Iron and Manganese based Magnetocaloric Materials for Near Room Temperature Thermal Management

V Chaudhary[1, 2, 3#], X Chen[3] and R V Ramanujan[3*]

[1]*Interdisciplinary Graduate School (IGS), Nanyang Technological University, Singapore 639798*
[2]*Energy Research Institute @ NTU (ERI@N), Nanyang Technological University, Singapore 637553*
[3]*School of Materials Science & Engineering, Nanyang Technological University, Singapore 639798*
[4]*Singapore-HUJ Alliance for Research and Enterprise (SHARE), Nanomaterials for Energy and Energy-Water Nexus (NEW), Campus for Research Excellence and Technological Enterprise (CREATE), Singapore 138602, Singapore*
Corresponding author email: *ramanujan@ntu.edu.sg (R V Ramanujan)

varun004@e.ntu.edu.sg (V Chaudhary)

Abstract

Thermal management technology based on the magnetocaloric effect offers several advantages over conventional gas compression cooling. The efficiency of magnetic cooling systems can be much higher than conventional gas based cooling technologies. Additionally, ozone layer depleting chemicals are not used and there is reduced noise and vibrations. Iron and manganese based magnetocaloric materials (MCM) are promising due to the challenges surrounding the use of conventional rare earth based MCM. We review the recent progress in the development of iron and manganese based MCM. The magnetic phase transitions, processing techniques, performance, as well as applications of these materials are discussed. Critical analysis to determine the critical exponents and phase transition behavior of these MCM, using modified Arrot plot, critical isotherm plots, the Kouvel-Fisher method, Landau theory and the Bean-Rodbell model, is also presented.

Key words: Magnetocaloric materials, magnetocaloric effect, Fe based alloys, Mn based alloys, modeling

Table of Contents

1. Introduction

A high percentage of energy utilization throughout the world is devoted to thermal management systems e.g., air conditioners and refrigerators[1]. Magnetic cooling, using the magnetocaloric effect (MCE), has high potential to address the worldwide urgent demand for environmentally friendly, green and energy efficient thermal management. Magnetic cooling based on the MCE has attracted considerable interest as a technology to reduce global warming[2-17]. Magnetic cooling can, in principle, be used for both small scale and large scale applications, whereas, conventional vapour compressor based technology is generally only useful for large scale applications. Magnetic cooling relies on the nearly instantaneous flip of magnetic spins under magnetic field[18, 19]. In principle, it can achieve Carnot efficiency, and can exhibit significantly higher energy efficiency compared to conventional vapour compression based systems[20]. A smaller number of moving parts in magnetic cooling systems can facilitate extended service life[21].

The search for affordable magnetocaloric materials for near room temperature applications has gained considerable momentum in the last decade. Paradoxically, global warming is partly because of air conditioners and refrigerators but we try to stay cool using air conditioners! The target to control global warming to less than 2 °C is a focus of international climate discussion[22]. The United States of America (USA) has a greater energy consumption for air conditioning than the rest of the world[23]. USA also uses more

electricity for cooling than the entire electricity consumption of Africa[23]. From 1993 to 2005, the energy consumed by residential air conditioning in the USA doubled because of larger homes and hotter summers. The climate impact of air conditioners is about half a billion metric tonnes of CO_2 per year. China is also one of the largest users of electricity for air conditioning and may overtake the US by 2020. In India, about 40% of the electricity of Mumbai was consumed by air conditioning[24]. More than 180 million cooling devices are produced every year using 10^3 tonnes of environmentally harmful hydrofluorocarbons (HCFCs), this will be equivalent to 28 – 45 % of CO_2 emissions in 2050[25], [26]. Magnetic cooling is environmentally friendly and energy efficient, and potentially be a good alternative to conventional air conditioning based on vapour compression technology. Magnetic cooling has already been shown to achieve 60% of Carnot (ideal) efficiency, while the best gas compression system can only reach only 40%[4, 20, 26]. Additionally, compressors are noisy and vibrate, whereas magnetic cooling devices can be less noisy and exhibit reduced vibration [26], [27]. Applications of magnetic cooling include a variety of thermal management applications including refrigeration, air-conditioning, cooling of vaccines, food industry, electronic devices, solar cell panels and data servers. The significance of improved cooling, can be seen, e.g., in data servers; approximately half of the total energy consumption is required to cool the servers [28].

Important characteristics of the magnetocaloric effect are that the effect is maximum in the vicinity of the transition temperature and it is reversible. Smith et al discussed the discovery of the magnetocaloric effect [10, 29]. The theoretical concept of a reversible change in temperature on application of an external magnetic field can be attributed to Thomson[30]. In 1917, Weiss and Piccard first experimentally observed the MCE in nickel by measuring a temperature change of 0.7 K for an applied field of 1.5 T, in the vicinity of its Curie temperature[31].Warburg was aware of the work of Thomson which he cited in his paper

[32]. Warburg performed experiments to study heat evolution in iron at room temperature under low magnetic fields (~50 Oe) [32]. He could demonstrate heating due to irreversible hysteresis phenomena, but his experiment could not measure the temperature difference of ~10^{-6} K required to observe the MCE of iron at ambient temperature. In 1992, Kuz'min and Tishin clearly mentioned that MCE was observed in nickel by Weiss and Piccard[33]. However, in 1999, Tishin, Gschneidner, Pecharsky stated incorrectly that the MCE was discovered by Warburg [34-36]. These influential papers, published in 1999, wrongly led the broader research community to attribute the discovery of the MCE to Warburg. Debye in 1926 and Giauque in 1927 independently to each other described the origin of low temperature cooling using adiabatic demagnetization of paramagnetic salts[37, 38]. The nature of MCE in a solid is the outcome of the change in entropy due to coupling of the magnetic spins of the electrons with the external magnetic field[8]. The possibility of using this technique at room temperature was introduced by Brown through a magnetic refrigerator prototype working in an Ericsson cycle with Gd as the magnetocaloric materials (MCM) and a magnetic field generated by superconducting magnets[39]. Pecharsky and Gschneidner's discovery[40] of materials with a "giant" MCE at room temperature, and the use of permanent magnets by the Astronautics Cooperation[41], reignited interest in this field. Since then, several families of magnetocaloric materials as well as magnetic refrigerator prototypes have been studied[4, 7]. An example is a compressor free wine cooler, based on MCE, developed by Haier and BASF in 2015. In this cooler, up to 35% less power is required compared to conventional cooling systems. Camfridge, Whirlpool, TCS Micropump, PSU Tec, Cemafroid, and International Institute of Refrigeration participated in a European Union project ELICiT (Environmentally Low Impact Cooling Technology)[42]. The main goal of ELICiT is to replace the domestic refrigerator with a solid state magnetic refrigerator. Toshiba and General Electric (GE) are also developing

magnetic cooling systems. GE targets to bring a magnetic refrigerator to the market shortly[43].

The magnetic refrigeration cycle of MCM can be described in terms of magnetic moments, lattice vibrations and the electronic states associated with magnetic entropy, lattice entropy and electronic entropy. The change in the lattice vibrations and magnetic moments depends on the magnitude of the applied magnetic field and the temperature of the material. The entropy of a magnetic solid (S) at constant pressure is a function of both temperature (T) and magnetic field (H) and is the sum of magnetic (S_M), lattice (S_{Lat}), and electronic (S_{el}) entropies:

$$S(T,H) = S_M(T,H) + S_{Lat}(T) + S_{el}(T) \quad (1)$$

Among these three types of entropies, the magnetic entropy is highly field dependent. When a magnetic field is applied adiabatically, the magnetic moments align parallel to the field, decreasing the magnetic entropy (Fig. 1 (a, b)). The total entropy of the system does not change since the lattice vibrations increase to compensate for the decreased magnetic entropy. Hence, the temperature of the system increases. Using a suitable heat transfer fluid, the system temperature can be reduced back to its initial value (Fig. 1 (c)). Importantly, when the magnetic field is adiabatically removed, the magnetic entropy increases and therefore lattice entropy and temperature decrease (Fig. 1 (d)). Now the magnetocaloric material is cold and can absorb heat from the heat load. Thus, a magnetic refrigeration cycle can be constructed.

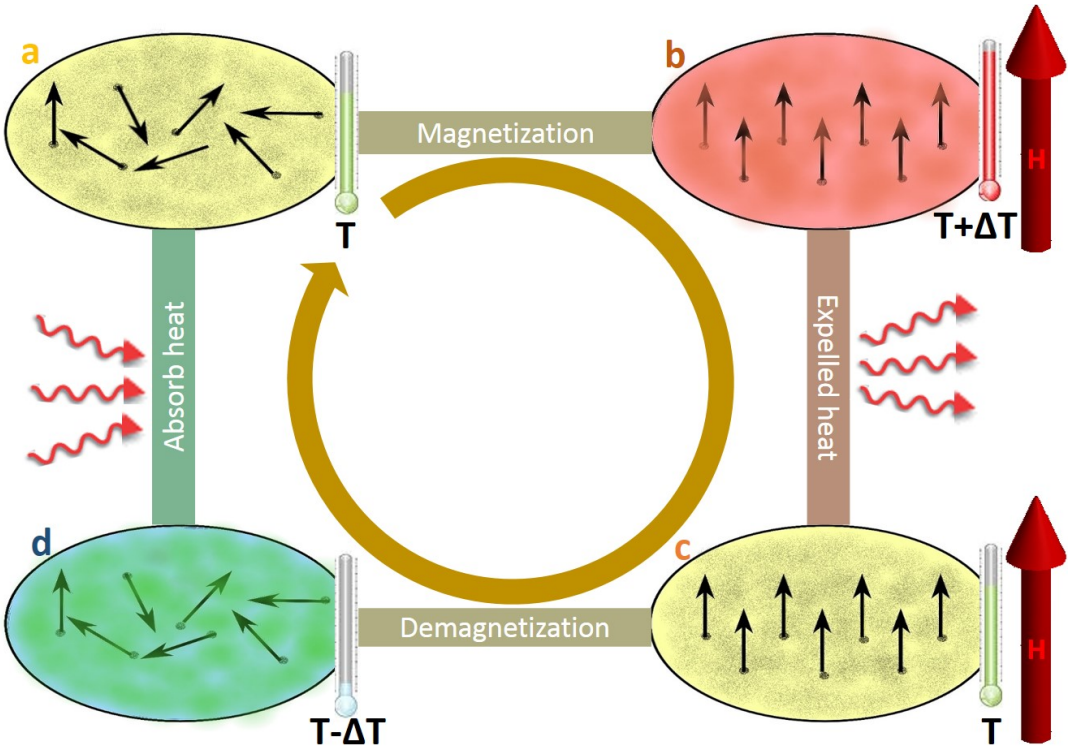

Fig. 1 Magnetocaloric cycle (a) a magnetocaloric material having random magnetic moments, (b) when the material is adiabatically magnetized, the magnetic entropy decreases and the temperature increases, (c) the material is brought back to its initial temperature after removal of heat by a suitable heat transfer fluid, (d) when the material is adiabatically demagnetized, the temperature decreases and this lower temperature can be used to cool the heat load.

2. Characterization of magnetocaloric materials

The MCE of magnetic materials is associated to the isothermal change in magnetic entropy (ΔS_M) and the adiabatic temperature change (T_{ad}). Fig. 2 shows the change in magnetic entropy as a function of temperature with, as well as without, an applied magnetic field. Isothermal and adiabatic processes are denoted by vertical and horizontal lines.

2.1. Adiabatic temperature change (ΔT_{ad}) and magnetic entropy change (ΔS_M)

If the change in applied magnetic field is represented by ΔH, the adiabatic change in temperature (ΔT_{ad}) can be defined as[44]:

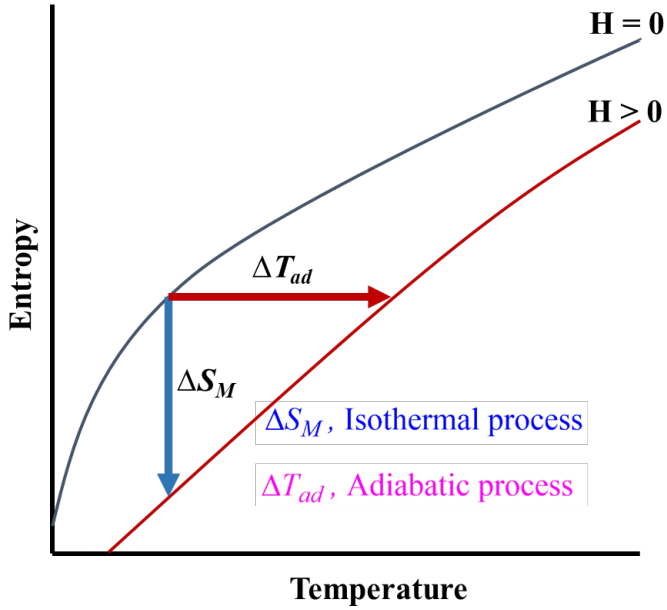

Fig. 2 A schematic of the entropy of MCM as function of temperature, showing the ΔS_M (vertical arrow) and the ΔT_{ad} (horizontal arrow).

$$\Delta T_{ad} = \int_0^H -\frac{T}{C_H}\left(\frac{\partial M}{\partial T}\right)_H dH \tag{2}$$

Where, C_H and M are the specific heat capacity and magnetization, respectively.

Integration of the above equation yields the Maxwell equation:

$$\Delta S_M = \int_0^H \left(\frac{\partial M}{\partial T}\right)_H dH \tag{3}$$

The numerical approximation of the above Maxwell's relation can be written as

$$\Delta S_M = \sum_i \frac{M_{i+1}(T_{i+1,}H_i) - M_i(T_{i,}H_i)}{T_{i+1} - T_i}\Delta H_i \tag{4}$$

With the help of the above equation and magnetic isotherms, the temperature dependence of change in magnetic entropy can be calculated. If the shape factor is included, then the above Maxwell equation must be recalculated using the internal field ($H = H_{ap} - NM$, where N is

the demagnetization factor; N = 1/3 for spherical particles), instead of the applied field. However, this correction usually does not significantly affect ΔS_M (~5 % reduction in magnitude)[45].

According to the second law of thermodynamics, the infinitesimal change of magnetic entropy can be described as

$$dS_M = \frac{C_H}{T} dT \tag{5}$$

Using the third law of thermodynamics *i.e*., the entropy of a system is assumed to be zero at temperature T = 0 and integration of Eq. 4, the entropy change in response to a magnetic field change can be expressed as[46]:

$$\Delta S_M(T) = \Delta S(T) = \int_0^T \frac{[C_H(H_f,T) - C_H(H_i,T)]}{T} dT \tag{6}$$

Where $C_H(H_f,T)$ and $C_H(H_i,T)$ represent, at constant pressure p, the specific heat of the material at the final and initial magnetic field, respectively. The above equations can be used to develop new materials with large MCE. Interpretation of ΔT_{ad} values for a magnetocaloric material is more straightforward than ΔS_M values. However, ΔT_{ad} is more difficult to determine experimentally since the equation for ΔT_{ad} contains a term C_H and some laboratories do not have the equipment to measure C_H.

A material can only have large MCE when the change of magnetization with temperature at constant field $\left(\partial M/\partial T\right)_H$ is large and the heat capacity C_H is small [27, 47, 48]. Both ΔT_{ad} and ΔS_M are relevant performance metrics since the heat capacity will vary depending on the type of magnetocaloric material, e.g., manganites have much greater heat capacity compared to Gd based alloys[8, 47]. The following information about the MCE of materials

can be developed (Eq. 2, 3 or 4): In both paramagnetic and ferromagnetic materials, magnetization decreases with increasing temperature i.e., $\left(\partial M/\partial T\right)_H < 0$. Hence, ΔS_M should be negative and ΔT_{ad} should be positive for positive field changes *($\Delta H > 0$)*. In ferromagnetic materials, the value of $|\left(\partial M/\partial T\right)_H|$ is largest at T_C, therefore $|\Delta S_M(T, \Delta H)|$ should be maximum at $T = T_C$. Tishin et al. have reported that, in the limit of ΔH tending to zero, ΔT_{ad} shows a peak near T_C for ferromagnets[34]. The behavior of ΔT_{ad} and $|\Delta S_M(T)|$ should be similar, i.e., gradually reduce on both sides of T_C. For the same $|\Delta S_M(T)|$ value, the value of ΔT_{ad} will be larger at higher absolute temperature (T) and lower heat capacity. Paramagnetic materials show significant value of $\Delta T_{ad}(T, \Delta H)$ only at temperatures close to absolute zero. The small value of $|\left(\partial M/\partial T\right)_H|$ is compensated by the small heat capacity. Furthermore, significant adiabatic temperature change is expected only if the solid spontaneously orders.

2.2. Relative cooling power

Relative cooling power *(RCP)* or refrigeration capacity is other important performance metric of MCM. It is a measure of the amount of heat transferred between the hot and cold reservoirs in one refrigeration cycle. For promising MCE materials, a high *RCP* is also needed, a large *RCP* implies a superior MCE material[44, 47]. Wood and Potter defined the *RCP* as[24]

$$RCP = \left|\Delta S_M\right|(T_{hot} - T_{cold}) \tag{7}$$

where $\left|\Delta S_M\right|$ is the change in the magnetic entropy, T_{hot} and T_{cold} are the temperatures at the hot and cold ends of the reservoirs, respectively. The *RCP* of MCM can be estimated from

the plots of ΔS_M vs T, as the product of maximum ΔS_M and the full temperature width at half maximum (δT_{FWHM}) of the peak in the ΔS_M vs T curve[19, 24, 47, 49-53] i.e.,

$$RCP(S) = \Delta S_M \times \delta T_{FWHM} \tag{8}$$

Some researchers calculate RCP by numerical integration of $\Delta S_M(T)$ under the full width at half maximum temperature limit[44].

$$RCP(S) = \int \left| \Delta S_M(\max) \right| dT \tag{9}$$

Engelbrecht et al. have reported that the shape of the ΔS_M vs T curve is crucial to good performance[54]. In device simulations, they found that different model materials with the same *RCP* can perform differently depending on the shape. In a practical AMR system, a material having a broad peak of isothermal entropy change shows significantly higher performance than a material exhibiting a sharp peak[54].

Magnetocaloric materials represent the most important elements of a magnetic cooling system. The following factors should be considered to select a MCM for near room temperature magnetic cooling[12, 19, 24]:

1. High MCE performance near room temperature
2. Large working temperature span
3. Low cost
4. Low magnetic and thermal hysteresis
5. Large saturation magnetization
6. High thermal conductivity and low specific heat
7. Easy processing and good chemical stability

3. First and second order magnetic phase transition in magnetocaloric materials

There are two groups of magnetocaloric materials, i.e., first order and second order, divided based on the nature of the magnetic phase transition. Fig 3 shows the schematic representation of the magnetization (M) and specific heat (C_H) for second-order (a, c) and first-order (b, d) materials with respect to temperature and magnetic field. Materials which exhibit a discontinuity in the first derivative of Gibbs free energy with respect to a thermodynamic variable during a phase transition are known as first order magnetic phase transition (FOMT) materials. The specific heat (C_H) exhibits a divergence at the transition temperature. With application of magnetic field, either this divergence is smeared out or the C_H peak is shifted to other temperatures.

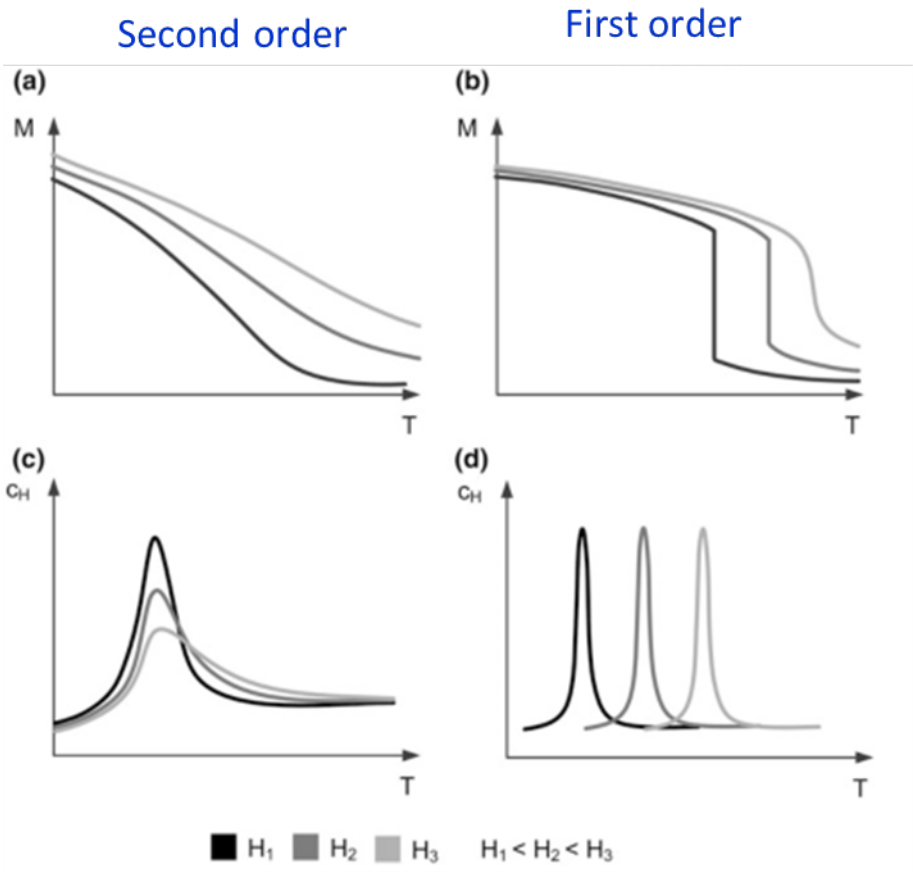

Fig. 3 Schematic representation of magnetization (M) and specific heat (C_H) with respect to temperature and magnetic field for second-order (a, c) and first-order (b, d) phase transition materials [55] .

Materials having a first order phase transition exhibit a large spike in magnetic entropy change over a narrow temperature range[27, 56-60]. For example, $Gd_5Si_2Ge_2$, is a "giant" MCE material, which shows a FM to PM transition, accompanied by a structural phase change from the orthorhombic to the monoclinic crystal structure[61-63]. Another example is $Ni_{43}Mn_{46}Sn_8In_3$ alloy composition which exhibits coupled structural and magnetic phase transitions[64]. Second-order magnetic phase transitions (SOMT) are transitions with continuous first derivatives of Gibbs free energy with respect to temperature but discontinuous second derivatives. The continuous nature of the transformation results in a finite value for *dM/dT* and *dS/dT*, reaching a maximum at the transition temperature. C_H shows a discontinuity at this transition temperature; however, with applied field, the discontinuity can be smeared out. Materials having a SOMT exhibit smaller ΔS_M with a broad temperature span. These materials have minimal or zero magnetic and thermal hysteresis. Many iron-based alloys exhibit a second order magnetic transformation. These alloys have been studied in bulk, ribbon and nanoparticle form.

4. Iron based magnetocaloric materials

The MCE of rare earth metals and their alloys have been intensively investigated due to their high entropy change (ΔS_M). The different magnetic structures in rare earths arise due to oscillations in the indirect interactions between 4f localized magnetic moments via conduction electrons. By suitable alloying with other rare earths, one can vary the magnetic transition temperature and the type of magnetic phase. The MCE of gadolinium has been studied in more detail than other rare earth metal[4, 46]. Gadolinium is treated as the standard MCM and generally, new materials are compared with it. The magnetocaloric properties of rare earth based materials have been previously elucidated[2, 4, 40, 65].

There are many complicated issues surrounding the use of rare earth because of international politics, high cost and availability. Toxicity concerns, manufacturing challenges, poor corrosion and oxidation resistance are additional hurdles. China has been the dominant supplier for rare earth materials for the past several decades (over 90% of world production in 2013). Another issue is that high performance ("giant") rare earth based MCM exhibit large magnetic and thermal hysteresis, which reduces their efficiency. Therefore, developing low cost, readily available are needed to fully exploit this technology in commercial applications. Here, we focus on the magnetocaloric alloys, which have small or no rare earth content. We begin this aim with Fe-Ni based alloys, followed by $Fe_{17}R_2$, Fe-B-Cr-R, Fe-Zr-B-M, Fe-Zr-B-Cu-M, Fe-B-X, Fe-Zr-M, $(Fe_xM_{1-x})_3Al$, Fe-M and other iron based MCM including iron based oxides and high entropy alloys. The MCE of the iron based alloys are compared with reference to T_C, ΔS_M, ΔH and RCP. Prototypes analyzing these MCM for self-pumping magnetic cooling are presented. Modeling results using critical analysis, including Arrot plot, critical isotherm plot and the method of Kouvel-Fisher are discussed at the end of experimental section (section 6).

4.1. Fe-Ni-M (M = B, Mn, Cr, Mo) alloys

The Fe-Ni alloys are well known family of soft magnetic alloys and therefore, their T_C is well above room temperature. Since the majority commercial applications focus on near room temperature, studies have been conducted to lower the T_C while retaining soft magnetic properties. The B (glass forming), Mn or Cr (antiferromagnetic) and Mo (paramagnetic) alloying additions to Fe-Ni were studied to reduce T_C. The Bethe-Slater curve provides a basis to select Mn and Cr alloying additions[66].

Fig. 4 illustrates the Fe-Ni phase diagram for a range of temperatures from 200 ºC to 1600 ºC, as well as T_C for the γ-phase (FCC) and the α-phase (BCC)[67]. On the iron side of the

Fe-Ni phase diagram, especially in the γ-phase region, the T_C is not well characterized. Miller et al. reported that the γ-phase of $(Fe_{73}Ni_{27})_{88}Zr_7B_4Cu_1$ can be stabilized by annealing the alloy at 700 ºC for 2 h, followed by water quenching[68]. The experimental T_C value for $(Fe_{73}Ni_{27})_{88}Zr_7B_4Cu_1$ powder was 120 ºC, which matched well with the T_C calculated by extrapolation of the T_C of the γ-phase to that of the relevant metastable phase region in the phase diagram. A small change in the composition of a few weight percent can result in a large change in T_C in Fe rich Fe-Ni alloys, as the extrapolated curve is very steep. $Fe_{70}Ni_{30}$ was prepared, and the γ-phase stabilized by water quenching in the γ-phase region. This composition was selected since, on the Fe rich side, the γ-phase could not be stabilized by quenching and on the nickel rich side the T_C was very high.

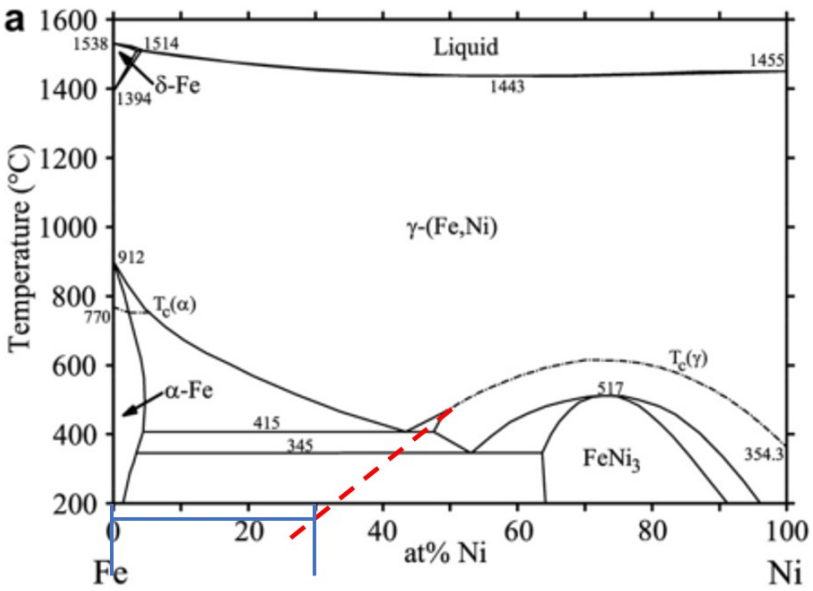

Fig. 4 Fe–Ni phase diagram. The dashed red line is the extrapolation of the T_C of the γ-phase to the iron rich region.

Fig. 5 shows the *M(T)* (left) and the d*M*/d*T* (right) versus *T* for γ-($Fe_{70}Ni_{30}$) nanoparticles, measured under a field of 0.1 T in a PPMS equipped with a VSM[24]. γ-$Fe_{70}Ni_{30}$ nanoparticles can be produced by high-energy ball milling, followed by an annealing treatment in the γ-phase region and quenching. The T_C of γ-($Fe_{70}Ni_{30}$) nanoparticles was found to be 438 K, as determined from the plot of *dM/dT* versus *T*. The T_C for γ-($Fe_{70}Ni_{30}$), as estimated from an extrapolation to metastable phase in the phase diagram, was found to be 443 K.

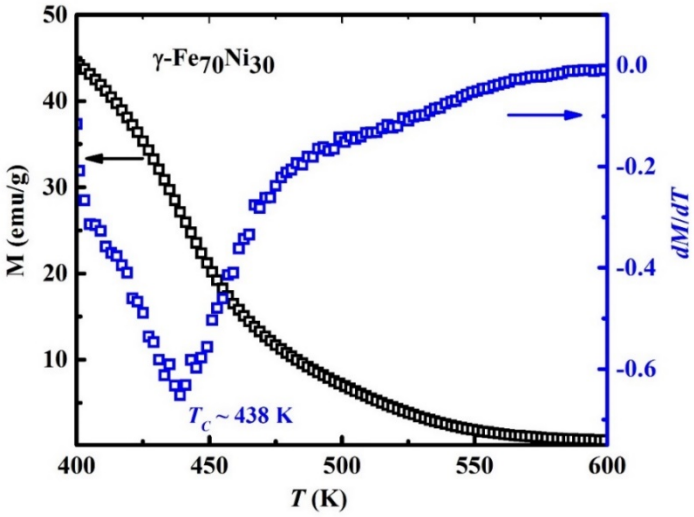

Fig. 5 The *M(T)* (left) and the d*M*/d*T* (right) versus *T* for γ-($Fe_{70}Ni_{30}$) nanoparticles

In order to tune T_C to near room temperature values, a suitable third element was added. The MCE of $(Fe_{70}Ni_{30})_{100-x}A_x$ (A = Mn, Cr and B) nanocrystalline powders produced by high-energy ball milling were studied. Boron, manganese and chromium were individually added to reduce T_C.[19, 52, 53, 69]

In the case B addition, γ-$(Fe_{70}Ni_{30})_{89}B_{11}$ nanoparticles were found to exhibit very high RCP of 640 Jkg^{-1} and ΔS_M of 2.1 $Jkg^{-1}K^{-1}$ for $\Delta\mu_0 H$ of 5 T, with $T_C \sim 381$ K. The moderate change in entropy along with broad operating temperature range and very high RCP make these nanoparticles appropriate candidates for magnetic cooling applications in low grade waste

heat recovery[19]. Enhanced working temperature span (δT_{FWHM}) of multiphase Fe-Ni-B bulk alloy was also reported[53]. Fig. 6 shows the change in magnetic entropy for quenched $(Fe_{70}Ni_{30})_{89}B_{11}$ nanoparticles and bulk $(Fe_{70}Ni_{30})_{89}B_{11}$ alloy as a function of temperature, for applied magnetic field up to 5 T.

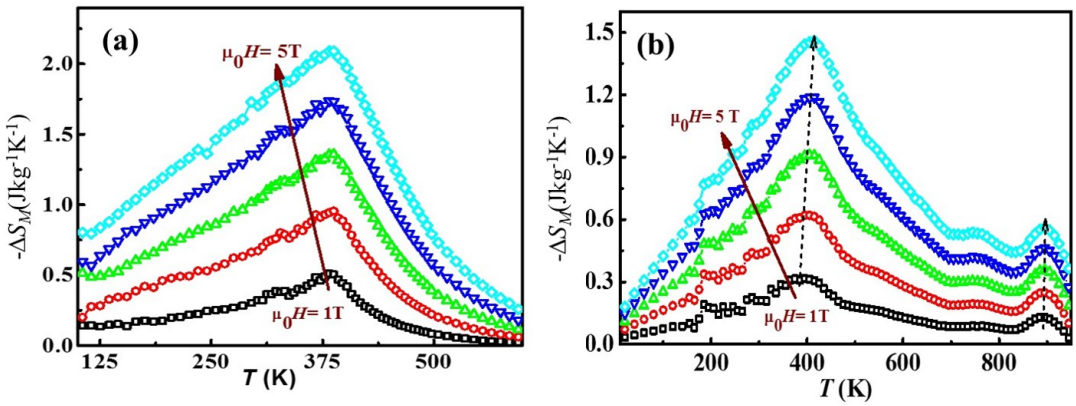

Fig. 6 (a) $-\Delta S_M$ versus T for (a) $(Fe_{70}Ni_{30})_{89}B_{11}$ nanoparticles (b) multiphase bulk $(Fe_{70}Ni_{30})_{89}B_{11}$ alloy at applied magnetic field up to 5 T[19, 24, 53].

The coexistence of multiphase (fcc, bcc, and spinel phases) results in a large δT_{FWHM} of 439 K, for a field change of 5 T. δT_{FWHM} value for multiphase $(Fe_{70}Ni_{30})_{89}B_{11}$ alloy is ~ 86 % higher than the value for a single phase γ-$(Fe_{70}Ni_{30})_{89}B_{11}$ alloy, for ΔH = 1 T. The reason for this high value of δT_{FWHM} is the difference in T_C of the three phases in $(Fe_{70}Ni_{30})_{89}B_{11}$ and the non zero magnetization over a wide temperature range of M vs T curves. Caballero-Flores et al. aslso reported an enhancement in RCP of 37% in a two phase $Fe_{88-2x}Co_xNi_xZr_7B_4Cu_1$ alloy (x= 0 to 1)[70]. The mass fraction of the existing phase and therefore MCE of these multiphase materials can be tuned by controlling the synthesis parameters, such as temperature/time of annealing [53]. For a magnetic regenerator, such multiphase materials with a broad temperature distributed ΔS_M is more attractive than materials with sharp ΔS_M peaks.

To further tune the T_C, $(Fe_{70}Ni_{30})_{100-x}B_x$, (x = 15, 18) alloys were prepared. The temperature dependence of magnetization for water quenched samples shows that the magnetization

values decrease as boron content is raised to 15% and 18%. There is little change in magnetization with temperature, indicating that the T_C of these alloys is above 400 K. The variation of magnetization and T_C of Fe-B and Co-B alloys with changing boron concentration has been previously determined[71-73]. It was found that T_C rises with greater B content in Fe-B alloys while it drops in the case of Co-B alloys. On the other hand, the magnetization value decreases with boron content in Fe-B and Co-B alloys, as in the case of Fe-Ni-B alloys. Hasegawa et al. reported that rapidly quenched $Fe_{100-x}B_x$ alloys ($12 \leq x \leq 28$) exhibit higher Curie temperature and reduced saturation magnetization[73]. This change in *Tc* is related to atomic rearrangements, such as short-range ordering or clustering during heating and quenching[74].

In studies of Mn alloying to Fe-Ni, the MCE of $(Fe_{70}Ni_{30})_{100-x}Mn_x$ nanoparticles were measured before and after γ–phase stabilization. It was shown that fast quenching is required for γ–phase stabilization. Fig. 7 shows the ΔS_M versus T at applied magnetic field of 5 T for $(Fe_{70}Ni_{30})_{95}Mn_5$ (quenched), $(Fe_{70}Ni_{30})_{92}Mn_8$ (as milled), $(Fe_{70}Ni_{30})_{92}Mn_8$ (vacuum annealed), $(Fe_{70}Ni_{30})_{92}Mn_8$ (quenched) and $(Fe_{70}Ni_{30})_{89}Mn_{11}$ (quenched) nanoparticles. The γ-$(Fe_{70}Ni_{30})_{95}Mn_5$ (T_C ~ 338 K) and γ-$(Fe_{70}Ni_{30})_{92}Mn_8$ (T_C ~ 317 K) nanoparticles possess good relative cooling power (RCP), up to 470 Jkg^{-1} and 415 Jkg^{-1}, respectively, for a field change of 5 T.

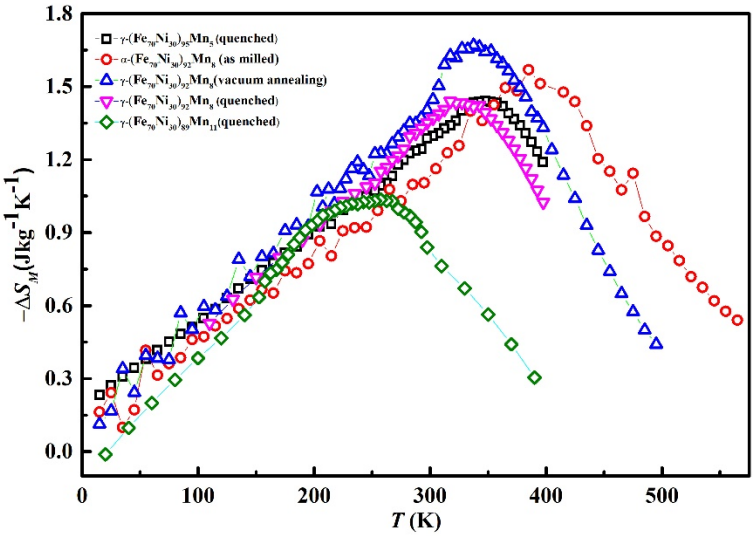

Fig. 7 $-\Delta S_M$ versus T at applied magnetic field of 5 T for $(Fe_{70}Ni_{30})_{95}Mn_5$ (quenched), $(Fe_{70}Ni_{30})_{92}Mn_8$ (as milled), $(Fe_{70}Ni_{30})_{92}Mn_8$ (vacuum annealed), $(Fe_{70}Ni_{30})_{92}Mn_8$ (quenched) and $(Fe_{70}Ni_{30})_{89}Mn_{11}$ (quenched) nanoparticles[24].

For the case of Cr additions, the MCE of transition metal based $(Fe_{70}Ni_{30})_{100-x}Cr_x$ (x = 1, 3, 5, 6, and 7) nanoparticles were studied (Fig 8)[12]. Alloying of Fe-Ni with 5% of Cr reduced the T_C significantly, from ~ 443 K to 258 K, the RCP value is 406 Jkg^{-1}; higher than those of Gd nanoparticles (400 Jkg^{-1}), at $\Delta\mu_0 H$ of 5 T. A maximum $|\Delta S_M|$ of 1.8 $Jkg^{-1}K^{-1}$ at ~ 125 K for a field change of 5 T was observed in a γ-$Fe_{49}Ni_{29}Cr_{22}$ alloy[75].

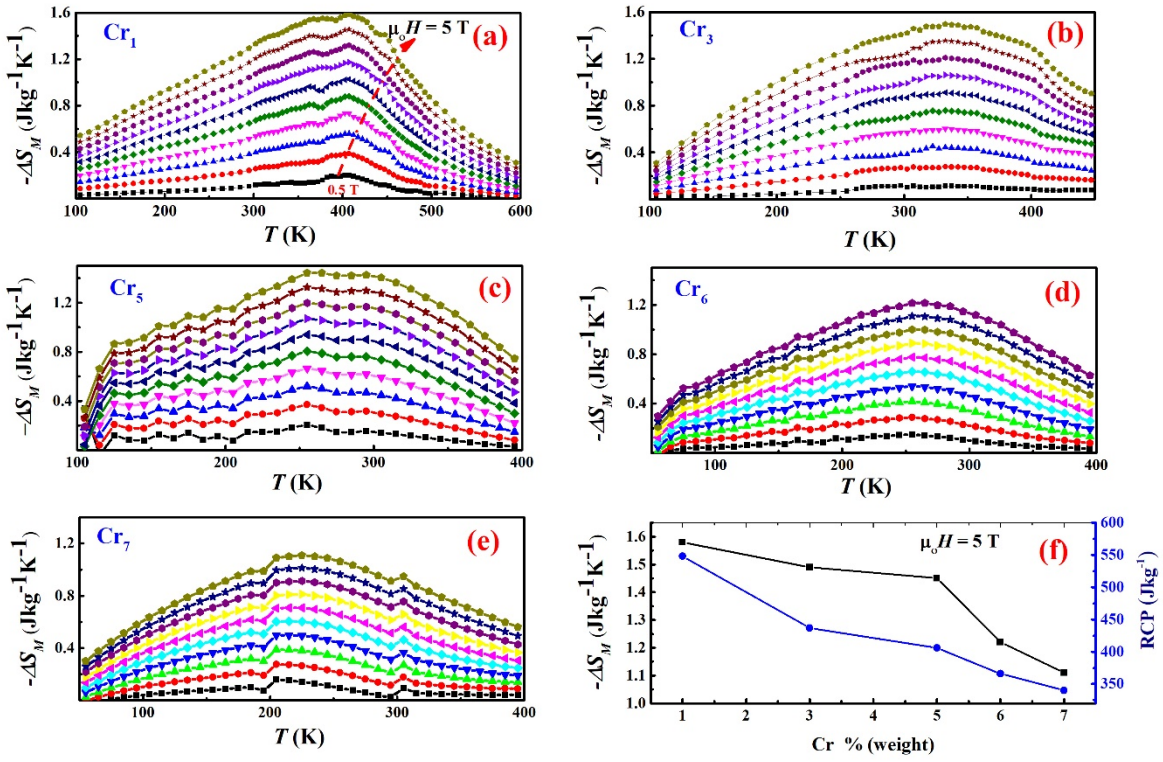

Fig 8 $-\Delta S_M$ versus T under magnetic field strength ranging from 0.5 T to 5 T for **(a)** $(Fe_{70}Ni_{30})_{99}Cr_1$, **(b)** $(Fe_{70}Ni_{30})_{97}Cr_3$, **(c)** $(Fe_{70}Ni_{30})_{95}Cr_5$, **(d)** $(Fe_{70}Ni_{30})_{94}Cr_6$, and **(e)** $(Fe_{70}Ni_{30})_{93}Cr_7$. **(f)** Dependence of $-\Delta S_M$ (left axis) and RCP (right axis) on Cr content in $(Fe_{70}Ni_{30})_{100-x}Cr_x$ nanoparticles[12].

The experimental values of T_C for $(Fe_{70}Ni_{30})_{100-x}Mn_x$ and $(Fe_{70}Ni_{30})_{100-x}Cr_x$ were compared with the theoretical values calculated from the expression $T_C = T^l_C + (dT_C/dc)c$[12, 24, 66]. T^l_C is the Curie temperature for the $Fe_{70}Ni_{30}$ alloy and dT_C/dc is the rate of change of Curie temperature with concentration c. The dT_C/dc value for Cr and Mn is -3.2 $\times 10^3$ K/wt % and -1.9 $\times 10^3$ K/wt %. To plot this expression, T_{C1} (443 K) was obtained by extrapolation to the metastable region of the Fe-Ni phase diagram, this value is reasonably close to the T_C (438 K) measured from experimental data.

Fig. 9 ((a) and (b)) shows the change in T_C with Mn and Cr content in ternary $(Fe_{70}Ni_{30})_{100-x}Mn_x$ and $(Fe_{70}Ni_{30})_{100-x}Cr_x$ alloys. The experimental T_C values for $(Fe_{70}Ni_{30})_{100-x}Mn_x$ and $(Fe_{70}Ni_{30})_{100-x}Cr_x$ alloys are rationally close to those calculated from the empirical formula

$T_C = T^1_C + (dT_C/dc)c$. The compositional tuning of T_C with minimal change in magnetization makes these alloys important for near room temperature cooling applications.

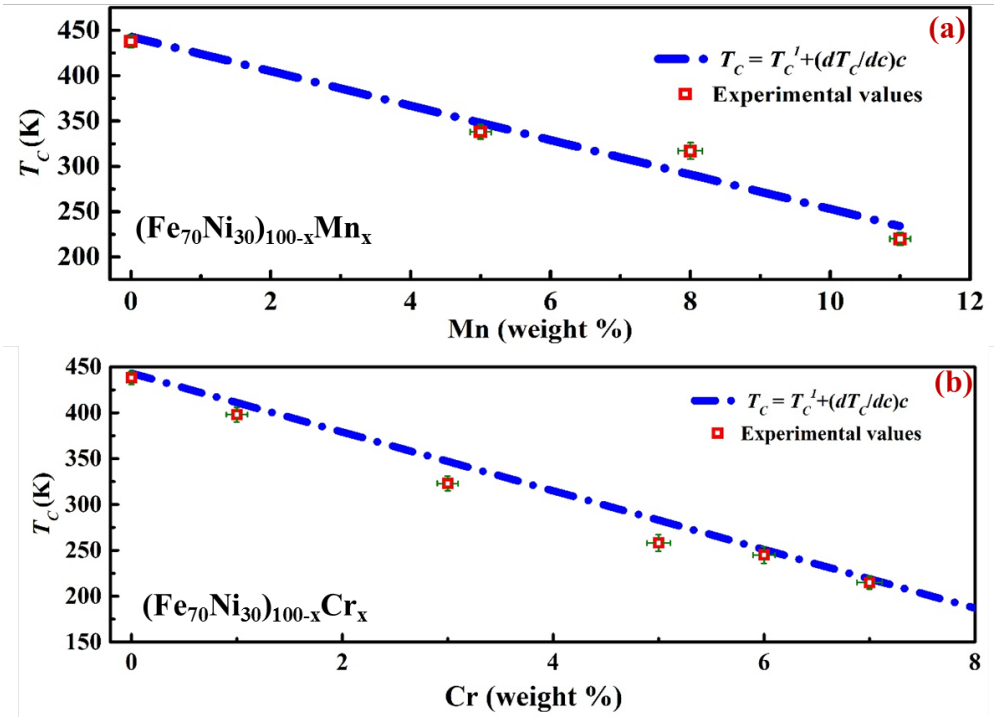

Fig. 9 T_C as a function of composition (a) $(Fe_{70}Ni_{30})_{100-x}Cr_x$ with x= 0 to 8. (b) $(Fe_{70}Ni_{30})_{100-x}Mn_x$ with x= 0 to 11. Solid line represents the theoretical values predicted from FeNi phase diagram and empirical equation $T_C = T^1_C + (T_C/dc)c$, while points (red square) are experimental results[12].

In case of Mo containing Fe-Ni alloys, Ucar at al. produced nanocrystalline powders of $(Fe_{70}Ni_{30})_{100-x}Mo_x$ (x = 1 to 4) by high energy mechanical alloying[76]. The T_C was lowered by Mo addition and a large working temperature span obtained. The $(Fe_{70}Ni_{30})_{96}Mo_4$ alloy was found to possess an RCP of 432 Jkg^{-1} at 5 T, comparable to other prominent MCM operating near room temperature. $Fe_{40}Ni_{38}Mo_4B_{18}$ amorphous alloy exhibited a $|\Delta S_M|$ of 1.1 $Jkg^{-1}K^{-1}$ and a RCP of 36 Jkg^{-1} for a field change of 1 T at 600 K[77].

Extended milling time induced oxidation of γ-Fe-Ni particles due to the elevated temperatures induced by milling, this effect was utilized to tune the T_C[78]. Mechanical alloying of $(Fe_{70}Ni_{30})_{89}Zr_7B_7$ powders leads to the formation of the γ-Fe-Ni phase, with a T_C

of 342 K[79]. The maximum ΔS_M and RCP of these powder was 0.182 $Jkg^{-1}K^{-1}$ and 0.20 Jkg^{-1}, respectively, at applied field of 0.5 T. Fig. 10 is a summary of the RCP and T_C for the Fe-Ni based alloys. It can be seen that a wide range of choices are now available for variety of applications. With alloying of Cr or Mn with $Fe_{70}Ni_{30}$, both T_C and RCP were found to be decrease.

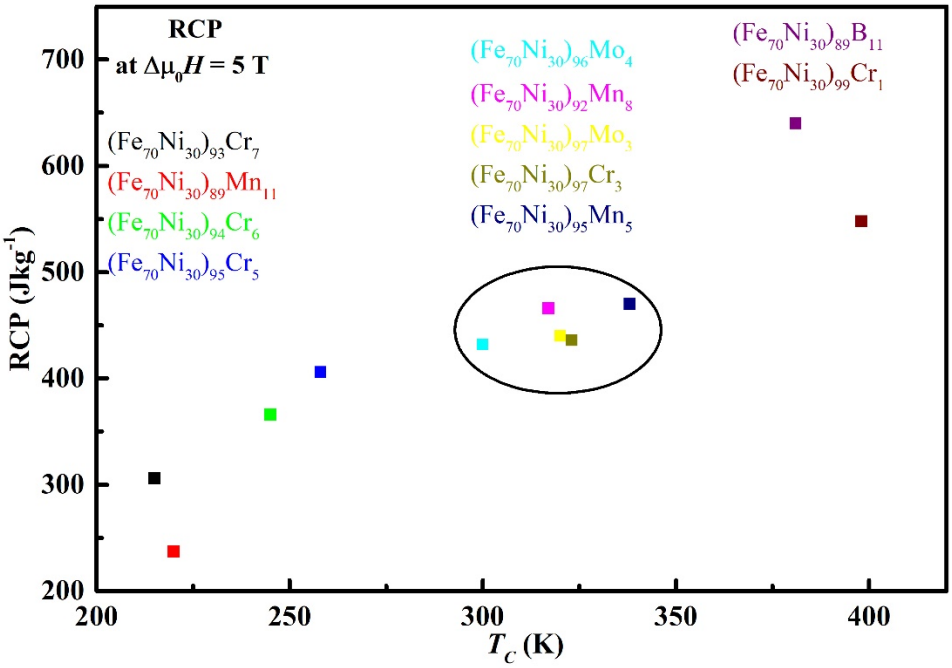

Fig. 10 Relative cooling power versus Curie temperature for Fe-Ni based nanoparticles. The materials for near room temperature applications are shown within the circle.

4.2. $Fe_{17}R_2$ (R = rare earths, Y) Alloys

$Fe_{17}R_2$ compounds, where R is a rare earth, shows moderate magnetocaloric effect (MCE) near room temperature. Gorria et al. discussed the potential of $Fe_{17}Pr_2$ nanostructured material as a room temperature magnetocaloric material[80]. They highlighted the differences in the MCE properties of particles and bulk. The maximum ΔS_M was found to be lower in powders while the δT_{FWHM} increased by a factor close to 2, which resulted in high RCP compared to the bulk alloy[80]. The increase in RCP was attributed to the broadening of magnetic entropy in nanoparticles. The exchange interactions in a nanostructured material

usually have a distribution of magnetic transitions, which results in broader magnetization change with temperature and therefore large working temperature span. Álvarez et al. used a high energy ball mill to produce nanocrystalline $Fe_{17}Nd_2$ powders[81]. A decrease of crystalline size to ~ 10 nm was observed, resulting in considerable expansion between disordered grain boundaries. They observed that the nanocrystalline samples exhibit a distribution in T_C, decreased maximum value of ΔS_M and high working temperature span, the magnetization versus temperature curve reveals a slower decrease than those of bulk samples. In another study, the correlation between the broadening of ΔS_M and the T_C distribution in nanostructured $Fe_{17}Pr_2$ and $Fe_{17}Nd_2$ powders synthesized by high-energy ball-milling was studied[82]. In both cases, the local environment of Fe atoms, and corresponding magnetic interactions, change with increasing milling time, resulting in a broader T_C distribution. $Fe_{17}Er_2$ exhibited both direct and inverse MCE with moderate ΔS_M and adiabatic temperature (ΔT_{ad}) change[83]. The inverse MCE was due to crystalline electric field-level crossover in the Er sub-lattice and ferrimagnetic interactions between the Er and Fe sub-lattice.

The effect of demagnetizing factor on ΔS_M and RCP in $Fe_{17}Er_2$ prepared by arc melting was investigated[84]. $Fe_{17}NdPr$ ribbons composed of nanocrystals within an amorphous phase showed two successive phase transitions, giving rise to increased working temperature span and enhanced RCP[85]. The RCP values for $Fe_{17}NdPr$ ribbons were larger than those of $Fe_{17}Pr_2$ bulk crystals. The magnetic moment of the $(Fe_{1-x}Mn_x)_{17}Dy_2$ compounds decreases gradually with increasing Mn content when $x \leq 0.2$, which is attributed to the antiparallel coupling effect of Fe and Mn magnetic moments. The T_C of the $(Fe_{1-x}Mn_x)_{17}Dy_2$ decreased with Mn doping, indicating that the Mn doping can effectively tune the T_C to room temperature. The maximum $|\Delta S_M|$ of $(Fe_{1-x}Mn_x)_{17}Dy_2$ compounds with $x = 0.0$, 0.1, and 0.2 are 3.9, 2.8, and 1.7 $Jkg^{-1}K^{-1}$, respectively, for field change of 5 T.

The ΔT_{ad} can be measured either directly or indirectly[44, 86]. However, usually, very limited study on adiabatic temperature change has been performed because of lack of infrastructure in research laboratory and very time talking measurements. Alvarez-Alonso et al., measured ΔT_{ad} and ΔS_M of $Fe_{17}Er_2$ (Fig 11) [83].

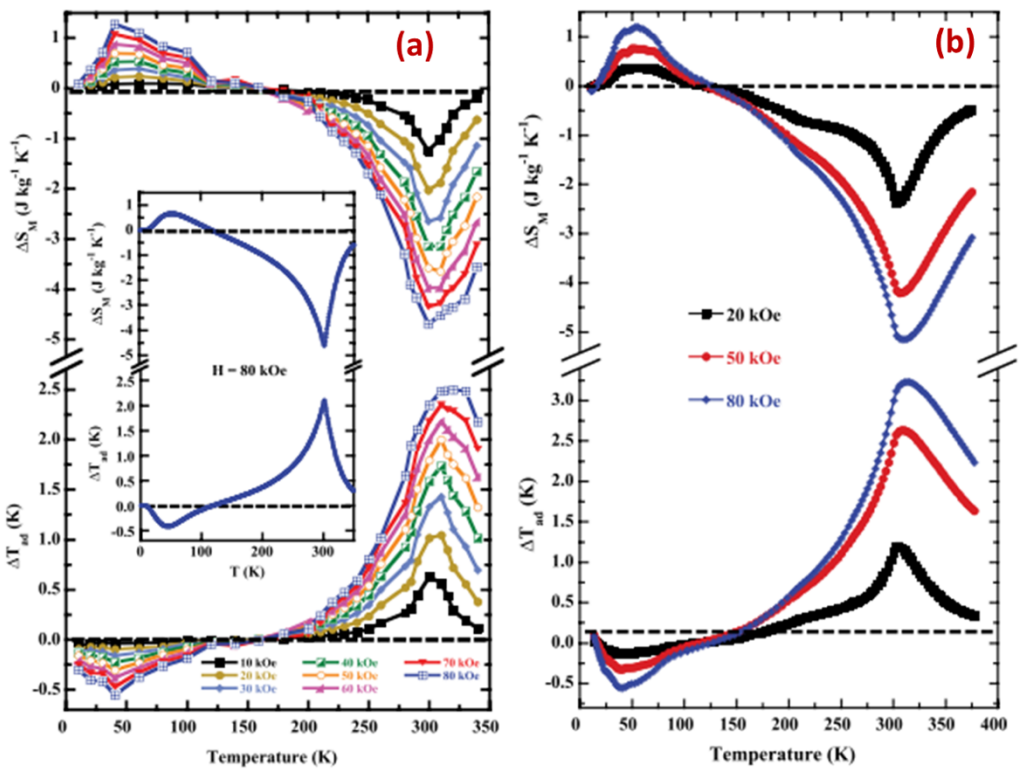

Fig. 11 Temperature dependence of ΔS_M and ΔT_{ad} under a magnetic field of up to 8 T for $Fe_{17}Er_2$ determined from (a) magnetization measurements and (b) heat-capacity measurements The insets of (a) show the theoretical values of ΔS_M and ΔT_{ad} [83].

The temperature dependence of ΔT_{ad} and atomic magnetic moments were described by a mean-field Hamiltonian, incorporating both the exchange interactions and the crystal electric field. $Fe_{17}Er_2$ exhibited both direct and inverse MCE with ΔS_M = -4.7 $Jkg^{-1}K^{-1}$ and ΔT_{ad} = 2.5 K near 300 K (T_C), and ΔS_M = 1.3 $Jkg^{-1}K^{-1}$ and ΔT_{ad} = −0.6 K at 40 K for $\Delta\mu_0 H$ = 8 T, respectively.

The MCE and crystal structure of $Fe_{17}Y_2$ melt spun ribbons was investigated with the wheel speed ranging from 10 to 40 m⁄s.[87] The crystal structure of the as-spun ribbons was the hexagonal Th_2Ni_{17} type. The ribbons prepared at 20 cm⁄s displayed a $|\Delta S_M|$ of 1.89 $Jkg^{-1}K^{-1}$

under magnetic field of 1 T. In another study, melt-spun ribbons of $Fe_{17}Y_2$ exhibited a maximum $|\Delta S_M|$ of 2.4 $Jkg^{-1}K^{-1}$ under an applied magnetic field of 2 T. The $\Delta S_M(T)$ curves for melt spun ribbons were broader than those for the bulk, resulting in enhancement of ~ 15% in the RCP[88].

4.3. Fe-B-Cr-R (R = La, Ce, Gd, Nd) Alloys

Law et al. studied the MCE of $Fe_{80-x}B_{12}Cr_8R_x$ (R=La, Ce or Gd, x = 1-15 at.%) alloys[44, 89-92]. Ce alloying to Fe-B-Cr alloys decreases the peak temperature (T^{pk}) at which ΔS_M occurs to near room temperature (RT) values, making such alloys highly relevant to RT applications. Addition of Gd to Fe-B-Cr amorphous alloys shifts T_C to higher temperatures, making them useful for high temperature applications. The addition of rare earth in Fe-B-Cr amorphous alloys increased the value of RCP. The highest MCE in this series was observed for a $Fe_{79}B_{12}Cr_8Gd_1$ alloy, which exhibited ~ 29% larger MCE than that of $Gd_5Si_2Ge_{1.9}Fe_{0.1}$, with transition temperature at ~ 350 K. The RCP of $Fe_{79}B_{12}Cr_8La_1$ and $Fe_{75}B_{12}Cr_8La_5$ alloys were ~ 17-27% larger than that of $Gd_5Si_2Se_2$, while those of $Fe_{78}B_{12}Cr_8Ce_2$ and $Fe_{75}B_{12}Cr_8Ce_5$ alloys displayed a 6-20% improvement compared to $Gd_5Si_2Ge_2$. The temperature dependence of ΔS_M for this series is presented in fig. 12.

T^{pk} could be tuned to near room temperature values by addition of 5% Ce to $Fe_{80}B_{12}Cr_8$. The good RCP values coupled with soft magnetic behavior and tunable T_C make Fe-B-Cr-R amorphous alloys useful for multi-MCM regenerators operating near and above room temperature. Desirable table-like MCE properties were obtained in composite $Fe_{88-x}Nd_xCr_8B_4$ (x=5, 8, 10, 12, and 15) alloys, with the T_C ranging from 322 K to 350 K [93]. The $|\Delta S_M|$ of these alloys was found to be constant value of ~ 3.2 $Jkg^{-1}K^{-1}$ for a field change of 5 T.

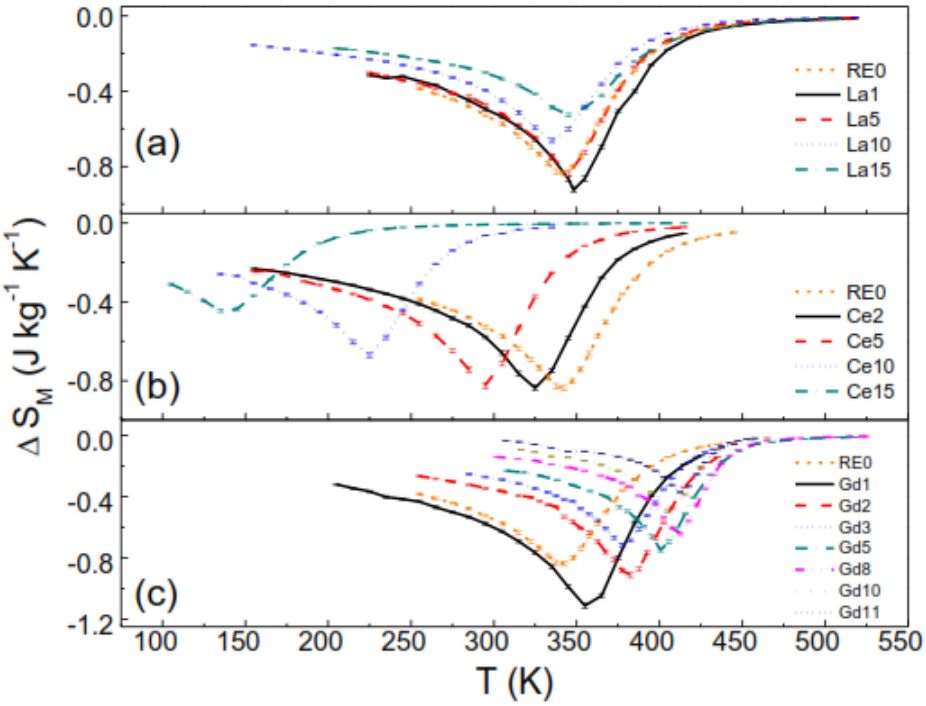

Fig. 12 ΔS_M versus T for a magnetic field of 1.1 T; (a) $Fe_{80-x}B_{12}Cr_8La_x$ (b) $Fe_{80-x}B_{12}Cr_8Ce_x$ (c) $Fe_{80-x}B_{12}Cr_8Gd_x$ melt spun ribbons[44].

4.4. Fe-Zr-B-M (M = Mn, Cr, Ni, Al, Ti, Mo, Co, Er, Sm) alloys

The T_C and saturation magnetization of $Fe_{89-x}Zr_{11}B_x$ (x = 0 - 10) alloys increases almost linearly with B addition[94]. An enhancement of $|\Delta S_M|$ from 1.3 $Jkg^{-1}K^{-1}$ for the $Fe_{89}Zr_{11}$ alloy to 1.73 $Jkg^{-1}K^{-1}$ for the $Fe_{79}Zr_{11}B_{10}$ alloy, for an applied magnetic field of 1.8 T was observed. The T_C of $Fe_{91}Zr_7B_2$ and $Fe_{88}Zr_8B_4$ alloys was found to be 230 and 285 K, respectively[95]. A maximum $|\Delta S_M|$ of 3 $Jkg^{-1}K^{-1}$ (with magnetic field of 5 T) and a large working temperature span (δT) of ~ 200 K, resulted in high RCP of ~ 435 Jkg^{-1}. The T_C can be simply altered from 200 to 350 K by varying the boron content. Fig. 13 shows the maximum ΔS_M as a function of temperature for both alloy compositions under a magnetic field of 0.4 T[96]. The effect of Zr and B on the MCE of $Fe_{90-x}Zr_{10}B_x$ (x = 3 to 9) and $Fe_{93-x}Zr_7B_x$ (x = 0 to 13) amorphous alloys has been obtained[96]. The dependence of maximum ΔS_M on the sum of the Zr and B content associated with the average magnetic moment per

Fe atom, as in the case of the $Fe_{91-x}Mo_8Cu_1B_x$ (x=15, 17, 20) amorphous series[96, 97].. The T_C can be tuned from ~ 225 K to 350 K and from 250 K to 410 K for $Fe_{90-x}Zr_{10}B_x$ (x = 3 to 9) and $Fe_{93-x}Zr_7B_x$ (x = 0 to 13) amorphous alloys, respectively. Enhanced T_c, as well as enhanced ΔS_M were achieved with increasing boron content in the $Fe_{91-x}Zr_9B_x$ (x = 3, 4, 5) amorphous alloys due to the higher direct interaction between Fe atoms[98]. The T_C and maximum ΔS_M of the three series, i.e., $Fe_{89-x}Zr_{11}B_z$ (x=3, 4, 5, 6, 8 and 10), $Fe_{91-y}Zr_9B_y$ (y=3, 4, 5, 6, 8 and 10) and $Fe_{94-z}Zr_6B_z$ (z=5, 6, 8 and 10), ribbons increases linearly with increasing boron content[99]. Recently, the effect of Sm, Er, Co, and Mn additions on the MCE of Fe-Zr-B based metallic glasses was studied[100]. The $Fe_{88}Zr_7B_3Co_2$ alloy exhibited the largest RCP of 123.37 Jkg^{-1} and $Fe_{86}Zr_8B_4Sm_2$ exhibited the largest $|\Delta S_M|$ of 1.116 $Jkg^{-1}K^{-1}$, while both alloys exhibit T_C of 320 K. The addition of Co to Fe-Zr-B results in an enhanced glass forming ability, MCE and T_C[100, 101].

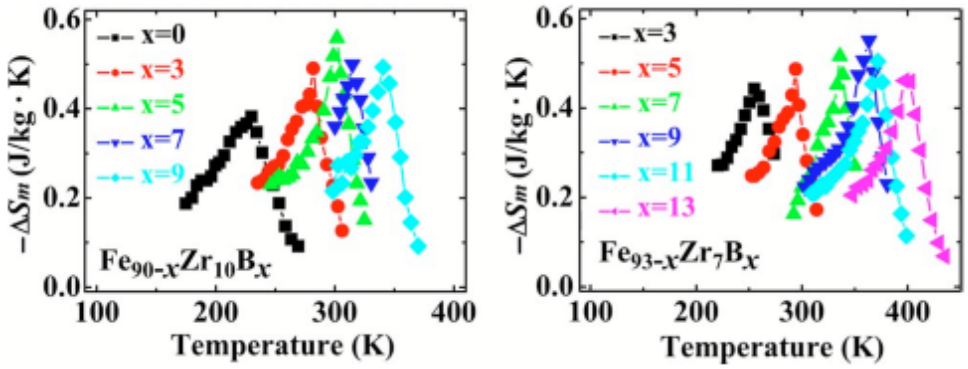

Fig. 13 Magnetic entropy change as a function of temperature under magnetic field of 0.4 T for (a) $Fe_{90-x}Zr_{10}B_x$ (x = 3 to 9) and (b) $Fe_{93-x}Zr_7B_x$ (x = 0 to 13)[96].

Feng at al. investigated the MCE of amorphous Fe-Zr-B-M alloys (M = none, Mn, Cr and Co) ribbons. They found an enhanced MCE in $Fe_{90-x}Zr_{10}B_x$ (x = 5, 10, 15 and 20) ribbons by addition of B[102]. The T_C of these alloys can be decreased close to room temperature by appropriate substitution of Mn and Cr. The ΔS_M of the Co-substitution series of $Fe_{85-y}Zr_{10}B_5Co_y$ alloy was found to be constant, though the T_C increased to ~ 400 K for y=5.

$Fe_{85-y}Zr_{10}B_5Co_y$ ribbons exhibit constant MCE and a refrigeration capacity of ~90 Jkg^{-1}, for a magnetic field change of 1 T. The MCE of amorphous Fe-Zr-B-M (M = Al, Ni, Co, and Ti) ribbons has also been studied[103]. Both the ΔS_M and the RCP of the base alloy $Fe_{88}Zr_8B_4$ were enhanced by alloying additions. T_C increased by addition of Co addition, but decreased with addition of Al and Ti. The alloy containing 1 at.% Co with T_C of 295 K and $|\Delta S_M|$ of 1.48 $Jkg^{-1}K^{-1}$ (for an applied magnetic field of 1.5 T), is suitable for near room temperature applications. On the other hand, the alloy containing 1 at.% Ti exhibit T_C of 270 K and RCP of 183.5 Jkg^{-1}. Johnson and Shull[104] reported the MCE in melt spun $(Fe_xCo_yCr_z)_{91}Zr_7B_2$ amorphous alloy with $x:y:z$ = 100:0:0, 90:15:5, 85:5:10 and 75:15:10. By tuning the composition, the T_C values could be varied from 200 K to 450 K, making this material promising for multistage regenerators.

4.5. Fe-Zr-B-Cu-M (M = Co, Co-Ni) alloys

The effect of Co addition on the MCE of Nanoperm-type compositions $Fe_{83}Zr_6B_{10}Cu_1$ and $Fe_{78}Co_5Zr_6B_{10}Cu_1$, were studied for high temperature applications[105]. Co additions results in an enhanced maximum ΔS_M and a shift to higher temperatures. A value of RCP of ~ 82 Jkg^{-1} was obtained for a magnetic field change of 1.5 T. This value is 30% larger than that of a Mo-containing Finemet-type alloy measured under the same experimental conditions. The T_C of the as melt spun material $Fe_{88-2x}Co_xNi_xZr_7B_4Cu_1$ (x = 0 – 22) was found to increase with Co and Ni content from 346 K at x = 0 to 843 K at x = 22[106]. In this study, the MCE of this alloy was not examined. The partial substitution of Fe by Co and Ni in the series of $Fe_{88-2x}Co_xNi_xZr_7B_4Cu_1$ alloys results in an increase in T_C from 287 K for x = 0 to 626 K for x=11[107]. The maximum $|\Delta S_M|$ (for an applied magnetic field of 1.5 T) was observed to be 1.98 $Jkg^{-1}K^{-1}$ for x = 8.25.

4.6. Fe-B-X (Mn, Nb, Cr, Cu) alloys

The partial substitution of Fe by Mn in amorphous $Fe_{80-y}Mn_yB_{20}$ (y= 10, 15, 18, 20, and 24) ribbons results in a change in T_C from 438 K for x = 10 to 162 K for x= 24[108]. The maximum $|\Delta S_M|$ reduced from 1 $Jkg^{-1}K^{-1}$ for x = 10 to 0.5 $Jkg^{-1}K^{-1}$ for x= 24; the RCP reduces from 117 Jkg^{-1} for x = 10 to 68 Jkg^{-1} for x = 24, for an applied magnetic field of 1.5 T. A linear relationship between the maximum $|\Delta S_M|$ and average magnetic moment per transition metal atom $<\mu>_{Fe,Mn}$ was obtained. The $Fe_{80.5}Nb_7B_{12.5}$ melt-spun ribbons exhibited a $|\Delta S_M|$ of ~ 0.72 $Jkg^{-1}K^{-1}$ at T_C of 363 K, at $\Delta\mu_0 H$ of 0.7 T[109]. The ΔS_M and T_C of the $Fe_{92-x}Cr_8B_x$ amorphous alloys increased with increasing B content from 12 to 15[110]. Chromium addition to a $Fe_{81}Nb_7B_{12}$ alloy resulted in a decrease of T_C from 363 to 279 K, making this series attractive for near room temperature applications[111]. The $|\Delta S_M|$ of non-crystallized ribbons of Fe-Nb-B-Cr has been found to be ~ 0.7 $Jkg^{-1}K^{-1}$, at an applied magnetic field of 0.7 T. Torrens-Serra et al. reported changes in MCE with change of Nb content in $Fe_{79-y}Nb_{5+y}B_{15}Cu_1$ (y = 0, 2, 4) alloys.[112] The T_C and ΔS_M were enhanced by reduction of Nb content. The theoretical and experimental values of ΔT_{ad} of $Fe_{80}B_{12}Nb_8$ alloy was found to be 1.2 K and 0.7 K at applied field of 1.9 T, respectively[86]. These values are comparatively less than those of rare earth based magnetocaloric materials. These samples exhibited soft magnetic behaviour with very low coercivity. The values of RCP for $Fe_{81+x}Ce_{13-x}B_6$ (x = 0, 0.5, 1, 1.5, and 2) amorphous alloys were found to be in the range of 117 Jkg^{-1} to 150 Jkg^{-1} for magnetic field changes of 5 T[113].

4.7. Fe-Zr-M (Mn, Dy) alloys

The T_C of $Fe_{90-x}Zr_{10}Mn_x$ amorphous alloys decreased from 210 K to 185 K with increasing Mn concentration, from x = 8 to x = 10[114]. The maximum $|\Delta S_M|$ of $Fe_{82}Zr_{10}$ Mn_8 was 2.87

$Jkg^{-1}K^{-1}$ at 210 K for an applied magnetic field of 5 T. In another study, the values of maximum ΔS_M of $Fe_{90-x}Zr_{10}Mn_x$ amorphous alloy were found to be 2.96, 2.51 and 2.29 $Jkg^{-1}K^{-1}$ for x = 0, 4 and 6, respectively, in the vicinity of the respective T_C of 243, 228 and 218 K, respectively, for the same applied magnetic field of 5 T[115]. The T_C can be increased from 273 K to 305 K by changing the Dy content in $Fe_{90-x}Zr_{10}Dy_x$ from x = 1 to x = 3[116]. The maximum $|\Delta S_M|$ of the alloys with x = 1 and 2 was found to be 0.84 and 0.93 $Jkg^{-1}K^{-1}$, respectively, for a magnetic field change of 1.2 T.

4.8. $(Fe_xM_{1-x})_3Al$ (M = Cr, Mn) compounds

The magnetic properties of the Fe_3Al alloy depends on the degree of chemical ordering and the local atomic environment[117]. Fe_3Al has high saturation magnetization, low coercivity, high corrosion resistance and high strength but not suitable for room temperature cooling applications due to its high T_C (~710 K)[118, 119]. Substitution of Fe by Cr/Mn could tune the T_C to near room temperature values. The arc melted buttons and melt spun ribbons of $(Fe_{0.72}Cr_{0.28})_3Al$ alloys possessed the $L2_1$ crystal structure and B2 crystal structure, respectively. An enhanced ΔS_M and RCP for the ribbons compared to the buttons have been reported which is attributed to higher structural disorder in the Fe–Cr and Fe–Al sub-lattices of the B2 structure in ribbons[119]. The substitution of Fe by Mn in $(Fe_xMn_{1-x})_3Al$ also resulted in the decrease of T_C to near room temperature values. The $(Fe_{0.8}Mn_{0.2})_3Al$ alloy exhibited a $|\Delta S_M|$ of 0.96 $Jkg^{-1}K^{-1}$ and RCP of 400 Jkg^{-1} for a magnetic field change of 5 T. The T_C of $(Fe_xMn_{1-x})_3Al$ alloys was tuned in a wide temperature range, from 165 K to 350 K.

4.9. Fe-M (M = Sc, Zr, Cu) alloys

$Fe_{90}Sc_{10}$ exhibits both positive and negative ΔS_M due to a field-driven metamagnetic transition from a spin-glass-like to a ferromagnetic state[120]. The hydrogenation to $Fe_{90}M_{10}$ (M=Zr, Sc) amorphous materials resulted in increased ΔS_M and tuning of T_C[121]. A large RCP of 216 Jkg^{-1} was obtained under a field change of 1.5 T. The effect of ion implantation on the MCE was studied in Fe-Zr amorphous films.[122] Enhanced $|\Delta S_M|$ and RCP, from 0.66 to 1.01 $Jkg^{-1}K^{-1}$ and 84.5 to 155.5 Jkg^{-1}, respectively, for C-implanted film compared to the as-grown film, was reported for a magnetic field change of 1.5 T. The increase of ΔS_M and RCP was due to increased magnetization and chemical inhomogeneity, respectively. The $|\Delta S_M|$ of Fe_xCu_{100-x} (x = 30, 32, 33, 35) varies with x, from 0.8 to 1 $Jkg^{-1}K^{-1}$ for a field change of 5 T[123]. The values of RCP of Fe_xCu_{100-x} alloys for x = 30, 32, 33 and 35 was found to be 195, 206, 208 and 234 Jkg^{-1}, respectively, under a field change of 5 T. The MCE of Fe/Cu thin films was studied, tuning the fraction of the interfacial Fe-Cu alloy resulted in control of the magnetic transition temperature and the magnetocaloric properties[124].

4.10. Other iron based alloys having four or more elements

Substitution of Fe by Tm in $(Fe_{0.76-x}Tm_xB_{0.24})_{96}Nb_4$ (x = 0, 0.01, 0.05, 0.1, 0.17 and 0.18) metallic glasses increases the glass-forming ability of these alloys, T_C decreased from 559 K (for x=0) to 325 K (x= 0.18)[125]. A linear relationship between ΔS_M and M_S was observed. The formation of the minority nanocrystalline $Tm_2Fe_{14}B_1$ phase was observed for higher Tm additions, which could influence the MCE. The substitution of Ce for Fe in amorphous ribbons of $Fe_{78-x}Ce_xSi_4Nb_5B_{12}Cu_1$ (x=0, 1, 3, 5 and 10) alloys resulted in a large T_C range, from 281 K to 465 K[126]. The ΔS_M for a field change of 5 T decreased from 3.25 to 2.18 $Jkg^{-1}K^{-1}$ for x = 0 to 10, respectively. Two types of composite materials with varying Ce content were obtained by layer by layer assembly of the ribbons[126]. The $|\Delta S_M|$ of the

composites approached a value of ~2.0 $Jkg^{-1}K^{-1}$ (for a field change of 5 T) and a temperature span of ~80 K was obtained, resulted in RCP values greater than 370 Jkg^{-1}.

The MCE of Fe-Nb-B and $Fe_{71.5}Cr_2Si_{13.5}B_9Nb_3Cu_1$ alloys prepared by rapid quenching from the melt was studied[127]. Replacement of Nb by Fe atoms or Fe by B atoms in the ternary Fe-Nb-B alloys results in enhancement of the T_C. The $|\Delta S_M|$ for $Fe_{84}Nb_7B_9$, $Fe_{85}Nb_6B_9$ and $Fe_{83}Nb_7B_{10}$ was found to be 1.0, 0.94 and 0.83 $Jkg^{-1}K^{-1}$, respectively, at $\Delta\mu_0 H$ of 1.5 T[127]. Changes in T_C and ΔS_M in $Fe_{80-x}Mn_xP_{10}B_7C_3$ metallic glasses have been achieved by varying Mn content in the range from x = 13 to 18[128]. The average magnetic moment per (Fe+Mn) atom correlates linearly with ΔS_M, resulting in lower ΔS_M with increasing Mn content. The $Fe_{65}Mn_{15}P_{10}B_7C_3$ alloy exhibits the maximum refrigeration capacity of 147.09 Jkg^{-1} and $|\Delta S_M|$ of 1.12 $Jkg^{-1}K^{-1}$ for an applied magnetic field of 2 T. This family of low-cost Fe based alloys provides an MCM which can be used for near room-temperature applications. A larger ΔS_M was found in quenched $Fe_{81.6}Mo_4Zr_{3.3}Nb_{6.8}B_1Cu$ ribbons because of structural and stress relaxation during heat treatment[129]. The RCP of multicomponent FeCrMoCuGaPCB alloys is comparable to that of a Mo-containing Finemet-type alloy and is 40% more than those of other bulk amorphous alloys with comparable working temperatures[130]. The temperature and field dependence of the MCE in a bulk amorphous $Pd_{40}Ni_{22.5}Fe_{17.5}P_{20}$ alloy exhibits a minimum value at the superparamagnetic-to-ferromagnetic transition and a maximum at the ferromagnetic-to-spin-glass transition[131]. At 80 K, and for $\mu_0 H$ = 5 T, the ΔS_M was -0.029 k_B per Fe atom in the alloy. The MCE of melt-spun $Fe_{64}Mn_{15-x}Co_xSi_{10}B_{11}$ (x = 0, 0.2, 0.5, 0.7, and 1.0) amorphous alloys has been evaluated near room temperature[132]. The maximum $|\Delta S_M|$ for $Fe_{64}Mn_{15}Si_{10}B_{11}$ at 309 K at $\mu_0 H$ = 1.5 T was limited to 0.82 $Jkg^{-1}K^{-1}$.

Boutahar et al. studied the effect of vanadium on the magnetocaloric properties of amorphous $Fe_{80-x}V_xB_{12}Si_8$ ribbons fabricated by the melt spinning technique. The addition

of V to the $Fe_{80}B_{12}Si_8$ alloy resulted in a decrease of T_C from 473.5 K to 335 K. The maximum value of ΔS_M decreased with increasing V content. A $Fe_{66.3}V_{13.7}B_{12}Si_8$ alloy exhibited the maximum RCP of 93.7 Jkg^{-1} and moderate $|\Delta S_M|$ of 1.034 $Jkg^{-1}K^{-1}$ for $\Delta\mu_0 H$ = 2 T[133].

$Fe_{74-x}Cr_xCu_1Nb_3Si_{15.5}B_{6.5}$ (x=2, 8, 10, 12, 13, 14 and 20) exhibited a broad T_C range, from 100 K to 550 K[134]. The T_C and maximum ΔS_M of these amorphous alloys decreased with an increase of Cr content at a rate of -25.6 K/at% Cr and -54 $mJkg^{-1}K^{-1}$/at% Cr, respectively. The T_C changed from 271 to 363 K when the x was increased from 2 to 8 in $Fe_{82-x}Co_xMn_4Zr_8Nb_2B_4$ amorphous ribbons, with almost similar ΔS_M and RCP for all the compositions[135]. The $|\Delta S_M|$ was found to be 1.7 $Jkg^{-1}K^{-1}$ and the RCP was ~115 Jkg^{-1} for a field change of 3 T.

Fig. 14 shows a comparison of RCP, at an applied magnetic field of 1.5 T and T_C for selected iron based MCM. For some materials, RCP was estimated from the figure in the references and for others, power law RCP α H^N was used, where N = 1.15 for transition metal based alloys[92, 107].

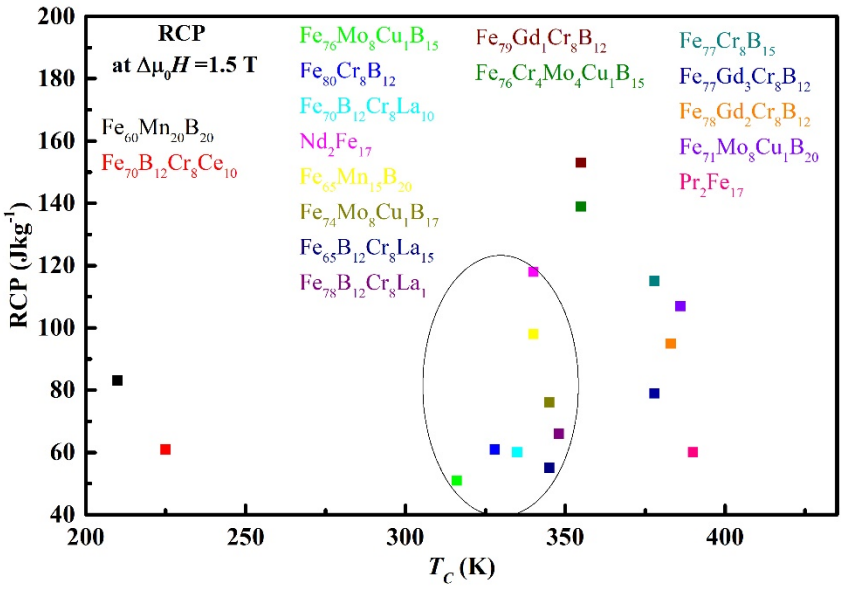

Fig. 14 Relative cooling power versus Curie temperature for Fe based magnetocaloric materials. Materials suitable for near room temperature applications are shown within the circle [89, 91, 92, 97, 105, 107, 108, 110, 130, 136, 137].

4.11. MCE in iron based high entropy alloys

The equimolar high-entropy FeCoCrNi alloy forms in the fcc crystal structure and possesses a T_C of 130 K[138]. The T_C was tuned to higher temperature by decreasing the Cr content in $FeCoCr_xNi$ alloys. The $|\Delta S_M|$ for cold-rolled FeCoCrNi was found to be 0.35 $Jkg^{-1}K^{-1}$ at an applied magnetic field of 2 T. Cold rolling resulted in a broadening of ΔS_M. Long range chemical ordering resulted in reduction of T_C since 4 out of the 12 nearest-neighbors of Fe, Co, and Ni atoms were Cr atoms. The MCE of the $Fe_1Co_1Ni_1Cr_1Pd_x$ alloy family, before and after annealing, with low molar fractions of Pd was also explored[139]. The ferromagnetic properties and T_C near room temperature in previously unexplored alloys was predicted when Pd was replaced by Ag, Au, or Cu[140]. Recently, McHenry and co-workers reported several high entropy alloys with tunable T_C for magnetocaloric applications[141, 142]. High resistance to wear and corrosion, and reduced metal flammability of high entropy alloys are additional advantage to use them for magnetocaloric applications.

4.12. MCE in iron based oxides

As discussed above many MCM have been developed based on the expectation that the higher density of solids compared to gases will allow for compact design of cooling devices. However, slow heat transfer in the bulk material is a constraining factor in magnetic cooling devices. Therefore, a suspension of magnetic particles in a suitable fluid for magnetic cooling has been proposed in several studies as an alternative to bulk MCM[143, 144]. Nanoparticles with increased surface area suspended in a suitable fluid have higher heat transfer compared to bulk devices. The magnetic behavior of such fluids varies with particle size, morphology, crystal structure and the particle – particle interactions. Nanostructures

can have higher MCE over a broad temperature distribution compared to the bulk. The MCE peak can be shifted to other temperatures or broadened by reducing the particle size. The advantage of magnetocaloric fluid based energy devices are a) they do not have any moving mechanical parts, b) there is no need for dynamic seals and valves, c) potential applications in micro and macro sized devices[55]. Suitably sized oxide nanoparticles, such as Co-ferrite, Mg-ferrite and ferrite nanoparticles, can be suspended into a carrier fluid for a reasonable time even in a magnetic field[51, 145, 146]. The main limitation of ferrofluid cooling technology is the process of dispersion of the nanoparticles in the fluid and their long term stability under a magnetic field[7, 147]. This challenge can be resolved by suitable surface chemistry on the nanoparticles.

When the particle size decreases to the magnetic domains size, enhanced spin disorder at surfaces is expected. Surface atoms experience large anisotropy due to the broken symmetry of their surroundings, which is called Néel surface anisotropy[148]. The ΔS_M broadening and high RCP of nanoparticles are due to the asymmetric nature of the exchange parameter and fluctuations in the interatomic spacing[51, 149]. The ΔS_M for $Mn_{0.3}Zn_{0.7}Fe_2O_4$ nanoparticles was found to be -0.88 $Jkg^{-1}K^{-1}$ for 5 T field at 300 K[51]. The broadening of the ΔS_M curve is due to the absence of sharp transition from FM to PM state. Similar behaviour of ΔS_M was reported in other Co and Mg based ferrites[150-152]. The $CoFe_2O_4/CoFe_2$ composite showed a positive as well as negative ΔS_M of 0.923 and -0.923 $Jkg^{-1}K^{-1}$ at a T_C of 310 and 290 K, respectively[153]. The MCE of $Zn_{1-x}Co_xFe_2O_4$ (x= 0 to 1) nanoparticles synthesized by the hydrothermal method were studied and they exhibited ΔS_M values in the similar to those of other ferrite[154]. However, the T_C for $Zn_{1-x}Co_xFe_2O_4$ nanoparticles is very high (606 K for x =0 to 823 K for x = 1), which is not useful for near room temperature applications. As discussed in section 3.1 and 3.2, Fe based

magnetic nanoparticles also exhibited larger relative cooling power than their bulk counterpart.

Iron based oxide nanoparticles are easy to suspend in carrier fluid compared to metallic nanoparticles. The suspension of magnetic nanoparticles (MNP) in a carrier fluid is known as ferrofluid or magnetic fluid. Such a ferrofluid can be used for transferring heat from a heat load to heat sink by the application of magnetic field. A ferrofluid experiences a change in magnetization when the fluid temperature changes[146, 155]. The magnetization is higher in the low temperature region compared to the high temperature region. Due to the applied magnetic field, a driving force is produced for fluid flow. This ferrofluid can therefore be used as a heat transfer medium. Fig. 15 shows a schematic of such a self pumping magnetic cooling system[155, 156].

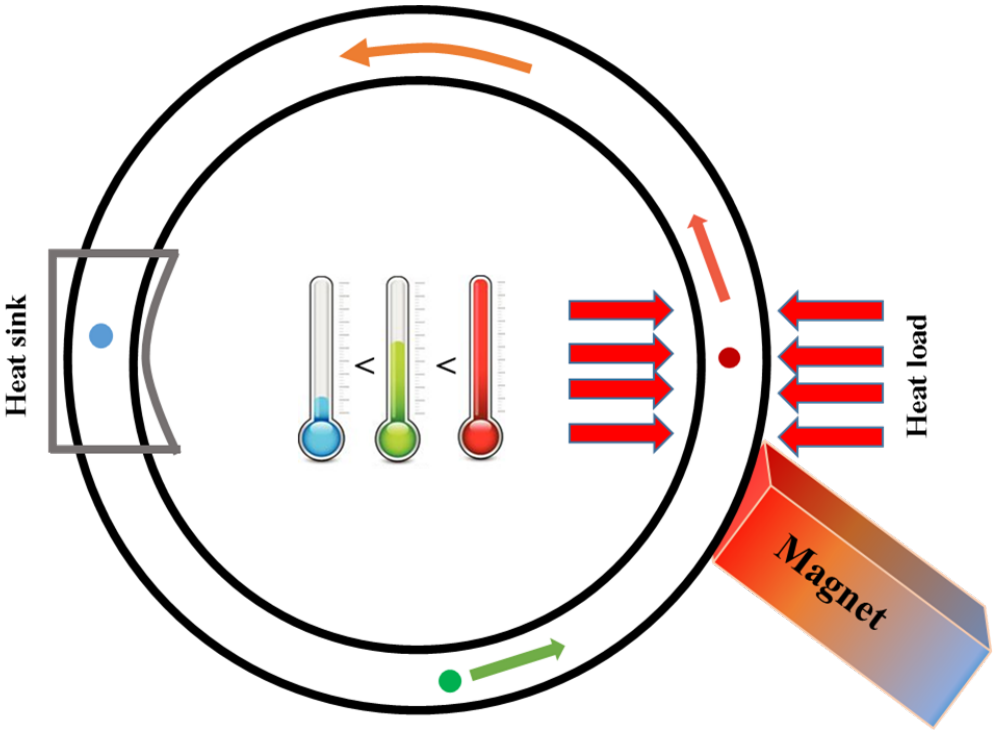

Fig. 15 Schematic representation of self-pumping magnetic cooling employing ferrofluid as heat transfer from heat load to heat sink.

A cold magnetic fluid (green circle) with finite magnetization is attracted by the magnetic field. As the fluid enters the thermal field of the heat load, the temperature increases (red circle) above the Curie temperature of the MNP in the ferrofluid. Therefore, in the thermal field, the ferrofluid temperature increases, the MNP become paramagnetic and are no longer attracted (or comparatively less attracted) to the magnetic field. This allows it to flow towards the heat sink. The ferrofluid again become ferromagnetic by transferring heat to the heat sink. The pumping of fluid is not strictly confined to T_C of the material, however, the best performance is expected in the vicinity of T_C due to the maximum change in magnetization at this temperature.

Rosenweig described the principle of magnetocaloric self-pumping using ferrohydrodynamic equations[144]. Love et al. suggested magnetocaloric pumping using only thermal and magnetic fields[145, 146]. A uniform magnetic field coincident with a temperature gradient results in a force on the magnetic fluid. A parametric study was showed to associate the heat transfer, temperature difference, cavity dimensions, magnetic field and fluid viscosity[157]. An experimental study to investigate the performance metrics of a cooling device and the effects of magnetic field and temperature distribution of the fluid on the cooling performance of a device was investigated[158]. Lian et al. established a energy transport device using a magnetocaloric ferrofluid as a coolant[159, 160]. The magnetic field gradient and the fluid temperature variation results in fluid motion in a loop. These devices can be applicable for energy transport systems including lab-on-a-chip, energy conversion devices, electronic cooling devices etc. since no mechanical moving parts are required.

Xuan and Lian presented a practical design of thermomagnetic convection in electronic cooling[161]. As the heat load increases (i.e., the temperature of chip increased), a higher heat dissipation rate is achievable due to larger thermomagnetic convection. Therefore, devices based on thermomagnetic convection can be treated as self-regulating devices[162].

Rahman and Suslov explained the linear stability of magneto-convection of a ferrofluid contained between two heated plates under uniform applied magnetic field[163]. A self-pumping magnetic cooling device, which does not require a mechanical pump or external energy input, has been investigated. Fig. 16 shows the temperature profiles of the heat load when the magnetic field was applied and subsequently removed[155]. The cooling (ΔT) increased from ~20 °C to ~28 °C, when the initial temperature of heat load was increased from 64 °C to 87 °C[155].

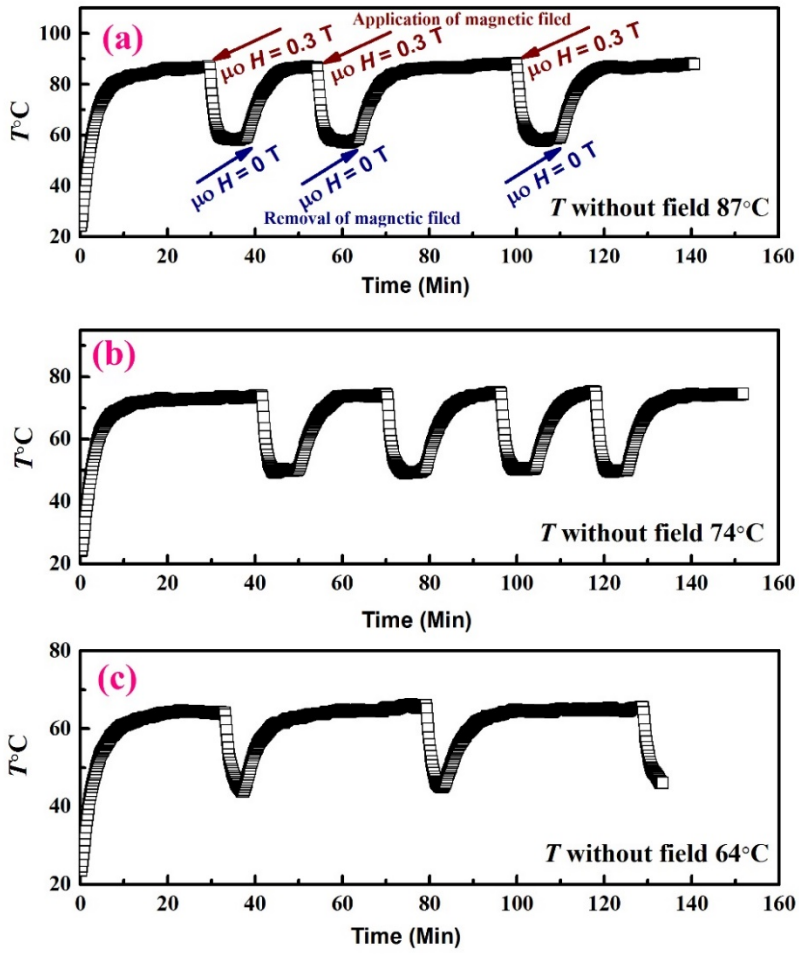

Fig. 16 The effect of application and removal of magnetic field of 0.3 T on the temperature profile for initial temperature of heat load of (a) 87 °C, (b) 74 °C and (c) 64 °C, respectively. The temperature drop (cooling) in (a), (b) and (c) was ~ 28 °C, ~ 24 °C and 20 °C, respectively[155].

Ferrofluid of Fe-Ni-Cr nanoparticles dispersed in oleic acid was used as the heat transfer medium to perform magnetic cooling[12]. However, due to the high viscosity of fluid (oleic

acid) and comparatively poor suspension stability of these nanoparticles, the cooling performance was not as good as iron oxide based MNP dispersed in water. It is expected that the first order magnetic transition materials can also be potential candidate for self-pumping magnetic cooling due to the sharp transition from the ferromagnetic state to paramagnetic state[164]. However, hysteresis and therefore, reversibility may be a barrier to continuous flow of ferrofluid.

We summarize the Curie temperature, change in entropy and relative cooling power for important iron based alloys in table 1.

Table 1. Magnetocaloric properties of iron based MCM.

Sample	Sample form	T_C (K)	$\|\Delta S_M\|$ ($Jkg^{-1}K^{-1}$)	$\Delta\mu_0 H$ (T)	RCP(Jkg^{-1})	Refs.
Fe-Ni-M (M = B, Mn, Cr, Mo) based alloys						
$Fe_{72}Ni_{28}$	NP	333	0.5	5	250	[78]
$Fe_{70}Ni_{30}$	NP	333	0.32	5	342	[78]
$(Fe_{70}Ni_{30})_{97}Mo_3$	NP	320	1.69	5	440	[76]
$(Fe_{70}Ni_{30})_{96}Mo_4$	NP	300	1.67	5	432	[76]
$(Fe_{70}Ni_{30})_{89}Zr_7B_4$	NP (20 nm)	353	0.7	1.5		[79]
$(Fe_{70}Ni_{30})_{89}Zr_7B_4$	NP (20 nm)	353	~2.8	5	~300	[79]
$(Fe_{70}Ni_{30})_{89}B_{11}$	NP (12 nm)	381	0.73	1.5	155	[19]
$(Fe_{70}Ni_{30})_{89}B_{11}$	NP (12 nm)	381	2.1	5	640	[19]
$(Fe_{70}Ni_{30})_{89}B_{11}$	Bulk(multiphase)	381	1.46	5	641	[53]
$(Fe_{70}Ni_{30})_{92}Mn_8$	NP	340	1.67	5	466	[52]
$(Fe_{70}Ni_{30})_{95}Mn_5$	NP	338	1.45	5	470	[69]
$(Fe_{70}Ni_{30})_{99}Cr_1$	NP (12 nm)	398	1.58	5	548	[12]
$(Fe_{70}Ni_{30})_{97}Cr_3$	NP (10 nm)	323	1.49	5	436	[12]
$(Fe_{70}Ni_{30})_{95}Cr_5$	NP (13 nm)	258	1.45	5	406	[12]
$(Fe_{70}Ni_{30})_{94}Cr_6$	NP (12 nm)	245	1.22	5	366	[12]
$(Fe_{70}Ni_{30})_{93}Cr_7$	NP (11 nm)	215	1.11	5	306	[12]

$Fe_{17}R_2$ (R = Rare earth) based alloys						
$Fe_{17}Pr_2$	NP (20 nm)	292	2.1	1.5	107	[80]
$Fe_{17}Pr_2$	NP (20 nm)	292	4.5	5	573	[80]
$Fe_{17}Nd_2$	NP (14 nm)	340	1.6	1.5	83	[81]
$Fe_{17}Nd_2$	NP (20 nm)	340	1.85	1.5	87	[81]
$Fe_{17}NdPr$	NP (20 nm)	303	2.1	2	175	[85]
$Fe_{17}Er_2$	Bulk	303	3.6	5	-	[83]
$Fe_{17}Y_2$	Ribbons	301	4.4	5	533	[88]
$Fe_{17}Y_2$	Bulk	303	4.6	5	448	[88]
$Fe_{17}Y_2$	Ribbons	304	1.8	1	54	[87]
Fe-B-Cr-R (R = La, Ce, Gd, Nd) Alloys						
$Fe_{80}B_{12}Cr_8$	Ribbons	342	1.09	1.5	131	[44]
$Fe_{79}B_{12}Cr_8Gd_1$	Ribbons	355	1.42	1.5	153	[44]
$Fe_{78}B_{12}Cr_8Gd_2$	Ribbons	383	1.18	1.5	95	[44]
$Fe_{77}B_{12}Cr_8Gd_3$	Ribbons	378	0.92	1.5	79	[44]
$Fe_{75}B_{12}Cr_8Gd_5$	Ribbons	400	0.95	1.5	73	[44]
$Fe_{79}B_{12}Cr_8La_1$	Ribbons	355	1.10	1.5	130	[44]
$Fe_{75}B_{12}Cr_8La_5$	Ribbons	345	1.06	1.5	116	[44]
$Fe_{83}Nd_5Cr_8B_4$	Bulk	323.3	1.8	2	93	[93]
$Fe_{80}Nd_8Cr_8B_4$	Bulk	340.2	1.8	2	82	[93]
$Fe_{78}Nd_{10}Cr_8B_4$	Bulk	345.3	1.9	2	81	[93]
$Fe_{76}Nd_{12}Cr_8B_4$	Bulk	349.9	1.9	2	78	[93]
$Fe_{73}Nd_{15}Cr_8B_4$	Bulk	349.6	1.8	2	78	[93]
Fe-Zr-B-M (M = Mn, Cr, Ni, Al, Ti, Mo, Co, Cu, Er, Sm) alloys						
$Fe_{80}Zr_{10}B_{10}$	Ribbons	365	1.47	1	-	[102]
$Fe_{85}Zr_{10}B_5$	Ribbons	318	1.20	1	-	[102]
$Fe_{75}Zr_{10}B_{15}$	Ribbons	390	1.30	1	-	[102]
$Fe_{88}Zr_9B_3$	Ribbons	286	0.94	1	-	[98]
$Fe_{87}Zr_9B_4$	Ribbons	304	0.99	1	-	[98]
$Fe_{86}Zr_9B_5$	Ribbons	327	1.02	1	-	[98]
$Fe_{89}Zr_6B_5$	Ribbons	320	0.5	1.5	55	[99]

$Fe_{88}Zr_6B_6$	Ribbons	330	0.94	1.5	103	[99]
$Fe_{86}Zr_6B_8$	Ribbons	380	1.06	1.5	116.6	[99]
$Fe_{88}Zr_9B_3$	Ribbons	300	0.62	1.5	49.9	[99]
$Fe_{87}Zr_9B_4$	Ribbons	310	0.80	1.5	80	[99]
$Fe_{86}Zr_9B_5$	Ribbons	330	1.13	1.5	135.6	[99]
$Fe_{85}Zr_9B_6$	Ribbons	330	0.98	1.5	117.6	[99]
$Fe_{83}Zr_9B_8$	Ribbons	370	1.04	1.5	124.8	[99]
$Fe_{81}Zr_9B_{10}$	Ribbons	380	1.13	1.5	113	[99]
$Fe_{86}Zr_{11}B_3$	Ribbons	300	0.77	1.5	77	[99]
$Fe_{85}Zr_{11}B_4$	Ribbons	310	0.89	1.5	71.2	[99]
$Fe_{84}Zr_{11}B_5$	Ribbons	330	1.02	1.5	91.8	[99]
$Fe_{83}Zr_{11}B_6$	Ribbons	330	0.97	1.5	87.3	[99]
$Fe_{81}Zr_{11}B_8$	Ribbons	350	0.93	1.5	102.3	[99]
$Fe_{79}Zr_{11}B_{10}$	Ribbons	360	1.04	1.5	104.4	[99]
$Fe_{84}Zr_{10}B_5Mn_1$	Ribbons	300	1.08	1	-	[102]
$Fe_{82}Zr_{10}B_5Mn_3$	Ribbons	273	1.04	1	-	[102]
$Fe_{80}Zr_{10}B_5Mn_5$	Ribbons	258	0.99	1	-	[102]
$Fe_{87}Zr_8B_4Mn_1$	Ribbons	280	0.757	1.5	83.27	[100]
$Fe_{86}Zr_8B_4Mn_2$	Ribbons	280	0.656	1.5	78.72	[100]
$Fe_{85}Zr_8B_4Mn_3$	Ribbons	280	0.669	1.5	66.9	[100]
$Fe_{80}Zr_8B_4Mn_8$	Ribbons	230	0.555	1.5	49.95	[100]
$Fe_{78}Zr_8B_4Mn_{10}$	Ribbons	220	0.483	1.5	43.47	[100]
$Fe_{84}Zr_{10}B_5Cr_1$	Ribbons	313	1.03	1	-	[102]
$Fe_{82}Zr_{10}B_5Cr_3$	Ribbons	297	1.02	1	-	[102]
$Fe_{80}Zr_{10}B_5Cr_5$	Ribbons	285	0.92	1	-	[102]
$Fe_{84}Zr_{10}B_5Co_1$	Ribbons	330	1.30	1	-	[102]
$Fe_{82}Zr_{10}B_5Co_3$	Ribbons	365	1.30	1	-	[102]
$Fe_{79}Zr_{11}B_{10}$	Ribbons	365	1.73	1.8	-	[94]
$Fe_{91}Zr_7B_2$	Ribbons	230	2.80	5	575	[95]
$Fe_{88}Zr_8B_4$	Ribbons	285	3.30	5	646	[95]
$Fe_{88}Zr_8B_4$	Ribbons	280	0.884	1.5	106.08	[100]

$Fe_{85}Zr_{10}B_5$	Ribbons	300	1.39	1.5	-	[96]
$Fe_{88}Zr_7B_4Ni$	Ribbons	285	1.32	1.5	132	[103]
$Fe_{88}Zr_7B_4Co$	Ribbons	295	1.48	1.5	177.6	[103]
$Fe_{88}Zr_7B_4Al$	Ribbons	280	1.37	1.5	154.8	[103]
$Fe_{88}Zr_7B_4Ti$	Ribbons	270	1.32	1.5	183.5	[103]
$Fe_{88}Zr_7B_4Cu$	Ribbons	287	1.32	1.5	166	[107]
$Fe_{83}Zr_6B_{10}Cu_1$	Ribbons	398	1.40	1.5	142	[105]
$Fe_{87}Zr_8B_4Co_1$	Ribbons	320	0.715	1.5	78.65	[100]
$Fe_{86}Zr_8B_4Co_2$	Ribbons	340	0.915	1.5	100.65	[100]
$Fe_{88}Zr_7B_4Co_1$	Ribbons	300	0.672	1.5	87.36	[100]
$Fe_{87}Zr_7B_4Co_2$	Ribbons	330	0.774	1.5	100.62	[100]
$Fe_{88}Zr_8B_3Co_1$	Ribbons	300	0.799	1.5	103.87	[100]
$Fe_{88}Zr_7B_3Co_2$	Ribbons	320	0.949	1.5	123.37	[100]
$Fe_{87}Zr_8B_3Co_2$	Ribbons	330	0.945	1.5	132.6	[100]
$Fe_{87}Zr_8B_4Co_1$	Ribbons	317	1.29	1.5	-	[101]
$Fe_{86}Zr_8B_4Co_2$	Ribbons	340	1.35	1.5	-	[101]
$Fe_{87}Zr_8B_4Er_1$	Ribbons	300	0.829	1.5	82.9	[100]
$Fe_{86}Zr_8B_4Er_2$	Ribbons	300	0.607	1.5	60.7	[100]
$Fe_{85}Zr_8B_4Er_3$	Ribbons	310	0.800	1.5	80	[100]
$Fe_{87}Zr_8B_4Sm_1$	Ribbons	300	0.705	1.5	77.55	[100]
$Fe_{86}Zr_8B_4Sm_2$	Ribbons	320	1.116	1.5	111.6	[100]
$Fe_{85}Zr_8B_4Sm_3$	Ribbons	330	0.809	1.5	88.99	[100]
$Fe_{82.5}Co_{2.75}Ni_{2.75}Zr_7B_4Cu_1$		398	1.41	1.5	166	[107]
Fe-B-M (M = Mn, Nb, Cr Cu) based alloys						
$Fe_{65}Mn_{15}B_{20}$	Ribbons	340	0.87	1.5	98	[108]
$Fe_{60}Mn_{20}B_{20}$	Ribbons	210	0.60	1.5	83	[108]
$Fe_{77}Cr_8B_{15}$	Ribbons	378	1.11	1.5	115	[110]
$Fe_{80}Cr_8B_{12}$	Ribbons	328	1.07	1.5	61	[110]
$Fe_{80.5}Nb_7B_{12.5}$	Ribbons	363	0.72	0.7	-	[109]
$Fe_{84}Nb_7B_9$	Ribbons	250	1.0	1.5		[127]
$Fe_{85}Nb_6B_9$	Ribbons	292	0.92	1.5		[127]

$Fe_{83}Nb_7B_{10}$	Ribbons	335	0.8	1.5		[127]
$Fe_{81}Ce_{13}B_6$	Ribbons	275	3.32	5	319.3	[113]
$Fe_{80.5}Ce_{12.5}B_6$	Ribbons	278	3.41	5	348.13	[113]
$Fe_{80}Ce_{12}B_6$	Ribbons	284	3.54	5	353.27	[113]
$Fe_{79.5}Ce_{11.5}B_6$	Ribbons	291	3.81	5	409.76	[113]
$Fe_{79}Ce_{11}B_6$	Ribbons	297	3.90	5	420.09	[113]
Fe-Mn-Zr based alloys						
$Fe_{86}Mn_4Zr_{10}$		228	2.51	5		[115]
$Fe_{84}Mn_6Zr_{10}$		218	2.29	5		[115]
$Fe_{82}Mn_8Zr_{10}$		210	2.87	5		[115]
$(Fe_xM_{1-x})_3Al$ (M = Cr, Mn) compounds						
$(Fe_{0.72}Cr_{0.28})_3Al$	Arc melted bulk	285	0.87	5	240	[119]
$(Fe_{0.72}Cr_{0.28})_3Al$	Ribbons	330	1.16	5	305	[119]
Fe-M (M = Sc, Cu, Zr, Y) based alloys						
$Fe_{90}Sc_{10}$	Ribbons	290	1.56	1.5	216.2	[121]
$Fe_{90}Zr_{10}$	Ribbons	243	2.96	5		[115]
$Fe_{89}Zr_{11}$	Ribbons	263	1.30	1.8	-	[94]
$Fe_{70}Cu_{30}$	NP (4.3 nm)	272	0.78	5	195	[123]
$Fe_{68}Cu_{32}$	NP (11.3 nm)	298	0.86	5	206	[123]
$Fe_{67}Cu_{33}$	NP (9.6 nm)	312	0.83	5	208	[123]
$Fe_{65}Cu_{35}$	NP (9.1 nm)	360	1.04	5	234	[123]
Other iron based alloys having four or more elements						
$(Fe_{0.66}Tm_{0.10}B_{0.24})_{96}Nb_4$	Ribbons	390	1.0	1.5	76	[125]
$(Fe_{0.59}Tm_{0.17}B_{0.24})_{96}Nb_4$	Ribbons	316	0.91	1.5	59	[125]
$(Fe_{0.58}Tm_{0.18}B_{0.24})_{96}Nb_4$	Ribbons	325	0.87	1.5	57	[125]
$Fe_{65}Mn_{15}P_{10}B_7C_3$		292	0.91	1.5	118	[128]
$Fe_{77}Ce_1Si_4Nb_5B_{12}Cu_1$		348	2.39	5	271	[126]
$Fe_{75}Ce_3Si_4Nb_5B_{12}Cu_1$		329	3.36	5	256	[126]
$Fe_{73}Ce_5Si_4Nb_5B_{12}Cu_1$		305	2.11	5	249	[126]
$Fe_{68}Ce_{10}Si_4Nb_5B_{12}Cu_1$		281	2.18	5	317	[126]
$Fe_{81.6}Mo_4Zr_{3.3}Nb_{3.3}B_{6.8}Cu_1$		235	0.75	1	-	[129]

$Fe_{60}Cr_{14}Cu_1Nb_3Si_{13}B_9$		235	0.9	3	-	[165]
$Fe_{66.3}V_{13.7}B_{12}Si_8$		335	1.03	2	93.7	[133]
$Fe_{66}Cr_8Cu_1Nb_3Si_{15.5}B_{6.5}$	Ribbons	~395	~0.9	1.5	~94	[166]
$Fe_{64}Cr_{10}Cu_1Nb_3Si_{15.5}B_{6.5}$	Ribbons	~345	0.8	1.5	~90	[166]
$Fe_{62}Cr_{12}Cu_1Nb_3Si_{15.5}B_{6.5}$	Ribbons	~290	~0.75	1.5	~85	[166]
$Fe_{60}Cr_{14}Cu_1Nb_3Si_{15.5}B_{6.5}$	Ribbons	~205	~0.65	1.5	~81	[166]
$Fe_{80}Co_2Mn_4Zr_8Nb_2B_4$	Ribbons	272	1.64	3	112	[135]
$Fe_{78}Co_4Mn_4Zr_8Nb_2B_4$	Ribbons	307	1.69	3	114	[135]
$Fe_{76}Co_6Mn_4Zr_8Nb_2B_4$	Ribbons	33	1.78	3	120	[135]
$Fe_{76}Co_8Mn_4Zr_8Nb_2B_4$	Ribbons	363	1.75	3	117	[135]
Fe based high entropy alloys						
$NiFeCoCrPd_{0.25}$	Bulk	225	0.90	5	-	[139]
$NiFeCoCrPd_{0.50}$	Bulk	295	0.88	5	-	[139]
$Fe_{0.975}CoNiCuMn_{1.025}$	Ribbons	299	0.105	1.5	14	[141]
$Fe_{0.95}CoNiCuMn_{1.05}$	Ribbons	292	0.071	1.5	10	[141]
Fe based oxides						
$Mn_{0.3}Zn_{0.7}Fe_2O_4$	NP	300	0.88	5	174	[51]
$CoFe_2O_4/CoFe_2$ composite	NP (30 nm)	290	0.923	4	3.7	[153]
$CoFe_2O_4$	NP (14 nm)	213	0.23	1.3	-	[167]
$Mn_{0.68}Zn_{0.25}Fe_{2.07}O_4$	NP (15 nm)	290	0.15	3	-	[152]
$Ni_{0.35}Zn_{0.65}Fe_2O_4$	Bulk powder (2.8 μm)	360	0.84	1.35	-	[168]
$Ni_{0.3}Zn_{0.7}Fe_2O_4$	Bulk powder (2.9 μm)	305	0.98	1.35	-	[168]
$Ni_{0.25}Zn_{0.75}Fe_2O_4$	Bulk powder (3.1 μm)	260	0.88	1.35	-	[168]
$Ni_{0.3}Zn_{0.7}Fe_2O_4$	Bulk powder	335	1.41	5	505	[169]

The cost of iron based MCM and other relevant magnetocaloric materials have been evaluated[12]. The materials cost of Fe-Ni-Cr/Mn/Mo nanoparticles is only ~ 2 % of the cost of pure Gd and $Gd_5Ge_{1.9}Si_2Fe_{0.1}$ alloys, which are benchmark magnetocaloric materials[12].

5. Mn based magnetocaloric materials

In this section, the Mn based magnetocaloric materials based on the Fe_2P crystal structure, Ni-Mn-X and Mn-T-X alloys and their magnetocaloric properties are described. Effect of annealing temperature/time on MCE are also presented.

5.1. Mn based alloys with Fe_2P crystal structure

The discovery of the "giant" MCE in $Gd_5(Si_xGe_{1-x})_4$ alloys inspired many studies of other materials with a first order magnetostructural transition, such as $La(Fe_{1-x}Si_x)_{13}$[170], Heusler alloys[58, 171] and $MnFeP_{0.45}As_{0.55}$[16]. Among the Fe_2P crystal structure based alloys, $MnFe(P_{1-x}As_x)$ alloys are the most prominent. $MnFe(P_{1-x}As_x)$ alloys can undergo a first order transition from the ferromagnetic to the paramagnetic state at the Curie temperature (T_C)[172-174]. The first order magnetic transition (FOMT) can enhance the magnetocaloric effect in the vicinity of the magnetic phase transition temperature. Active magnetic regenerators, which exhibit higher efficiency and greater cooling capability than that of Gd can be obtained by combining giant magnetocaloric materials (GMCM) possessing different T_C in series[175, 176].

There are two kinds of Fe-sites in the Fe_2P hexagonal structure, *3f* and *3g* (Fig. 17)[177]. According to the Landau phenomenological theory[178], the first order magnetic transition in Fe_2P alloys derives from the Fe atoms at the 3*f* site exhibiting meta-magnetic behavior. The strength of the exchange interaction is different for the Fe–Fe pairs in the *3f* and *3g* sites. The Fe moment at the *3f* site is sensitive to inter-site exchange interactions, which can be affected by the interatomic spacing. In Mn-Fe-P-Ge alloys, Fe is substituted by Mn and Mn can occupy both *3f* and *3g* sites, while Fe atoms can only occupy *3f* sites.[179] The magnetic moment of Fe atoms at *3f* sites responds to the change of interatomic spacing, the

total exchange interaction is governed by both Mn-Mn and Mn-Fe interactions. Recently, the crystal structure and MCE of $(Mn,Fe,T)_{1.95}P_{0.50}Si_{0.50}$ (T = Co, Ni and Cu) compounds have been investigated[180]. These compounds crystallize in the Fe_2P-type structure. Transition metal substitutions for either Mn or Fe weaken the ferromagnetic ordering and result in complex behavior in the thermal/magnetic hysteresis. It was shown by first-principles calculations that Co, Ni and Cu atoms occupy 3*f*, 3*f* and 3*g* sites, respectively.

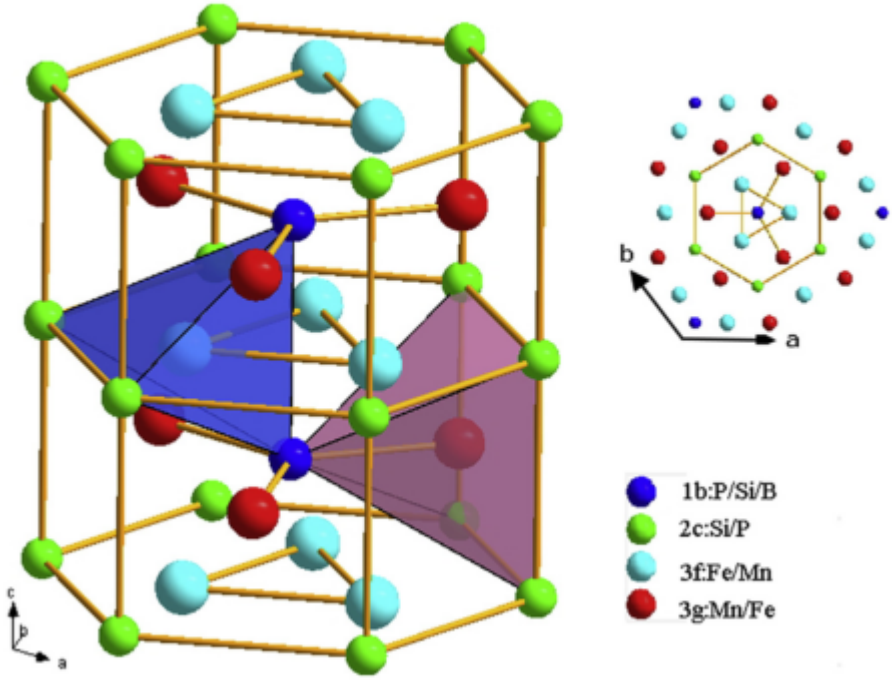

Fig. 17 Crystal structure of Fe_2P alloy at room temperature[181].

The T_C of $MnFe(P_{1-x}As_x)$ alloys was altered from 168 and 332 K by changing the P to As ratio without reduction in the values of ΔS_M[182]. However, some disadvantages are also associated with this alloy composition since As is a toxic element. By replacement of the As by Ge in Mn-Fe-P-As alloys, Mn-Fe-P-Ge alloys were developed which also exhibited attractive magnetocaloric properties[175]. These Mn-Fe-P-Ge alloys exhibited a discontinuous phase transformation from the FM to the PM state, accompanied by a large

entropy change (ΔS_M). Moreover, thermal and magnetic field hysteresis, frequently associated with the FOMT, can hamper applications in a refrigeration cycle.

5.1.1. MnAs1-xPx and MnAs1-xSbx alloys

The MnAs compound possesses a hexagonal NiAs-type structure at low temperatures and transforms to a paramagnetic phase with an orthorhombic MnP-type structure at T_C of 318 K. By partially replacing As with P, the T_C decreases from 318 K (MnAs)[183] to 303K ($MnAs_{0.98}P_{0.02}$)[184]. The maximum magnetic entropy change for an applied magnetic field of 14 T is ~ 40 $Jkg^{-1}K^{-1}$ in MnAs single crystals and approaches 50 $Jkg^{-1}K^{-1}$ in $MnAs_{0.98}P_{0.02}$ single crystals. 3d transition-metal-based compounds $MnAs_{1-x}Sb_x$ can exhibit interesting properties. The magnetic entropy change of $MnAs_{0.75}Sb_{0.25}$ reaches 15 $Jkg^{-1}K^{-1}$ at 205 K for a field change of 1 T[185]. The replacement of 10 % Sb for As reduced the thermal hysteresis and the T_C, while the giant ΔS_M values are retained[186].

5.1.2. Mn-Fe-P-Ge alloys

The $(MnFe)_2(PGe)_1$ compound crystallizes in the hexagonal Fe_2P-type structure, in which the Mn atoms occupy all the 3g sites and some of the 3f sites, the Fe atoms occupy the remaining 3f sites, and the P and the Ge atoms randomly occupy the 1b and 2c sites[187, 188]. This compound undergoes a first order magneto-structural transition from the ferromagnetic to the paramagnetic state, which is accompanied by a lattice parameter change in the hexagonal structure. A magnetic entropy change of 35 $Jkg^{-1}K^{-1}$ was observed in $Mn_{1.1}Fe_{0.9}P_{0.76}Ge_{0.24}$ ribbons at 316 K for a field change of 5 T[179].

The $Mn_{1.2}Fe_{0.8}P_{0.75}Ge_{0.25}$ melt spun ribbon showed a good ΔS_M and a small temperature hysteresis[189]. The $|\Delta S_M|$ value for the $Mn_{1.2}Fe_{0.8}P_{0.75}Ge_{0.25}$ ribbon was 20.3 $Jkg^{-1}K^{-1}$ under a magnetic field of 2 T. For higher magnetic field, the ΔS_M was not changed, however, the RCP was considerably enhanced (Fig.18).

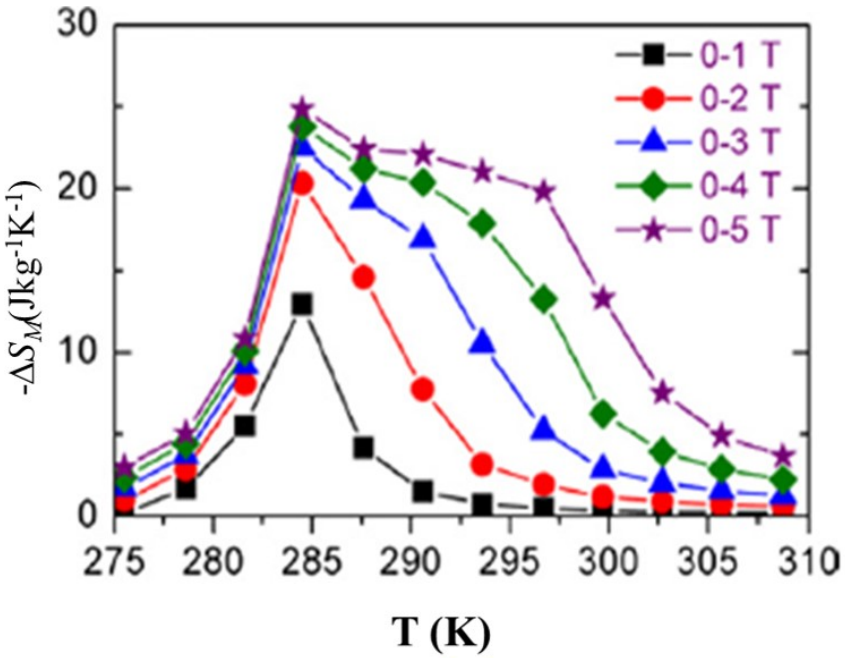

Fig. 18 -ΔS_M versus T of $Mn_{1.2}Fe_{0.8}P_{0.75}Ge_{0.25}$ for different field changes values[189]

In $Mn_{2-x}Fe_xP_{1-y}Ge_y$ alloys, the phase fraction, hysteresis of the transition, and entropy change can be affected by compositional homogeneity, particle size and annealing procedure[190].

5.1.3. Mn-Fe-P-Si-X (X = B, C, N) alloys

In order to further reduce the cost, Ge was replaced by Si, and therefore $(MnFe)_2(PSi)_1$ alloys were studied[11]. These compounds also exhibit a hexagonal Fe_2P crystal structure, the T_C increases with increasing Si content. However, these alloys reveal a new form of magnetism: the coexistence of weak and strong magnetism in alternate atomic layers, as predicted by first principles calculations[191]. The weak magnetism of Fe layers is responsible for strong coupling with the crystal lattice, while the strong magnetism in adjacent Mn-layers results in T_C suitable for near room temperature applications, tunable working temperatures and a strong reduction of undesirable thermal hysteresis. The $|\Delta S_M|$ values for $Mn_xFe_{1.95-x}P_{1-y}Si_y$ compounds (x = 1.34, 1.32, 1.30, 1.28, 1.24, 0.66, 0.66 and y = 0.46, 0.48, 0.50, 0.52, 0.54, 0.34, 0.37) were found to be ~ 18 $Jkg^{-1}K^{-1}$ for a field change of 2 T (Fig. 19). More importantly, the T_C was changed from 215 K to 350 K without affecting the value of ΔS_M.

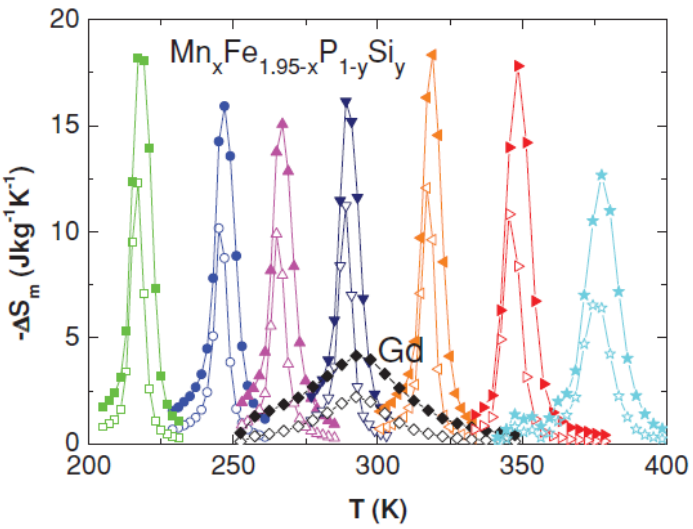

Fig. 19 The -ΔS_M values under a field change of 1T (open curves) and 2T (solid curves) for $Mn_xFe_{1.95-x}P_{1-y}Si_y$ (x= 1.34, 1.32, 1.30, 1.28, 1.24, 0.66, 0.66 and y= 0.46, 0.48, 0.50, 0.52, 0.54, 0.34, 0.37) compounds, respectively (from left to right). The data of Gd metal under a field change of 1T (open diamond) and 2T (solid diamond) are included [11].

The MCE of MnFe(P,*X*) (*X* = Si, As, Ge) alloys was measured by combining indirect ΔS_M and direct ΔT_{ad} [192]. The maximum values of ΔT_{ad} ($\Delta\mu_0 H$ = 1.1 T) and $|\Delta S_M|$ ($\Delta\mu_0 H$ = 1 T) in $Mn_{1.25}Fe_{0.7}P_{0.49}Si_{0.51}$ were ~ 2.2 K and ~8 Jkg^{-1}K^{-1}, respectively.

The longitudinal-field muon-spin relaxation technique was used to study spin correlations in $(Mn,Fe)_2(P,Si)$ compounds above the T_C[193]. The slow magnetic fluctuations and the increasing standard deviation of the local field distribution reflected the presence of short-range magnetic correlations. These correlations were expected for the deviations from Curie–Weiss behavior observed in the paramagnetic susceptibility. The MCE and structural properties of nitrogen doped $MnFe_2(PSi)$ have been reported[194]. Nitrogen addition resulted in a decrease of T_C and increase in the c/a ratio. The introduction of nitrogen in $(Mn,Fe)_2(P,Si)$ materials preserved the MCE properties with an enhancement of the mechanical stability. The magnetoelastic transition of $(Mn,Fe)_2(P,Si)$ was tuned by doping with B, C and N atoms[194, 195]. The site occupation of these light dopants in the crystal

structure was determined by neutron diffraction. B substituted Si on the 1*b* site, while C occupied the interstitial sites in the hexagonal *P-62m* structure.

$(Mn,Fe)_2(P,Si)$ compounds can experience a second-order paramagnetic to a spin-density-wave phase transition before further transformation to a ferromagnetic phase via a first-order phase transition[196]. The spin-density-wave to ferromagnetic transition can be kinetically arrested, causing the coexistence of ferromagnetic and untransformed spin-density-wave phases at low temperatures. The magnetic relaxation measurements and in-field x-ray diffraction revealed metastability of the untransformed spin density wave phase. This unusual magnetic configuration originated from strong magnetoelastic coupling and mixed magnetism in $(Mn,Fe)_2(P,Si)$ compounds. A redistribution in the electron density around the Fe atom during the FM to the PM transition resulted in the covalent bond formation which strongly reduce the magnetic moment of Fe[197]. Bruck and co-workers proposed that the $(Mn,Fe)_2(P,Si)$ compounds should contain a metalloid element and a late 3d transition metal which occupy two different crystallographic positions for better magnetocaloric properties[197].

The influence of carbon addition on the structure, magnetic phase transition and MCE of $Mn_{1.25}Fe_{0.70}P_{0.50}Si_{0.50}C_z$ and $Mn_{1.25}Fe_{0.70}P_{0.55}Si_{0.45}C_z$ compounds synthesized by high-energy ball milling and a solid-state reaction was recently examined[198]. The C doping was found to be helpful for tuning the T_C of the alloys and to reduce thermal hysteresis. It was confirmed from neutron diffraction that C substitutes P/Si on the 2c site and/or occupies the 6k interstitial site of the hexagonal Fe_2P-type structure. Both T_C and the thermal hysteresis of $(Mn,Fe)_2(P,Si)$ alloys can be tuned by Co and B co-doping without any loose of MCE and mechanical stability[199].

$Mn_zFe_{1.95-z}P_{1-x-y}Si_yB_x$ alloys exhibited a giant MCE with a limited thermal hysteresis over a temperature range from 160 to 360 K[200]. Fig 20 shows the cyclic temperature change

(ΔT_{cyclic}) of $MnFe_{0.95}P_{0.67-x}Si_{0.33}B_x$ and $MnFe_{0.95}P_{0.55}Si_{0.45}$ alloys measured by indirect and direct methods. The values of adiabatic change (ΔT_{ad}) and cyclic temperature change (ΔT_{cyclic}) may not be similar in every system. For example, $LaFe_{11.6}Si_{1.4}$ exhibited the ΔT_{cyclic} about 20% lower than the ΔT_{ad} measured during the first cycle[201]. $MnFe_{0.95}P_{0.595}Si_{0.33}B_{0.075}$ alloy does not lead to a significant difference between ΔT_{cyclic} measured by direct cyclic measurements and the ΔT_{ad} derived from an indirect calorimetric method[202]. Therefore, it is useful to distinguish between ΔT_{ad} and ΔT_{cyclic} in first order materials exhibiting large hysteresis. The coefficient of performance, which is a function of both ΔS_M and ΔT_{ad}, of MnFe(P,X) (X = As, Ge, Si, B) alloys is significantly higher than that of gadolinium[202]. The ΔT_{ad} of $Mn_{1.00}Fe_{0.95-z}Ni_zP_{0.51}Si_{0.45}B_{0.04}$ was found to be in the range of 1.7 to 1.9 K at a magnetic field of 1.1 T[199].

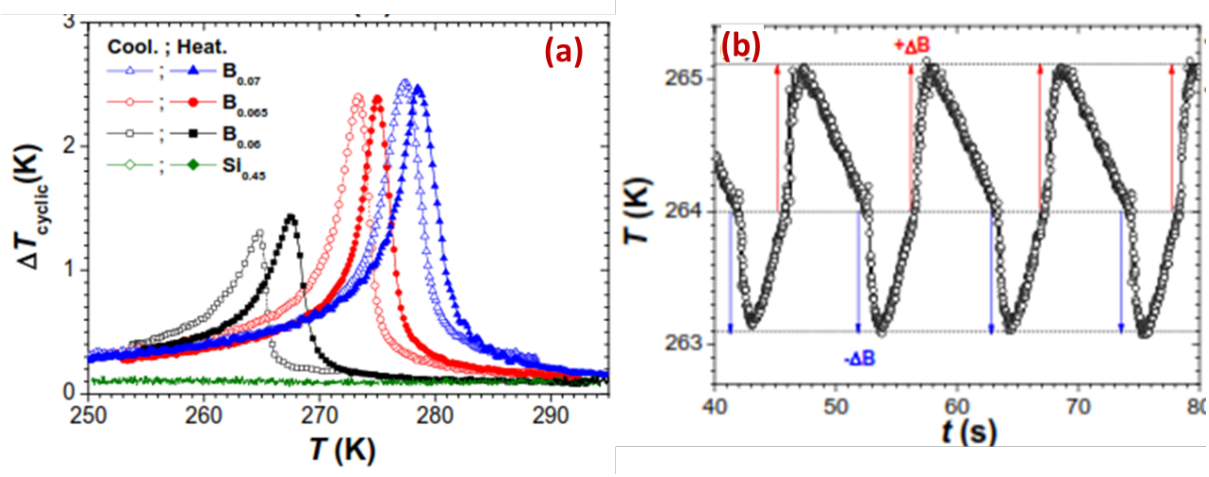

Fig. 20 (a) magnetocaloric properties (ΔT_{cyclic}) of $MnFe_{0.95}P_{0.67-x}Si_{0.33}B_x$ and $MnFe_{0.95}P_{0.55}Si_{0.45}$ measured for a magnetic field 1.1 T. Closed and open symbols are for warming and cooling, for $MnFe_{0.95}P_{0.55}Si_{0.45}$ warming and cooling curves are overlaps. (b) ΔT_{cyclic} measured by a direct method at constant starting temperatures before the magnetic field changes($|B|$ = 1 T) [200].

Crystal structure, transition temperature and magnetic entropy change of Fe_2P based magnetocaloric materials are summarized in table 2. By replacing As with Ge, ΔS_M increased, the magneto-structural transition temperature also increased also with increasing

Ge content. Ribbon samples showed higher ΔS_M but narrower working temperature span compared to powder and bulk samples. The ΔS_M of Mn-Fe-P-Si alloys was smaller than the corresponding value for Mn-Fe-P-Ge alloys. However, on the other hand, Mn-Fe-P-Si alloys showed lower thermal hysteresis.

Table 2. Crystal structure, transition temperature (T_C) and magnetic entropy change ($|\Delta S_M|$) of Fe_2P hexagonal structure based magnetocaloric materials.

Compound	**Space group**	**Sample type**	T_C **(K)**	**Applied field (T)**	$\|\Delta S_M\|$ **(Jkg^{-1}K^{-1})**	**Refs**
$MnFeP_{0.45}As_{0.55}$	P $\bar{6}$ 2m	bulk	310	5	18	[16]
$Mn_{1.1}Fe_{0.9}P_{1-x}Ge_x$						
x=0.13	P $\bar{6}$ 2m	powder	265	5	10	[203]
x=0.19	P $\bar{6}$ 2m	powder	272	5	28	[203]
x=0.19	P $\bar{6}$ 2m	bulk	255	5	14	[204]
x=0.2	P $\bar{6}$ 2m	bulk (SPS)	255	5	50	[187]
x=0.2	P $\bar{6}$ 2m	bulk	251	5	61	[205]
x=0.21	P $\bar{6}$ 2m	powder	282	5	26	[203]
x=0.21	P $\bar{6}$ 2m	ribbon	291	5	23	[203]
x=0.22	P $\bar{6}$ 2m	bulk	290	5	20	[204]
x=0.24	P $\bar{6}$ 2m	bulk	295	5	26	[206]
x=0.24	P $\bar{6}$ 2m	ribbon	315	5	35	[206]
x=0.25	P $\bar{6}$ 2m	bulk	320	5	25	[204]
x=0.26	P $\bar{6}$ 2m	powder	350	5	18	[203]
x=0.26	P $\bar{6}$ 2m	ribbon	340	5	44	[59]
x=0.3	P $\bar{6}$ 2m	ribbon	374	5	14	[59]

x=0.32	P $\bar{6}$ 2m	powder	403	5	9	[203]
x=0.32	P $\bar{6}$ 2m	ribbon	411	5	9	[59]
$Mn_{2-y}Fe_yP_{0.75}Ge_{0.25}$						
y=0.74	P $\bar{6}$ 2m	bulk	248	5	8	[204]
y=0.8	P $\bar{6}$ 2m	bulk	300	5	12	[204]
y=0.82	P $\bar{6}$ 2m	bulk	310	5	17	[204]
y=0.84	P $\bar{6}$ 2m	bulk	320	5	18	[204]
y=0.7	P $\bar{6}$ 2m	ribbon	230	5	10	[204]
y=0.76	P $\bar{6}$ 2m	ribbon	252	5	16	[204]
y=0.78	P $\bar{6}$ 2m	ribbon	275	5	15	[204]
y=0.8	P $\bar{6}$ 2m	ribbon	285	5	20	[204]
$Mn_{1.35}Fe_{0.65}P_{1-x}Si_x$						
x=0.52	P $\bar{6}$ 2m	powder	253	1.5	7	[207]
x=0.54	P $\bar{6}$ 2m	powder	275	1.5	4	[207]
x=0.55	P $\bar{6}$ 2m	powder	280	1.5	4.2	[207]
x=0.56	P $\bar{6}$ 2m	powder	296	1.5	3.3	[207]
x=0.57	P $\bar{6}$ 2m	powder	289	1.5	3.5	[207]
x=0.56 (quenching)	P $\bar{6}$ 2m	powder + quenching	278	1.5	4.3	[207]
x=0.57 (quenching)	P $\bar{6}$ 2m	powder + quenching	293	1.5	4.2	[207]
$Mn_xFe_{1.95-x}P_{1-y}Si_y$						
x=1.34 & y=0.46	P $\bar{6}$ 2m	powder	213	2	18	[11]
x=1.32 & y=0.48	P $\bar{6}$ 2m	powder	245	2	16	[11]

x=1.3 & y=0.5	P $\bar{6}$ 2m	powder	265	2	15	[11]
x=1.28 & y=0.52	P $\bar{6}$ 2m	powder	288	2	17	[11]
x=1.24 & y=0.54	P $\bar{6}$ 2m	powder	315	2	19	[11]
x=0.66 & y=0.34	P $\bar{6}$ 2m	powder	350	2	17	[11]
x=0.66 & y=0.37	P $\bar{6}$ 2m	powder	375	2	13	[11]
$Mn_{1.25}Fe_{0.70}P_{0.50}Si_{0.50}C_z$						
Z= 0	P $\bar{6}$ 2m	powder	256	2	21.01	[198]
Z=0.05	P $\bar{6}$ 2m	powder	275	2	13.02	[198]
Z=0.10	P $\bar{6}$ 2m	powder	260	2	11.19	[198]
Z=0.15	P $\bar{6}$ 2m	powder	270	2	9.21	[198]
$Mn_{1.25}Fe_{0.70}P_{0.55}Si_{0.45}C_z$						
Z=0	P $\bar{6}$ 2m	powder	202	2	24.64	[198]
Z=0.025	P $\bar{6}$ 2m	powder	229	2	20.99	[198]
Z=0.050	P $\bar{6}$ 2m	powder	224	2	19.28	[198]
Z=0.075	P $\bar{6}$ 2m	powder	226	2	18.38	[198]
$MnFeP_{0.89-x}Si_xGe_{0.11}$						
x = 0.22	P $\bar{6}$ 2m		270		27	[208]
x = 0.26	P $\bar{6}$ 2m		292		27	[208]
x = 0.30	P $\bar{6}$ 2m		288		27	[208]
x = 0.33	P $\bar{6}$ 2m		260		45	[208]

5.1.4. Magneto-structural transition in Mn-Fe-P-Ge alloys

By increasing Ge content, a change from first order to second order transition was observed, the effect of Ge content on phase transition in Mn-Fe-P-Ge alloys was studied. MCM can exhibit either first order or second order transition. The first order transition can be

antiferromagnetic (MnSb based alloys), martensitic (Heusler alloys) or magneto-structural (Fe_2P based with abrupt lattice parameter change). For a first order transition the first derivatives of Gibbs free energy is discontinuous, therefore, the change in entropy corresponds to latent heat and higher ΔS_M can be expected. In the *3d* series (*i.e.*, Fe, Co, Cr, Mn, Ni, Zn and Cu), orbital contraction affects the ability of the *d* electrons to contribute to bonding. Metals and alloys formed from these *3d* elements can be either ferromagnetic or antiferromagnetic.

In Mn-Fe-P-Ge alloys, the ferromagnetic behavior is mainly derived from the Fe atoms[209]. Based on the Bethe-Slater curve, an asymmetric dependence of the exchange interactions can be induced by fluctuations in atomic spacing and other disorder at defects and interfaces[210], therefore the inter-spin interactions decided the transition temperature (T_C). The spins of the electrons pair and a bond is formed at short interatomic distances or with strong overlap between atomic orbitals. When the overlap between orbitals is poor, unpaired electrons become favorable at larger interatomic distances. The critical effect of Ge is to change the interatomic spacing (lattice parameter), therefore the T_C can be tuned by Ge content.

By tuning the Ge content, the magnetic transition in Mn-Fe-P-Ge alloys can be either first order or second order[27, 205]. The parameter of phase transition in Bean-Rodbell model was applied to determine the order of the magnetic transition [210]. When the phase parameter is larger than 1, a first-order magnetic transition with a sudden volume change of the unit cell can be expected at T_C. A change of lattice parameter due to the decrease of magnetization can be observed, since the lattice parameters are influenced by the extent of order of the magnetic spins. By further heating, a discontinuous decrease of magnetization to zero was observed, accompanied by an abrupt change in lattice parameters. Hence, a discontinuous loss of magnetization, which is first order, occurred[210, 211].

The low temperature and high temperature x-ray diffraction with Rietveld refinement were applied to study the magnetic transition in Mn-Fe-P-Ge alloys. In samples with Ge content lower than 0.32, sudden lattice parameter change was observed. By increasing Ge content, the interatomic spacing increases, leading to weakening of the interactions between Fe atoms at *3f* sites and the absence of metamagnetism above a critical Ge content. Therefore, the magnetic transition changes from first to second order at x=0.32 in $Mn_{1.1}Fe_{0.9}P_{1-x}Ge_x$ alloys.

5.1.5. Effect of annealing time and temperature on the MCE

The phase transition and magnetocaloric behavior of $Mn_{1.1}Fe_{0.9}P_{0.75}Ge_{0.25}$ powders annealed between 1023 K and 1323 K for 3h, 9h and 15h were studied (Fig. 21) [212]. The effect of annealing temperature and time on T_C, thermal hysteresis, ΔS_M and RCP were investigated and optimum annealing parameters determined. The mass fraction of the parent phase was found to be sensitive to both annealing temperature and time. The annealing at 1123 K for 9h resulted a maximum RCP, while maximum ΔS_M was obtained after annealing at 1223 K for 9h.

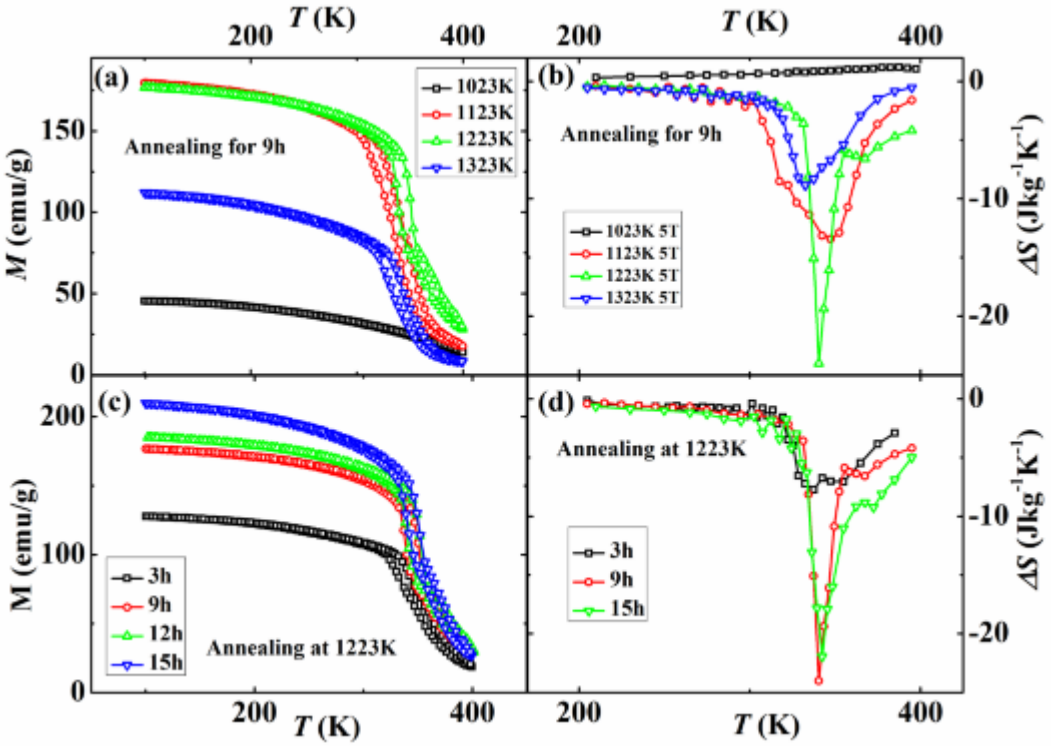

Fig. 21 Temperature dependence of the magnetization at a magnetic field of 2 T for the $Mn_{1.1}Fe_{0.9}P_{0.75}Ge_{0.25}$ powders (a) annealed at different temperature (b) corresponding ΔS_M as a function of temperature (c) annealed at different time (d) corresponding ΔS_M as a function of temperature[212].

With increasing annealing temperature, the lattice parameters of Fe_2P-type phase increase from 5.7988(1)Å to 6.0785(2)Å and from 3.3218(1)Å to 3.4727(2)Å for the $Mn_{1.15}Fe_{0.85}P_{0.50}Si_{0.45}B_{0.05}$ alloys[181]. The T_C and $|\Delta S_M|$ from increased form 233 K to 244 K and from 8.8 $Jkg^{-1}K^{-1}$ to 17.0 $Jkg^{-1}K^{-1}$ ($\Delta\mu_0 H = 2$ T), respectively. The T_C of $Mn_{1.00}Fe_{0.95}P_{0.595}Si_{0.33}B_{0.075}$ samples was tuned between 265 and 298 K by annealing the alloys at different temperatures between 1273 and 1373 K, while, the T_C was not significantly affected with annealing time (Fig 22)[213]. The $|\Delta S_M|$ under a field change of 1 T increased from 2.7 to 6.5 $Jkg^{-1}K^{-1}$ by increasing the annealing temperature from 1273 to 1373 K.

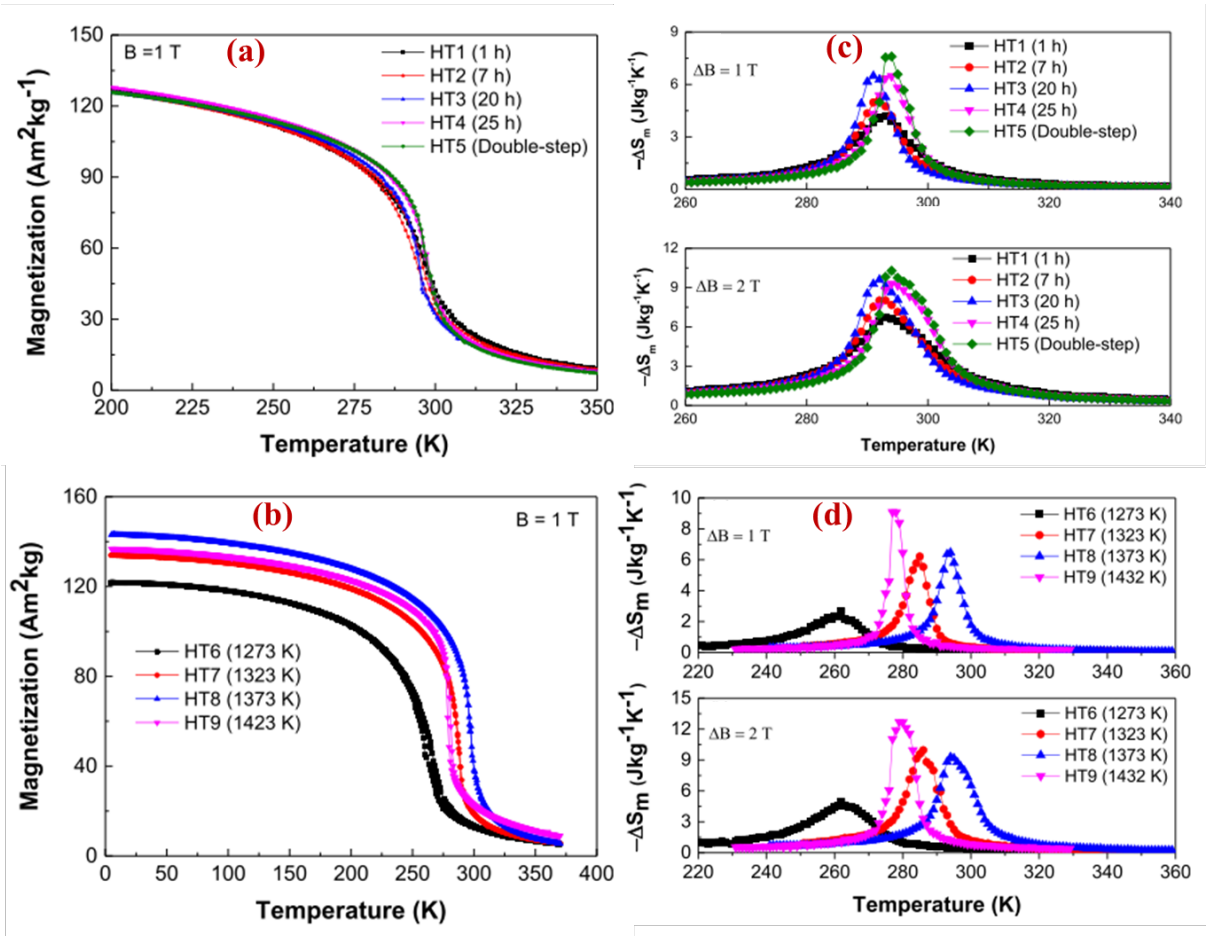

Fig. 22 Temperature dependence of magnetization during heating and cooling at a magnetic field of 1 T for $Mn_{1.00}Fe_{0.95}P_{0.595}Si_{0.33}B_{0.075}$ alloys (a) annealed for different times (b) annealed at different temperatures. The entropy change as a function of temperature for $Mn_{1.00}Fe_{0.95}P_{0.595}Si_{0.33}B_{0.075}$ (c) annealed for different times (d) annealed at different temperatures[213].

5.1.6. Thermal hysteresis

The practical impact of hysteresis is a key requirement for the development of potential magnetocaloric material. The order of the transition also plays a crucial role. As discussed in introduction, in general, FOMT materials exhibits hysteresis and a SOMT materials shows no or negligible hysteresis. Using MCE properties that measured ignoring the hysteresis effects can result higher temperature spans for a given cooling power. Engelbrecht et al., reported that the hysteresis in $MnFeP_{1-x}As_xMnFeP_{1-x}As_x$ compounds may significantly reduce their performance in a practical AMR[214]. In $MnFeP_{1-x}As_x$, a thermal hysteresis of 0.5–3.9 K with magnetic field of 1.5 T is responsible for a decrease from a ΔT_{ad} of 5 K for the full effect to a ΔT_{cyclic} of only 3.1 K for the cyclic MCE. The hysteresis of a material can be controlled during material synthesis by controlling/optimizing process parameters. The origins of hysteresis can be divided into “intrinsic” contributions associated to the electronic properties and “extrinsic” influences associated to microstructure[215] In Mn–Fe–P–Si systems, the hysteresis can be minimized by changing the ratio of Mn/Fe and/or P/Si. Fig 23 shows Curie temperature and thermal hysteresis of $(Mn,Fe,T)_{1.95}P_{0.50}Si_{0.50}$ as function of the transition metal (Co, Mn, Cu) content [180].

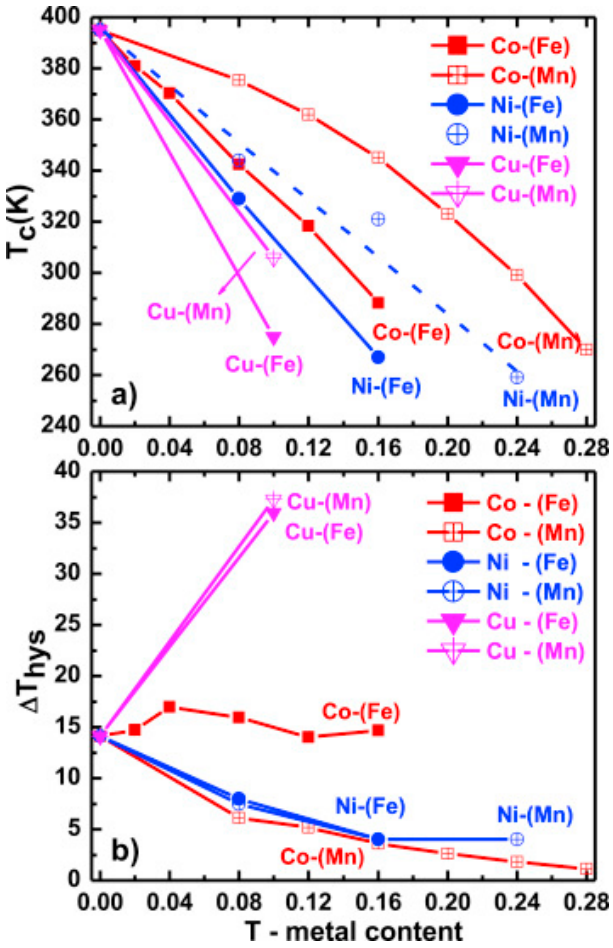

Fig. 23 (a) Curie temperature and (b) thermal hysteresis as function of the transition metal (Co, Mn, Cu) content in $(Mn,Fe,T)_{1.95}P_{0.50}Si_{0.50}$[180].

The T_C decreases by increasing the substitution of transition metal. In $(Mn,Fe,T)_{1.95}P_{0.50}Si_{0.50}$ compounds, thermal hysteresis decreases and increases with Ni and Cu substitutions, respectively. Moreover, Co substitutions for Mn and Fe decreases and no changes in thermal hysteresis, respectively [180]. The change in the hysteresis is related to electronic configuration of the atoms since Co and Ni has incomplete 3d orbital same as Fe and Mn while Cu has filled 3d shell and unfilled 4S shell.

The thermal hysteresis was studied for $Mn_{1.1}Fe_{0.9}P_{0.75}Ge_{0.25}$ samples. In samples annealed at 1223 K for 9h, the thermal hysteresis is ~14 K, for the first, second and third cycles (Fig. 24

(a)). Thermal hysteresis (ΔT) of samples annealed at 1123 K, 1223 K and 1323 K for 9h are plotted in Fig. 24 (b).

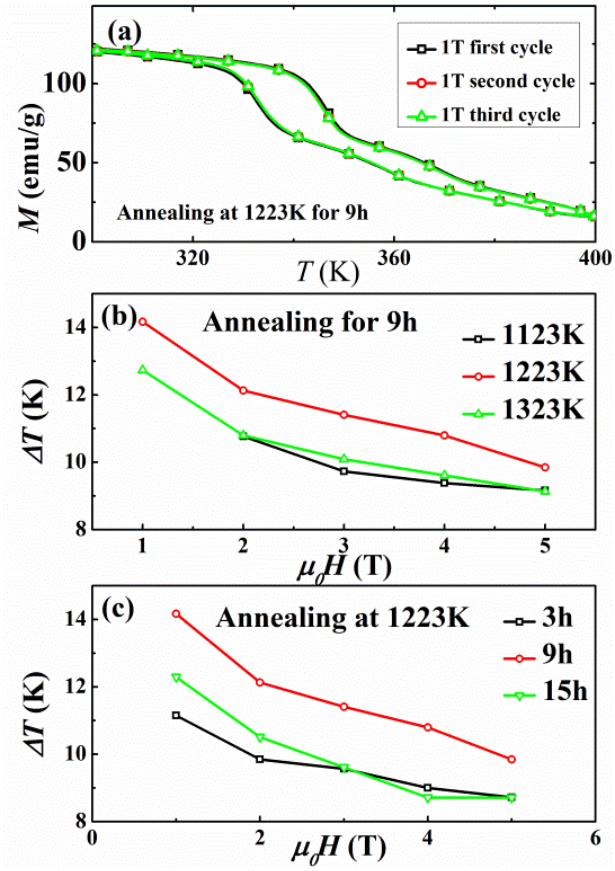

Fig. 24 (a) M vs T curves in 1 T field for the first, second and third cycles (b) Field dependence of thermal hysteresis of samples annealed at 1123 K, 1223 K and 1323 K for 9h. (c) Field dependence of thermal hysteresis of samples annealed at 1223 K for 3h, 9h and 15h.

With increasing applied magnetic field, ΔT decreases from 14 K to 9 K for samples annealed at 1223K. The ΔT increases from 1123 K to 1223 K and subsequently decreases.

It exhibits a peak value of 14 K at 1223 K, which also exhibits high ΔS_M and RCP. In a first order transition, higher ΔS_M is usually accompanied by larger thermal hysteresis. Fig. 24 (c) shows the thermal hysteresis for samples annealed at 1223 K for 3h, 9h, 12h and 15h. The ΔT decreased with increasing magnetic field and decreasing annealing time. This change in MCE induced by annealing conditions was due to the variation in volume fraction of the

existing phase. Thermal hysteresis of $Mn_{1.15}Fe_{0.85}P_{0.50}Si_{0.45}B_{0.05}$ alloys decreased with increasing annealing temperature[181].

5.2. Ni-Mn-X (X= Ga, Sn, In, Sb) alloys

The Heusler alloys (Ni-Mn-X) (Ga, Sn, In, Sb) exhibits both a structural transformation (T_m) and a magnetic transition (T_C), these transition can be tuned by changing the ratio of Ni:Mn:X[8, 216]. Heusler-type alloys exhibit high hysteresis and large MCE. Reducing hysteresis with a minor change in the MCE of these alloys is the main focus of ongoing research[217, 218]. Ni–Mn–In–(Co) Heusler alloys exhibited ΔT_{ad} in the range of -3.6 to -6.2 K under a magnetic field of 2 T[219].

The MCE of Polycrystalline $Ni_{50}Mn_{37}Sn_{13}$, $Ni_{49.5}Co_{0.5}Mn_{37}Sn_{13}$, $Ni_{48.5}Co_{1.5}Mn_{37}Sn_{13}$, $Ni_{48.3}Co_{1.7}Mn_{37}Sn_{13}$, $Ni_{47.5}Co_{2.5}Mn_{37}Sn_{13}$ and $Ni_{48}Co_2Mn_{38}Sn_{12}$ alloys was reported. The $Ni_{48}Co_2Mn_{38}Sn_{12}$ alloy composition was identified as the optimum alloy composition for near room temperature magnetic cooling applications with ΔS_M of 32 $JKg^{-1}\text{-}K^{-1}$[58]. Polycrystalline $Ni_{55}Mn_{18+x}Ga_{27-x}$ (x = 0, 1, 2) alloys exhibit coupled magnetostructural transformation for x= 1 and 2[220]. ΔT_{ad} values of 1.47 K and 1.57 K, and $|\Delta S_M|$ values of 6.54 $Jkg^{-1}K^{-1}$ and 10.15 $Jkg^{-1}K^{-1}$, under the field change of 1.5 T, were achieved in $Ni_{55}Mn_{19}Ga_{26}$ and $Ni_{55}Mn_{20}Ga_{25}$ alloys, respectively[220]. The martensitic transition temperature was found to decrease monotonically with increasing Co content in $Ni_{50-x}Co_xMn_{38}Sb_{12}$ (x = 0, 2, 3, 4, 5)[216]. The maximum $|\Delta S_M|$ of 34 $Jkg^{-1}K^{-1}$ was found for x = 5 at 262 K for a field change of 5 T. A $|\Delta S_M|$ of 18.7 $Jkg^{-1}K^{-1}$ under a field of 5 T was achieved in a $Ni_{41}Ti_1Co_9Mn_{39}Sn_{10}$ alloy at room temperature[221]. This alloy showed good compressive properties and stable martensitic transformation during thermal cycling, which is advantageous for magnetocaloric applications.

5.3. Mn-T-X (T = Ni, Co and X = Si, Ge) alloys

The main challenge in the use of Mn-T-X (T = Ni, Co and X = Si, Ge) compounds for MCE applications is that the structural transformation temperature (Tt) is higher than the magnetic-ordering temperatures of both hexagonal and orthorhombic phases[222, 223]. The ΔS_M of Mn-T-X (T = Ni, Co and X = Si, Ge) compounds, such as $MnNi_{0.77}Fe_{0.23}Ge$ (-7 and -19 $Jkg^{-1}K^{-1}$)[224], $Mn_{0.82}Fe_{0.18}NiGe$ (-13 and -31 $Jkg^{-1}K^{-1}$)[224], $Mn_{0.9}Co_{0.1}NiGe$ (-15 and -40 $Jkg^{-1}K^{-1}$)[225], $MnCoGe_{0.95}Ga_{0.05}$ (-14 and -34 $Jkg^{-1}K^{-1}$)[226], $(MnNiSi)_{65}(Fe_2Ge)_{35}$ (-15.2 and -36.9 $Jkg^{-1}K^{-1}$)[60] $Mn_{0.74}Fe_{0.26}NiSi_{0.7}Ge_{0.3}$ (-17 and -37 $Jkg^{-1}K^{-1}$)[222], and $Mn_{0.64}Fe_{0.36}NiSi_{0.7}Ge_{0.3}$ (-15 and -34 $Jkg^{-1}K^{-1}$)[222] under magnetic field changes of 2 and 5 T, respectively, was found to reasonably good. In ongoing research, near room temperature MCE was obtained for the composition of $(MnNiSi)_{1-x}(Fe_2Ge)_x$, x in the range from 0.32 to 0.36. The structural transition from the high temperature hexagonal phase to the low temperature orthorhombic phase was coupled with a magnetic transition from the paramagnetic to the ferromagnetic phase to achieve the giant magnetostructural transition. It was found that these alloys are useful for a wide temperature range, since T_t can be tuned from 365 K to 200 K by varying Fe_2Ge content in the range from x = 0.32 to 0.36. For example, the $|\Delta S_M|$ of $(MnNiSi)_{0.66}(Fe_2Ge)_{0.34}$ alloy was found to be 57 $Jkg^{-1}K^{-1}$ at 295 K.

6. Critical analysis of iron based magnetocaloric materials

Critical analysis of MCM is of high interest, since it is directly related to the MCE[19, 227]. The critical exponents α, β, γ and δ associated to specific heat, spontaneous magnetization, magnetic susceptibility and critical isotherm, respectively, are related to the magnetic entropy change at the transition temperature ($T = T_C$). The ΔS_M can be expressed by the relation[228]:

$$\Delta S_M = \frac{-a\beta\gamma}{b^{\frac{\beta+\gamma\beta}{\beta+\gamma}}\left(2\beta+\gamma-1\right)} H^{\frac{\beta-1}{\beta+\gamma}+1} = AH^n \qquad (10)$$

Where a and b are constants, A is a function of the critical exponents, and n = 1+ [(β−1)/(β+γ)]. In addition, the RCP can be expressed by a power law of $RCP \propto H^N$, ($N = 1+1/\delta$). Therefore, the critical exponents are useful to evaluate the MCE at high fields, as well as to compare RCP and ΔS_M values obtained by various investigators using different applied fields. It can also be used to understand the magnetic phase transition and the nature of ordering around T_C. In the critical region, the equation of state $(M)^{1/\beta} = A(T - Tc)/Tc + B(H/M)^{1/\gamma}$ was proposed by Arrott and Noakes, where A and B are constants. Arrott and Noakes determined the critical exponents of pure Ni as $1/\gamma = 0.75$ and $1/\beta = 2.5$ from the magnetization curves at fields up to 1.8 T near T_C. $(H/M)^{0.75}$ vs $M^{2.5}$ plots for fixed temperature lie on straight lines which are parallel to each other[229]. These plots are referred to as the Arrott-Noakes plots.

According to Banerjee's criterion, the order of the magnetic phase transition can be determined from the slope of the magnetic isotherms. A negative (positive) slope of the Arrott plot M^2 versus H/M, suggests that the magnetic phase transition is first (second) order[230]. Theoretical models such as the 3D-Heisenberg model, the 3D-Ising model and the tricritical model) are useful to explain the magnetic behaviour at the ordering temperature. The scaling hypothesis can be used to calculate the critical exponents β, γ and δ near T_C. The critical exponents (β, γ) and T_C can be accurately determined by the Kouvel-Fisher (KF) method[19, 52, 231], equations (11) and (12).

$$\frac{Ms(T)}{dMs(T)/dT} = \frac{T - Tc}{\beta} \qquad (11)$$

$$\frac{\chi_0^{-1}(T)}{d\chi_0^{-1}(T)/dT} = \frac{T - Tc}{\gamma} \tag{12}$$

According to this method, the graph of $M_s\left(dM_s/dT\right)^{-1}$ versus T and $\chi_0^{-1}\left(d\chi^{-1}/dT\right)^{-1}$ versus T should display straight lines, with slopes of 1/ β and 1/ γ, respectively. The value of T_C can be determined by extrapolation of these straight lines to the ordinate equal to zero on the T axis. Widom's scaling relation[232] $\delta = 1 + (\gamma/\beta)$ is useful to determine the third exponent δ.

The critical behavior near T_C can also be studied by a scaling hypothesis; in the critical region, the magnetic equation of state[19, 52, 233], can be written as

$$m = f_{\pm}(h) \tag{13}$$

where m is the scaled magnetization, $m = |\varepsilon|^{-\beta} M(H,\varepsilon)$, h is the scaled field $h = |\varepsilon|^{-\beta\delta} H$ and ε is the reduced temperature *(T-Tc)/Tc*. Eq. 13 suggests that *m* as a function of *h* yields two curves: $f_+(h)$ for $T > T_C$ and $f_-(h)$ for $T < T_C$. The critical exponents for some relevant materials is presented in the table 3.

Table 3. Critical exponents of some magnetocaloric materials

Model/material	α	β	γ	δ	Ref.
3D-Heisenberg	-0.115	0.365	1.336	4.8	[233]
3D-Ising	0.11	0.325	1.241	4.82	[233]
Mean-field theory	0.0	0.5	1.0	3.0	[233]
Tricritical mean field	0.5	0.25	1	5	[234]
$(Fe_{70}Ni_{30})_{89}B_{11}$ (KF)	-0.055	0.364	1.319	4.623	[19]
$(Fe_{70}Ni_{30})_{92}Mn_8$ (KF)	-	0.319	1.195	4.71	[52]
$Fe_{90}Zr_{10}$ (KF)	-	0.368	1.612	5.32	[235]
$Fe_{85}Ni_5Zr_{10}$ (KF)	-	0.425	1.323	4.11	[235]

$Fe_{77}Co_{5.5}Ni_{5.5}Zr_7B_4Cu$ (KF)	-	0.53	1.34	3.5	[227]
$Fe_{89.5}Zr_{10.5}$ (KF)	-0.93	0.47	2.0	5.31	[236]
$Fe_{91}Zr_7B_2$	-	0.325	1.38	-	[237]
$Fe_{88}Zr_8B_4$		0.39	1.38		[237]
$Fe_{87}Zr_6B_6Cu$		0.40	1.38		[237]
$Fe_{86}Mn_4Zr_{10}$		0.369	1.368		[238]
$Fe_{84}Mn_6Zr_{10}$		0.341	1.358		[238]
$Fe_{82}Mn_8Zr_{10}$		0.365	1.387		[238]
$Fe_{80}Mn_{10}Zr_{10}$		0.368	1.384		[238]
$Fe_{78}Mn_{12}Zr_{10}$		0.359	1.378		[238]
$Fe_{80}P_{13}C_{10}$		0.38±0.02	1.30±0.05	4.47±0.05	[239]
$Fe_{75.5}Cr_4B_{13}Si_{7.5}$		0.366	1.286		[240]
$Fe_{20}Ni_{60}P_{14}B_6$		0.39	1.33	4.45	[241]
$Fe_{40}Ni_{40}P_{14}B_6$		0.38	1.31	4.46	[242]
$Fe_{88}Zr_8B_4$ (MAP)	-	0.39	1.38	-	[237]
Er_2Fe_{17} (MAP)	-0.59	0.42	1.74	5.1	[81]
Fe	-0.11	0.389	1.333	4.35	[233]
Ni	-0.10	0.378	1.34	4.58	[243]
Co	-0.095	0.435	1.225	3.35	[233]
Gd	0.04	0.381	1.196	3.615	[233]

7. Modeling of the magneto-structural transition and magnetocaloric property

Modeling of the relevant magneto-structural transition of Mn based alloys with Fe_2P crystal structure, using Landu theory, Arrott plots and the Bean- Rodbell model are elucidated.

7.1. Landau Theory

A Landau expansion with respect to magnetization (M) can be used to express the magnetic free energy F (M, T) [59]. In Mn-Fe-P-Ge alloys, the Landau expansion can be used to

describe the magnetic behavior near T_c by assuming that the resulting splitting of the subbands is much smaller than their width. The Landau expansion is:

$$F(M,T) = \frac{a_1(T)}{2}M^2 + \frac{a_3(T)}{4}M^4 + \frac{a_5(T)}{6}M^6 + ... - \mu_0 HM \quad (14)$$

By fitting the M vs H curves at different temperatures in Eq. 14, the value of the Landau coefficients a_1, a_3 and a_5 can be determined as a function of temperature.

$$\mu_0 H = a_1(T)M + a_3(T)M^3 + a_5(T)M^5 \quad (15)$$

The transition temperatures can be identified by the temperature dependence of the Landau coefficients a_1 (T), a_3 (T) and a_5 (T). The Landau coefficients a_1 and a_5 are positive at T_C. However, a_3 can be positive or negative depending on the order of the transition. $a_3 > 0$ and $a_3 < 0$ corresponding to a second order and first order transition, respectively [209, 244].

Fig. 25 shows the plots of a_1, a_3 and a_5 as a function of temperature for Polycrystalline $Mn_{1.1}Fe_{0.9}P_{1-x}Ge_x$ (x= 0.13, 0.19, 0.21, 0.26 and 0.32) powder and $Mn_{1.1}Fe_{0.9}P_{0.79}Ge_{0.21}$ (Ge0.21R) ribbon alloys. These $Mn_{1.1}Fe_{0.9}P_{1-x}Ge_x$ (x= 0.13, 0.19, 0.21, 0.26 and 0.32) powder samples are designated as Ge0.13P, Ge0.19P, Ge0.21P, Ge0.26P and Ge0.32P, respectively. In the Ge0.13P powder sample, there are two minimum values in the a_1 curve, indicating two transitions, which is consistent with the M vs. T results. Both the values of T_0 are larger than T_C and a_5 is positive in the vicinity of these two temperatures, indicating that these two transitions are first-order (Fig. 25 (a)). In Fig. 25 (b-d), the T_0 values are larger than T_c, while a_5 is positive in the vicinity of these two temperatures, verifying that the transition in Ge0.19P, Ge0.21P and Ge0.21 R alloys are also first order. In Fig. 25 (e), T_0 and T_c are quite similar. Therefore, the Arrott plot was applied to identify the order of

magnetic transition in Ge0.26 powders. The Landau coefficients of Ge0.32 powders are shown in Fig. 25 (f), T_0 is smaller than T_c, indicating a second order transition.

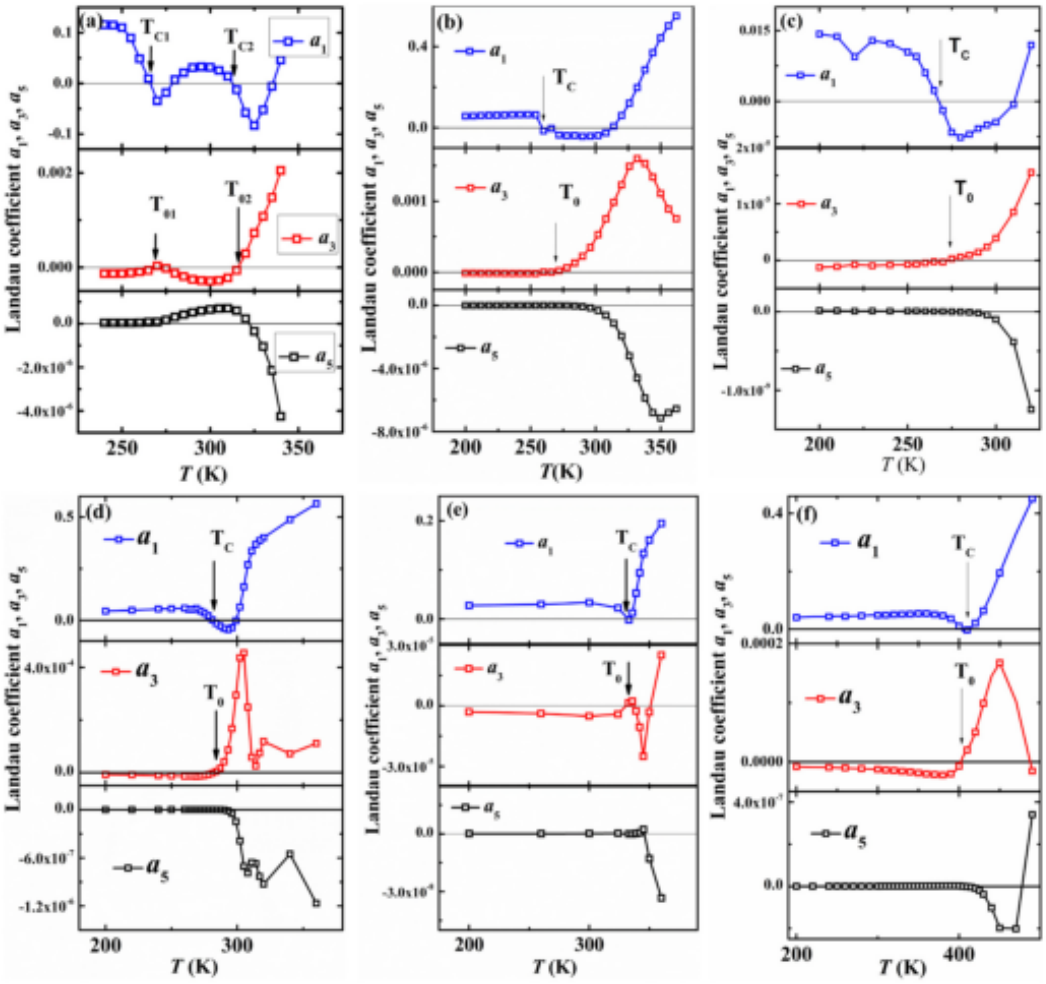

Fig. 25 Temperature dependence of Landau coefficients a_1, a_3 and a_5 for (a) $Mn_{1.1}Fe_{0.9}P_{0.87}Ge_{0.13}$ powder, (b) $Mn_{1.1}Fe_{0.9}P_{0.81}Ge_{0.19}$ powder, (c) $Mn_{1.1}Fe_{0.9}P_{0.79}Ge_{0.21}$ powder, (d) $Mn_{1.1}Fe_{0.9}P_{0.79}Ge_{0.21}$ ribbon, (e) $Mn_{1.1}Fe_{0.9}P_{0.74}Ge_{0.26}$ powder and (f) $Mn_{1.1}Fe_{0.9}P_{0.68}Ge_{0.32}$ powder alloys[203, 212].

7.2. Arrott Plots

Arrott plot, which is M^2 versus H/M isotherms were used to identify the ordering of the magnetic phase transition in $Mn_{1.1}Fe_{0.9}P_{0.74}Ge_{0.26}$ and $Mn_{1.1}Fe_{0.9}P_{0.68}Ge_{0.32}$ powder samples. The negative slope of Arrott plot of the Ge0.26 powder sample, indicated a first order magnetic transition, while the positive slope of the Arrott plot in the Ge0.32 powder sample

suggested a second order magnetic phase transition. In these Mn-Fe-P-Ge powder alloys, The critical composition range for the cross over from first order to second order magnetic transition was experimentally determined to be in the range of 0.3<x<0.32.

7.3. Bean-Rodbell model

In Mn-Fe-P-As alloys, the ferro-paramagnetic transition can be changed from first order to second order by tuning As content[245, 246]. This transition can also be tuned by magnetic field or temperature, the transition temperature (T_C) is quite sensitive to Ge and Mn content, which indicates that the exchange energy and T_C are a strong function of interatomic spacing.[202] In Mn-Fe-P-Ge alloys, the critical composition of the phase transition was studied to simultaneously achieve high ΔS_M and RC. The experimental M vs T results for the Ge0.3 ribbons show a thermal hysteresis of ~10 K, which is a sign of a first order transition. Fig. 26 shows the fitting of the calculated magnetic entropy change of Ge0.26, Ge0.3 and Ge0.32 ribbons at 5 T external magnetic field using the experimental results.

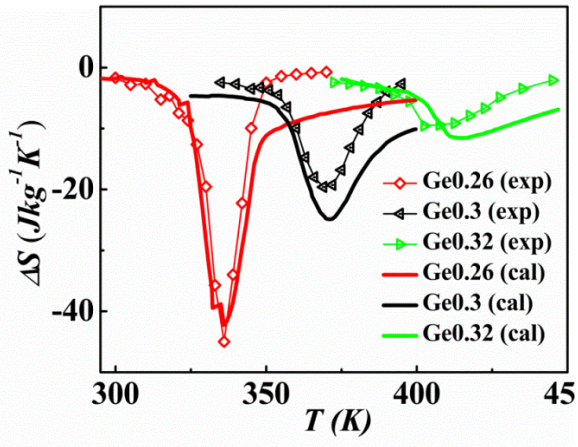

Fig. 26 Theoretical and experimental ΔS_M versus T for magnetic field change of 5T in Ge0.26, Ge0.3 and Ge0.32 ribbons.

The calculated ΔS_M showed a good fit with the experimental results for the Ge0.26R alloy. For other alloy compositions, there was reasonable fit between the model and experiment for temperatures less than T_c.

The combination of: (a) large ΔS_M and ΔT_{ad} at intermediate applied magnetic fields, (b) low hysteresis, (c) readily tunable T_C and (d) cost effective, readily available and non-toxic materials; makes the Fe_2P family highly promising for magnetic refrigeration applications[55, 189, 190, 192]. Astronautics Corporation of America, BASF and Haier presented a prototype of a wine cooler refrigerated by a magnetocaloric heat pump, which was the first consumer fridge to use magnetic refrigeration technology. They used Mn-Fe-P-Si alloys as the working material, the material heated up when exposed to a magnetic field and cooled down when removed from the magnetic field. This prototype of wine cooler showed a remarkable 35% greater energy efficiency than the cooler based on vapor compression, also, operates with less vibration and noise.

Besides magnetic cooling, MCE can be used in medical applications, e.g., controllable release and delivery of drugs or biomedical substances and magnetic hyperthermia applications in cancer treatment[247-253]. Therapies based on magnetic hyperthermia have already been proven in several types of cancer e.g., breast carcinoma or brain tumor prostate cancer[254-256].These applications are based on local cooling and local heating by alternating magnetic fields. For hyperthermia applications, it is necessary that the MCE nanomaterials should not be toxic, and T_C must be in the range of 42 to 46 °C. Therefore, iron based MCE nanomaterials which are comparatively less toxic compared to rare earth based materials may be useful for hyperthermia applications.

Summary

Magnetic cooling using MCE has high potential in addressing the critical world-wide demand for environmentally friendly, green and energy efficient thermal management. Rare

earth based materials possess high ΔS_M values but have very low potential for large scale commercialization due to their limited availability, high cost and poor corrosion resistance. Low cost and readily available Fe based magnetic materials are therefore attractive for magnetic cooling. Fe-Ni and $Fe_{17}R_2$ based nanoparticles are more attractive due to their large temperature span, tunable Curie temperature, low cost, easy availability, corrosion resistance, negligible hysteresis and high relative cooling power, though additional research is needed to improve the ΔS_M. Such nanoparticles have additional advantage as they have potential to disperse in a suitable fluid and can be used for self-pumping magnetic cooling applications. However, the stability of the dispersion of metallic nanoparticles in the fluid is a challenge due to their high density, therefore appropriate surface coating of the nanoparticles is required for long term stability. For Mn based MCM, MnFePGe and MnFeSiGe compounds are more promising for near room temperature applications due to their low cost, non-toxic nature and good MCE properties. However, the thermal hysteresis in these Mn based compounds needs to be reduced for cyclic applications. The transition temperature of Mn based materials can be tuned in a large temperature and hysteresis can be minimized by adjusting the percentage of Mn, Fe, P or Si.

Acknowledgments

This research is supported by the National Research Foundation, Prime Minister's Office, Singapore under its Campus for Research Excellence and Technological Enterprise (CREATE) programme.

References

[1] Khan MIH. Conventional Refrigeration Systems Using Phase Change Material: A Review. International Journal of Air-Conditioning and Refrigeration. 2016;24:1630007.
[2] Gschneidner KA, Pecharsky VK. MAGNETOCALORIC MATERIALS. Annual Review of Materials Science. 2000;30:387-429.
[3] Phan M-H, Yu S-C. Review of the magnetocaloric effect in manganite materials. Journal of Magnetism and Magnetic Materials. 2007;308:325-40.
[4] Franco V, Blázquez JS, Ingale B, Conde A. The Magnetocaloric Effect and Magnetic Refrigeration Near Room Temperature: Materials and Models. Annual Review of Materials Research. 2012;42:305-42.
[5] Ucar H, Ipus JJ, McHenry ME, Laughlin DE. Overview of Amorphous and Nanocrystalline Magnetocaloric Materials Operating Near Room Temperature. Journal of Metals. 2012;64:782-8.
[6] Balli M, Jandl S, Fournier P, Gospodinov MM. Anisotropy-enhanced giant reversible rotating magnetocaloric effect in HoMn2O5 single crystals. Applied Physics Letters. 2014;104:232402.
[7] Romero Gómez J, Ferreiro Garcia R, De Miguel Catoira A, Romero Gómez M. Magnetocaloric effect: A review of the thermodynamic cycles in magnetic refrigeration. Renewable and Sustainable Energy Reviews. 2013;17:74-82.
[8] GschneidnerJr KA, Pecharsky VK, Tsokol AO. Recent developments in magnetocaloric materials %U http://stacks.iop.org/0034-4885/68/i=6/a=R04. Reports on Progress in Physics. 2005;68:1479.
[9] Qian S, Yu J, Yan G. A review of regenerative heat exchange methods for various cooling technologies. Renewable and Sustainable Energy Reviews. 2017;69:535-50.
[10] Smith A, Bahl CRH, Bjørk R, Engelbrecht K, Nielsen KK, Pryds N. Materials Challenges for High Performance Magnetocaloric Refrigeration Devices. Advanced Energy Materials. 2012;2:1288-318.
[11] Dung NH, Ou ZQ, Caron L, Zhang L, Thanh DTC, de Wijs GA, et al. Mixed Magnetism for Refrigeration and Energy Conversion. Advanced Energy Materials. 2011;1:1215-9.
[12] Chaudhary V, Ramanujan RV. Magnetocaloric Properties of Fe-Ni-Cr Nanoparticles for Active Cooling. Scientific Reports. 2016;6:35156.
[13] Moya X, Kar-Narayan S, Mathur ND. Caloric materials near ferroic phase transitions. Nat Mater. 2014;13:439-50.
[14] Balli M, Jandl S, Fournier P, Kedous-Lebouc A. Advanced materials for magnetic cooling: Fundamentals and practical aspects. Applied Physics Reviews. 2017;4:021305.
[15] de Campos A, Rocco DL, Carvalho AMG, Caron L, Coelho AA, Gama S, et al. Ambient pressure colossal magnetocaloric effect tuned by composition in Mn1-xFexAs. Nat Mater. 2006;5:802-4.
[16] Tegus O, Bruck E, Buschow KHJ, de Boer FR. Transition-metal-based magnetic refrigerants for room-temperature applications. Nature. 2002;415:150-2.
[17] Julia L. Magnetocaloric materials for energy efficient cooling. Journal of Physics D: Applied Physics. 2017;50:053002.
[18] Shull RD. Magnetocaloric effect of ferromagnetic particles. IEEE Transactions on Magnetics. 1993;29:2614 - 5
[19] Chaudhary V, Maheswar Repaka DV, Chaturvedi A, Sridhar I, Ramanujan RV. Magnetocaloric properties and critical behavior of high relative cooling power FeNiB nanoparticles. Journal of Applied Physics. 2014;116:163918-26.
[20] Zimm C, Jastrab A, Sternberg A, Pecharsky V, Gschneidner K, Osborne M, et al. Description and Performance of a Near-Room Temperature Magnetic Refrigerator. In: Kittel P, editor. Advances in Cryogenic Engineering. Boston, MA: Springer US; 1998. p. 1759-66.
[21] Chauhan A, Patel S, Vaish R, Bowen CR. A review and analysis of the elasto-caloric effect for solid-state refrigeration devices: Challenges and opportunities. MRS Energy & Sustainability. 2015;2:E16.

[22] Randalls S. History of the 2°C climate target. Wiley Interdisciplinary Reviews: Climate Change. 2010;1:598-605.
[23] Cox S. Cooling a Warming Planet:

A Global Air Conditioning Surge Yale Environment 360 2012.
[24] Chaudhary V. Study of Iron based Magnetocaloric Nanomaterials: Nanyang Technological University Singapore 2016.
[25] Velders GJM, Fahey DW, Daniel JS, McFarland M, Andersen SO. The large contribution of projected HFC emissions to future climate forcing. Proceedings of the National Academy of Sciences. 2009;106:10949-54.
[26] GmbH MKaV. Novel magnetocaloric materials for magnetic cooling applications.
[27] Ekkes B. Developments in magnetocaloric refrigeration. Journal of Physics D: Applied Physics. 2005;38:R381.
[28] www.infotech.com/download/32455.
[29] Smith A. Who discovered the magnetocaloric effect? The European Physical Journal H. 2013;38:507-17.
[30] Thomson W. II. On the thermoelastic, thermomagnetic, and pyroelectric properties of matter. The London, Edinburgh, and Dublin Philosophical Magazine and Journal of Science. 1878;5:4-27.
[31] Weiss P, Piccard A. Sur un nouveau ph´enom`ene magn´etocalorique. Comptes Rendus 1918: 352-4.
[32] Warburg E. Magnetische Untersuchungen. Annalen der Physik. 1881;249:141-64.
[33] Kuz'min MD, Tishin AM. Magnetocaloric effect. Part 1: An introduction to various aspects of theory and practice. Cryogenics. 1992;32:545-58.
[34] Tishin AM, Gschneidner KA, Pecharsky VK. Magnetocaloric effect and heat capacity in the phase-transition region. Physical Review B. 1999;59:503-11.
[35] Pecharsky VK, Gschneidner Jr KA. Magnetocaloric effect and magnetic refrigeration. Journal of Magnetism and Magnetic Materials. 1999;200:44-56.
[36] Gschneidner KA, Pecharsky VK. Magnetic refrigeration materials (invited). Journal of Applied Physics. 1999;85:5365-8.
[37] Debye P. Ann Phys. 1926;81:1154.
[38] Giauque WF. J Amer Chem Soc. 1927; 49:1864.
[39] Brown GV. Magnetic heat pumping near room temperature. Journal of Applied Physics. 1976;47:3673-80.
[40] Pecharsky VK, Gschneidner JKA. Giant Magnetocaloric Effect in ${\mathrm{Gd}}_{5}({\mathrm{Si}}_{2}{\mathrm{Ge}}_{2})$. Physical Review Letters. 1997;78:4494-7.
[41] Zimm CB, Sternberg A, Jastrab AG, Boeder AM, Lawton LM, Chell JJ. Rotating bed magnetic refrigeration apparatus. Google Patents; 2003.
[42] http://elicit-project.eu/.
[43] http://www.geglobalresearch.com/innovation/magnetocaloric-materials-chill-next-generation-refrigerators.
[44] Law JY. The magnetocaloric effect of iron-based soft magnetic alloys: Nanyang Technological University Singapore; 2012.
[45] Moreno-Ramírez LM, Ipus JJ, Franco V, Blázquez JS, Conde A. Analysis of magnetocaloric effect of ball milled amorphous alloys: Demagnetizing factor and Curie temperature distribution. Journal of Alloys and Compounds. 2015;622:606-9.
[46] Tishin AM, Spichkin, Y. I. . The Magnetocaloric Effect and its Applications: Bristol: Institute of Physics Publishing; 2003.
[47] Phan M-H, Peng H-X, Yu S-C, Duc Tho N, Chau N. Large magnetic entropy change in Cu-doped manganites. Journal of Magnetism and Magnetic Materials. 2005;285:199-203.

[48] Halder M, Yusuf SM, Mukadam MD, Shashikala K. Magnetocaloric effect and critical behavior near the paramagnetic to ferrimagnetic phase transition temperature in ${\text{TbCo}}_{2\ensuremath{-}x}{\text{Fe}}_{x}$. Physical Review B. 2010;81:174402.
[49] Chaudhary V, Chaturvedi A, Sridhar I, Ramanujan RV. Fe-Ni-Mn Nanoparticles for Near Room Temperature Magnetic Cooling. IEEE Magn Lett. 2014;5:6800104-8.
[50] Chaudhary V, Chen X, Repaka DVM, Chaturvedi A, Wang Z, Ramanujan RV. High Relative Cooling Power Iron based Magnetocaloric Nanoparticles. 6th IIF-IIR International Conference on Magnetic Refrigeration THERMAG VI, Victoria, BC, 7-10 Sept 2014. 2014.
[51] Chaudhary V, Ramanujan RV. Iron Oxide-based Magnetic Nanoparticles for High Temperature Span Magnetocaloric Applications. MRS Online Proceedings Library. 2014;1708:vv10-08.
[52] Chaudhary V, Ramanujan RV. Magnetic and structural properties of high relative cooling power (Fe 70 Ni 30) 92 Mn 8 magnetocaloric nanoparticles. Journal of Physics D: Applied Physics. 2015;48:305003.
[53] Chaudhary V, Ramanujan RV. High Relative Cooling Power in a Multiphase Magnetocaloric FeNiB Alloy. Magnetics Letters, IEEE. 2015;6:6700104(4).
[54] Engelbrecht K, Bahl CRH. Evaluating the effect of magnetocaloric properties on magnetic refrigeration performance. Journal of Applied Physics. 2010;108:123918.
[55] Jaka Tušek UT, Andrej Kitanovski, Uroš Plaznik, Marko Ožbolt and Alojz Poredoš. Magnetocaloric Energy Conversion: Springer International Publishing Switzerland; 2015.
[56] Chaudhary V, Chaturvedi A, Ramanujan RV. Magnetocaloric behavior of Fe-Ni-Mn nanoparticies. Magnetics Symposium 2014 - Celebrating 50th Anniversary of IEEE Magnetics Society (MSSC50)2014. p. 1-2.
[57] Chen X, Maheswar Repaka DV, Ramanujan RV. Structural investigation of the crossover in the magnetic transition of Mn–Fe–P–Ge magnetocaloric powders. Journal of Alloys and Compounds. 2016;658:104-9.
[58] Chen X, Naik VB, Mahendiran R, Ramanujan RV. Optimization of Ni–Co–Mn–Sn Heusler alloy composition for near room temperature magnetic cooling. Journal of Alloys and Compounds. 2015;618:187-91.
[59] Chen X, Ramanujan RV. The magnetic phase transition in Mn1.1Fe0.9P1−xGex magnetocaloric alloys. Journal of Applied Physics. 2015;117:063909.
[60] Zhang CL, Shi HF, Ye EJ, Nie YG, Han ZD, Qian B, et al. Magnetostructural transition and magnetocaloric effect in MnNiSi-Fe2Ge system. Applied Physics Letters. 2015;107:212403.
[61] Moore JD, Perkins GK, Bugoslavsky Y, Chattopadhyay MK, Roy SB, Chaddah P, et al. Reducing the operational magnetic field in the prototype magnetocaloric system Gd5Ge4 by approaching the single cluster size limit. Applied Physics Letters. 2006;88:072501.
[62] Aprea C, Greco A, Maiorino A. Magnetic refrigeration: a promising new technology for energy saving. International Journal of Ambient Energy. 2016;37:294-313.
[63] Pires AL, Belo JH, Turcaud J, Oliveira GNP, Araújo JP, Berenov A, et al. Influence of short time milling in R5(Si,Ge)4, R = Gd and Tb, magnetocaloric materials. Materials & Design. 2015;85:32-8.
[64] Thanh TD, Nan WZ, Nam G, Van HT, You TS, Phan TL, et al. Conventional and inverse magnetocaloric effects, and critical behaviors in Ni43Mn46Sn8In3 alloy. Current Applied Physics. 2015;15:1200-4.
[65] Durga P, Pecharsky VK, K. A. Gschneidner J. Origins of ferromagnetism and antiferromagnetism in Gd 5 Ge 4. Journal of Physics: Condensed Matter. 2008;20:235235.
[66] Chen C-W. Magnetism and Metallurgy of Soft Magnetic materials North Holland Publishing Company; 1977.
[67] Binary Alloy Phase Diagrams, 2nd Edition: ASM International Materials Park, OH 1990.
[68] Miller KJ, Sofman M, McNerny K, McHenry ME. Metastable γ-FeNi nanostructures with tunable Curie temperature. Journal of Applied Physics. 2010;107:09A305.
[69] Chaudhary V, Chaturvedi A, Sridhar I, Ramanujan RV. Fe-Ni-Mn nanoparticles for magnetic cooling near room temperature. IEEE Magnetics Letters. 2014;5.

[70] Caballero-Flores R, Franco V, Conde A, Knipling KE, Willard MA. Optimization of the refrigerant capacity in multiphase magnetocaloric materials. Applied Physics Letters. 2011;98:-.
[71] Dolocan V, Dolocan E. Curie temperatrue measurements in amorphous Fe-Co-B alloys. J Phys III France. 1992;2:915-20.
[72] Kazama NS, Masumoto T, Mitera M. Effects of metalloids on the magnetic properties of iron- and cobalt-based amorphous alloys. Journal of Magnetism and Magnetic Materials. 1980;15–18, Part 3:1331-5.
[73] Hasegawa R, Ray R. Iron-boron metallic glasses. Journal of Applied Physics. 1978;49:4174-9.
[74] Gallas MR, Jornada JAHd. Effects of annealing processes on the Curie temperature of Fe-Ni Invar alloys. Journal of Physics: Condensed Matter. 1991;3:155.
[75] Mandal S, Panda J, Nath TK. Investigation of the critical behaviour and magnetocaloric effect in γ-Fe49Ni29Cr22 disordered austenitic stainless steel alloy by using the field dependence of magnetic entropy change. Journal of Alloys and Compounds. 2015;653:453-9.
[76] Ucar H, Craven M, Laughlin DE, McHenry ME. Effect of Mo Addition on Structure and Magnetocaloric Effect in γ-FeNi Nanocrystals. Journal of Electronic Materials. 2014;43:137-41.
[77] Thanveer T, Ramanujan RV, Thomas S. Magnetocaloric effect in amorphous and partially crystallized Fe40Ni38Mo4B18 alloys. AIP Advances. 2016;6:055322.
[78] Ucar H, Ipus JJ, Laughlin DE, McHenry ME. Tuning the Curie temperature in gamma-FeNi nanoparticles for magnetocaloric applications by controlling the oxidation kinetics. Journal of Applied Physics. 2013;113:17A918-21.
[79] Ipus JJ, Ucar H, McHenry ME. Near Room Temperature Magnetocaloric Response of an (FeNi)ZrB Alloy. IEEE Transactions on Magnetics. 2011;47:2494-7.
[80] Pedro G, José LSL, Pablo Á, María José P, Jorge Sánchez M, Jesús AB. Relative cooling power enhancement in magneto-caloric nanostructured Pr 2 Fe 17. Journal of Physics D: Applied Physics. 2008;41:192003.
[81] Pablo Á, Pedro G, Victorino F, Jorge Sánchez M, María JP, José LSL, et al. Nanocrystalline Nd 2 Fe 17 synthesized by high-energy ball milling: crystal structure, microstructure and magnetic properties. Journal of Physics: Condensed Matter. 2010;22:216005.
[82] Alvarez-Alonso P, Sánchez Llamazares JL, Sánchez-Valdés CF, Cuello GJ, Franco V, Gorria P, et al. On the broadening of the magnetic entropy change due to Curie temperature distribution. Journal of Applied Physics. 2014;115:17A929-32.
[83] Álvarez-Alonso P, Gorria P, Blanco JA, Sánchez-Marcos J, Cuello GJ, Puente-Orench I, et al. Magnetovolume and magnetocaloric effects in Er${}_{2}$Fe${}_{17}$. Physical Review B. 2012;86:184411.
[84] Pablo Á-A, Pedro G, Jorge Sánchez M, José LSL, Jesús AB. The magnetocaloric effect in Er 2 Fe 17 near the magnetic phase transition. Journal of Physics: Condensed Matter. 2013;25:496010.
[85] Sánchez-Valdés CF, Ibarra-Gaytán PJ, Llamazares JLS, Ávalos-Borja M, Álvarez-Alonso P, Gorria P, et al. Enhanced refrigerant capacity in two-phase nanocrystalline/amorphous NdPrFe17 melt-spun ribbons. Applied Physics Letters. 2014;104:212401.
[86] Waske A, Hermann H, Mattern N, Skokov K, Gutfleisch O, Eckert J. Magnetocaloric effect of an Fe-based metallic glass compared to benchmark gadolinium. Journal of Applied Physics. 2012;112:123918.
[87] Fang YK, Chang CW, Yeh CC, Chang HW, Li W, Chang WC. Microstructure and magnetocaloric effect of melt-spun Y2Fe17 ribbons. Journal of Applied Physics. 2008;103:07B302.
[88] Sánchez Llamazares JL, Álvarez-Alonso P, Sánchez-Valdés CF, Ibarra-Gaytán PJ, Blanco JA, Gorria P. Investigating the magnetic entropy change in single-phase Y2Fe17 melt-spun ribbons. Current Applied Physics. 2016;16:963-8.
[89] Law JY, Franco V, Ramanujan RV. Influence of La and Ce additions on the magnetocaloric effect of Fe-B-Cr-based amorphous alloys. Applied Physics Letters. 2011;98:192503-6.
[90] Law JY, Franco V, Ramanujan RV. The magnetocaloric effect of partially crystalline Fe-B-Cr-Gd alloys. Journal of Applied Physics. 2012;111: 3919- 25.

[91] Law JY, Franco V, Ramanujan RV. Direct magnetocaloric measurements of Fe-B-Cr-X (X = La, Ce) amorphous ribbons. Journal of Applied Physics. 2011;110:023907.
[92] Law JY, Ramanujan RV, Franco V. Tunable Curie temperatures in Gd alloyed Fe–B–Cr magnetocaloric materials. Journal of Alloys and Compounds. 2010;508:14-9.
[93] Lai JW, Zheng ZG, Zhong XC, Franco V, Montemayor R, Liu ZW, et al. Table-like magnetocaloric effect of Fe88−xNdxCr8B4 composite materials. Journal of Magnetism and Magnetic Materials. 2015;390:87-90.
[94] Mishra D, Gurram M, Reddy A, Perumal A, Saravanan P, Srinivasan A. Enhanced soft magnetic properties and magnetocaloric effect in B substituted amorphous Fe–Zr alloy ribbons. Materials Science and Engineering: B. 2010;175:253-60.
[95] Álvarez P, Gorria P, Sánchez Marcos J, Fernández Barquín L, Blanco JA. The role of boron on the magneto-caloric effect of FeZrB metallic glasses. Intermetallics. 2010;18:2464-7.
[96] Wang Y, Bi X. The role of Zr and B in room temperature magnetic entropy change of FeZrB amorphous alloys. Applied Physics Letters. 2009;95:262501.
[97] Franco V, Conde CF, Blázquez JS, Conde A, Švec P, Janičkovič D, et al. A constant magnetocaloric response in FeMoCuB amorphous alloys with different Fe⁄B ratios. Journal of Applied Physics. 2007;101:093903.
[98] Yu P, Zhang JZ, Xia L. Effect of boron on the magneto-caloric effect in Fe91−x Zr9B x (x = 3, 4, 5) amorphous alloys. Journal of Materials Science. 2017;52:13948-55.
[99] Guo DQ, Chan KC, Xia L, Yu P. Magneto-caloric effect of FexZryB100−x−y metallic ribbons for room temperature magnetic refrigeration. Journal of Magnetism and Magnetic Materials. 2017;423:379-85.
[100] Guo DQ, Yuan YD, Chan KC. The Effect of Different Minor Additions on the Magneto-caloric Effect of FeZrB Metallic Ribbons near Room Temperature. Journal of Magnetism and Magnetic Materials. 2017.
[101] Gan L, Ma L, Tang B, Ding D, Xia L. Effect of Co substitution on the glass forming ability and magnetocaloric effect of Fe88Zr8B4 amorphous alloys. Science China Physics, Mechanics & Astronomy. 2017;60:076121.
[102] Fang YK, Yeh CC, Hsieh CC, Chang CW, Chang HW, Chang WC, et al. Magnetocaloric effect in Fe–Zr–B–M (M=Mn, Cr, and Co) amorphous systems. Journal of Applied Physics. 2009;105:07A910.
[103] Li X, Pan Y. Magnetocaloric effect in Fe-Zr-B-M (M = Ni, Co, Al, and Ti) amorphous alloys. Journal of Applied Physics. 2014;116:093910.
[104] Johnson F, Shull RD. Amorphous-FeCoCrZrB ferromagnets for use as high-temperature magnetic refrigerants. Journal of Applied Physics. 2006;99:08K909.
[105] Franco V, Blázquez JS, Conde A. The influence of Co addition on the magnetocaloric effect of Nanoperm-type amorphous alloys. Journal of Applied Physics. 2006;100:064307.
[106] Knipling KE, Daniil M, Willard MA. Nanocrystalline Fe88−2xCoxNixZr7B4Cu1 alloys: Soft magnets for vehicle electrification technologies (invited). Journal of Applied Physics. 2015;117:172611.
[107] Caballero-Flores R, Franco V, Conde A, Knipling KE, Willard MA. Influence of Co and Ni addition on the magnetocaloric effect in Fe88−2xCoxNixZr7B4Cu1 soft magnetic amorphous alloys. Applied Physics Letters. 2010;96:182506.
[108] Caballero-Flores R, Franco V, Conde A, Kiss LF. Influence of Mn on the magnetocaloric effect of nanoperm-type alloys. Journal of Applied Physics. 2010;108:073921.
[109] Škorvánek I, Kováč J. Magnetocaloric Behaviour in Amorphous and Nanocrystalline FeNbB Soft Magnetic Alloys. Czechoslovak Journal of Physics. 2004;54:189-92.
[110] Franco V, Conde A, Kiss LF. Magnetocaloric response of FeCrB amorphous alloys: Predicting the magnetic entropy change from the Arrott–Noakes equation of state. Journal of Applied Physics. 2008;104:033903.

[111] Škorvánek I, Kováč J, Marcin J, Švec P, Janičkovič D. Magnetocaloric effect in amorphous and nanocrystalline Fe81−xCrxNb7B12 (x = 0 and 3.5) alloys. Materials Science and Engineering: A. 2007;449–451:460-3.
[112] Torrens-Serra J, Bruna P, Roth S, Rodriguez-Viejo J, Clavaguera-Mora MT. Structural and magnetic characterization of FeNbBCu alloys as a function of Nb content. Journal of Physics D: Applied Physics. 2009;42:095010.
[113] Zhu-bai L, Le-le Z, Xue-feng Z, Yong-feng L, Qian Z, Tong-yun Z, et al. Tunable Curie temperature around room temperature and magnetocaloric effect in ternary Ce–Fe–B amorphous ribbons. Journal of Physics D: Applied Physics. 2017;50:015002.
[114] Min SG, Kim KS, Yu SC, Suh HS, Lee SW. Analysis of magnetization and magnetocaloric effect in amorphous FeZrMn ribbons. Journal of Applied Physics. 2005;97:10M310.
[115] Min SG, Kim KS, Yu SC, Kim YC, Kim KY, Lee KW, et al. The magnetic entropy change on amorphous FeMnZr alloys. Journal of Magnetism and Magnetic Materials. 2007;310:2820-2.
[116] Dan NH, Yen NH, Thanh PT. Magnetocaloric Effect and Critical Behavior in Fe-Dy-Zr Rapidly Quenched Alloys. Journal of Electronic Materials. 2016;45:5058-63.
[117] Rodríguez DM, Plazaola F, Garitaonandia JS, Jiménez JA, Apiñaniz E. Influence of volume and Fe local environment on magnetic properties of Fe-rich Fe–Al alloys. Intermetallics. 2012;24:38-49.
[118] Huang YD, Yang WY, Sun ZQ. Improvement of room temperature tensile properties for Fe3Al-based alloys by thermomechanical and annealing processes. Materials Science and Engineering: A. 1999;263:75-84.
[119] Sharma V, Repaka DVM, Chaudhary V, Ramanujan RV. Enhanced magnetocaloric properties and critical behavior of (Fe 0.72 Cr 0.28) 3 Al alloys for near room temperature cooling. Journal of Physics D: Applied Physics. 2017;50:145001.
[120] Wang Y, Bi X. Effect of noncollinear spin structure on magnetic entropy change and its field dependence in Fe90Sc10 amorphous alloy. Applied Physics Letters. 2010;97:022503.
[121] Wang Y, Hou K, Bi X. Hydrogenated Fe90M10 (M: Zr and Sc) amorphous alloys with enhanced room-temperature magnetocaloric effect. Journal of Alloys and Compounds. 2016;689:564-9.
[122] Moubah R, Boutahar A, Lassri H, Dinia A, Colis S, Hjörvarsson B, et al. Enhanced magnetocaloric properties of FeZr amorphous films by C ion implantation. Materials Letters. 2016;175:5-8.
[123] Repaka DVM, Sharma V, Ramanujan RV. Near room temperature magnetocaloric properties and critical behavior of binary FexCu100−xNanoparticles. Journal of Alloys and Compounds. 2017;690:575-82.
[124] Desautels RD, Shueh C, Lin K-W, Freeland JW, van Lierop J. Dynamical freezing, magnetic ordering, and the magnetocaloric effect in nanostructured Fe/Cu thin films. Applied Physics Letters. 2016;108:172410.
[125] Li J, Law JY, Ma H, He A, Man Q, Men H, et al. Magnetocaloric effect in Fe-Tm-B-Nb metallic glasses near room temperature. Journal of Non-Crystalline Solids. 2015;425:114-7.
[126] Tian HC, Zhong XC, Liu ZW, Zheng ZG, Min JX. Achieving table-like magnetocaloric effect and large refrigerant capacity around room temperature in Fe78−xCexSi4Nb5B12Cu1 (x=0–10) composite materials. Materials Letters. 2015;138:64-6.
[127] Shishkin DA, Volegov AS, Baranov NV. The thermomechanical stability of Fe-based amorphous ribbons exhibiting magnetocaloric effect. Applied Physics A. 2016;122:1002.
[128] Zhang H, Li R, Xu T, Liu F, Zhang T. Near room-temperature magnetocaloric effect in FeMnPBC metallic glasses with tunable Curie temperature. Journal of Magnetism and Magnetic Materials. 2013;347:131-5.
[129] Wang D, Peng K, Gu B, Han Z, Tang S, Qin W, et al. Influence of annealing on the magnetic entropy changes in Fe81.6Mo4Zr3.3Nb3.3B6.8Cu1 amorphous ribbons. Journal of Alloys and Compounds. 2003;358:312-5.

[130] Franco V, Borrego JM, Conde CF, Conde A, Stoica M, Roth S. Refrigerant capacity of FeCrMoCuGaPCB amorphous alloys. Journal of Applied Physics. 2006;100:083903.
[131] Shen TD, Schwarz RB, Coulter JY, Thompson JD. Magnetocaloric effect in bulk amorphous Pd40Ni22.5Fe17.5P20 alloy. Journal of Applied Physics. 2002;91:5240-5.
[132] Lee JH, Lee SJ, Han WB, An HH, Yoon CS. Magnetocaloric effect of Fe64Mn15−xCoxSi10B11 amorphous alloys. Journal of Alloys and Compounds. 2011;509:7764-7.
[133] Boutahar A, Ettayfi A, Alouhmy G, Lassri H, Hlil EK, Fruchart D. The Influence of Vanadium on Magnetism and Magnetocaloric Properties of Fe80−xVxB12Si8 (x = 8, 10, and 13.7) Amorphous Alloys. Journal of Superconductivity and Novel Magnetism. 2014;27:2401-5.
[134] Moreno-Ramirez LM, Blazquez JS, Franco V, Conde A, Marsilius M, Budinsky V, et al. Magnetocaloric response of amorphous and nanocrystalline Cr-containing Vitroperm-type alloys. Journal of Magnetism and Magnetic Materials. 2016;409:56-61.
[135] Wang GF, Li HL, Zhao ZR, Zhang XF. Stable magnetocaloric effect and refrigeration capacity in Co-doped FeCoMnZrNbB amorphous ribbons near room temperature. Journal of Alloys and Compounds. 2017;692:793-6.
[136] Franco V, Borrego JM, Conde A, Roth S. Influence of Co addition on the magnetocaloric effect of FeCoSiAlGaPCB amorphous alloys. Applied Physics Letters. 2006;88:132509.
[137] Franco V, Conde C, Conde A, Kiss L. Enhanced magnetocaloric response in Cr⁄ Mo containing Nanoperm-type amorphous alloys. Applied physics letters. 2007;90:052509.
[138] Lucas MS, Belyea D, Bauer C, Bryant N, Michel E, Turgut Z, et al. Thermomagnetic analysis of FeCoCrxNi alloys: Magnetic entropy of high-entropy alloys. Journal of Applied Physics. 2013;113:17A923.
[139] Belyea DD, Lucas MS, Michel E, Horwath J, Miller CW. Tunable magnetocaloric effect in transition metal alloys. Scientific Reports. 2015;5:15755.
[140] Körmann F, Ma D, Belyea DD, Lucas MS, Miller CW, Grabowski B, et al. “Treasure maps” for magnetic high-entropy-alloys from theory and experiment. Applied Physics Letters. 2015;107:142404.
[141] Perrin A, Sorescu M, Burton M-T, Laughlin DE, McHenry M. The Role of Compositional Tuning of the Distributed Exchange on Magnetocaloric Properties of High-Entropy Alloys. JOM. 2017;69:2125-9.
[142] Kurniawan M, Perrin A, Xu P, Keylin V, McHenry M. Curie Temperature Engineering in High Entropy Alloys for Magnetocaloric Applications. IEEE Magnetics Letters. 2016;7:1-5.
[143] Barclay JA. Use of a ferrofluid as the heat-exchange fluid in a magnetic refrigerator. Journal of Applied Physics. 1982;53:2887-94.
[144] Rosenweig RE. Ferrohydrodynamics Cambridge University Press; 1985.
[145] Love L, Jansen J, McKnight T. Magnetocaloric pump for microfluidic applications. Google Patents; 2006.
[146] Love LJ, Jansen JF, McKnight TE, Roh Y, Phelps TJ. A magnetocaloric pump for microfluidic applications. NanoBioscience, IEEE Transactions on. 2004;3:101-10.
[147] Chaudhary V, Ramanujan RV. Self pumping magnetic cooling Journal of Physics D: Applied Physics. 2016.
[148] Garanin DA, Kachkachi H. Surface Contribution to the Anisotropy of Magnetic Nanoparticles. Physical Review Letters. 2003;90:065504.
[149] Jones NJ, Ucar H, Ipus JJ, McHenry ME, Laughlin DE. The effect of distributed exchange parameters on magnetocaloric refrigeration capacity in amorphous and nanocomposite materials. Journal of Applied Physics. 2012;111:07A334-7.
[150] Gass SHaJ. Superparamagnetism and Magneto-caloric Effect (MCE) in Functional Magnetic Nanostructures REVIEWS ON ADVANCED MATERIALS SCIENCE. 2005;10:398-402.
[151] Burianova S, Poltierova-Vejpravova J, Holec P, Plocek J. Magnetocaloric phenomena in Mg-ferrite nanoparticles. Journal of Physics: Conference Series. 2010;200.

[152] Poddar P, Gass J, Rebar DJ, Srinath S, Srikanth H, Morrison SA, et al. Magnetocaloric effect in ferrite nanoparticles. Journal of Magnetism and Magnetic Materials. 2006;307:227-31.
[153] Prabhakaran T, Mangalaraja RV, Denardin JC. The structural, magnetic and magnetic entropy changes on CoFe2O4/CoFe2 composites for magnetic refrigeration application. Journal of Magnetism and Magnetic Materials. 2017;444:297-306.
[154] Phan TL, Tran N, Kim DH, Dang NT, Manh DH, Bach TN, et al. Magnetic and Magnetocaloric Properties of Zn1−x Co x Fe2O4 Nanoparticles. Journal of Electronic Materials. 2017;46:4214-26.
[155] Ramanujan RV. Self-pumping Magnetic Cooling Singapore 2016.
[156] Chaudhary V, Wang Z, Ray A, Sridhar I, Ramanujan RV. Self pumping magnetic cooling. Journal of Physics D: Applied Physics. 2017;50:03LT.
[157] Ganguly R, Sen S, Puri IK. Thermomagnetic convection in a square enclosure using a line dipole. Physics of Fluids. 2004;16:2228-36.
[158] Mukhopadhyay A, Ganguly R, Sen S, Puri IK. A scaling analysis to characterize thermomagnetic convection. International Journal of Heat and Mass Transfer. 2005;48:3485-92.
[159] Lian W, Xuan Y, Li Q. Design method of automatic energy transport devices based on the thermomagnetic effect of magnetic fluids. International Journal of Heat and Mass Transfer. 2009;52:5451-8.
[160] Lian W, Xuan Y, Li Q. Characterization of miniature automatic energy transport devices based on the thermomagnetic effect. Energy Conversion and Management. 2009;50:35-42.
[161] Xuan Y, Lian W. Electronic cooling using an automatic energy transport device based on thermomagnetic effect. Applied Thermal Engineering. 2011;31:1487-94.
[162] Pal S, Datta A, Sen S, Mukhopdhyay A, Bandopadhyay K, Ganguly R. Characterization of a ferrofluid-based thermomagnetic pump for microfluidic applications. Journal of Magnetism and Magnetic Materials. 2011;323:2701-9.
[163] Rahman H, Suslov SA. Thermomagnetic convection in a layer of ferrofluid placed in a uniform oblique external magnetic field. Journal of Fluid Mechanics. 2015;764:316-48.
[164] Skokov KP, Gutfleisch O. Viewpoint on the letter 'Self pumping magnetic cooling' by V Chaudhary et al (2017 J. Phys. D: Appl. Phys . 50 03LT03). J Phys D: Appl Phys. 2017;50:131001.
[165] Atalay S, Gencer H, Kolat VS. Magnetic entropy change in Fe74−xCrxCu1Nb3Si13B9 (x = 14 and 17) amorphous alloys. Journal of Non-Crystalline Solids. 2005;351:2373-7.
[166] Moreno-Ramírez LM, Blázquez JS, Franco V, Conde A, Marsilius M, Budinsky V, et al. Magnetocaloric response of amorphous and nanocrystalline Cr-containing Vitroperm-type alloys. Journal of Magnetism and Magnetic Materials. 2016;409:56-61.
[167] Gopalan EV, Al-Omari IA, Kumar DS, Yoshida Y, Joy PA, Anantharaman MR. Inverse magnetocaloric effect in sol–gel derived nanosized cobalt ferrite. Applied Physics A. 2010;99:497-503.
[168] Chau N, Thuan NK, Minh DL, Luong NH. Effects of Zn content on the magnetic and magnetocaloric properties of Ni-Zn ferrites. VNU J Sci Mathematics – Phys. 2008;24:155-62.
[169] Maalam KE, Fkhar L, Hamedoun M, Mahmoud A, Boschini F, Hlil EK, et al. Magnetocaloric Properties of Zinc-Nickel Ferrites Around Room Temperature. Journal of Superconductivity and Novel Magnetism. 2017;30:1943-7.
[170] Hu F-x, Shen B-g, Sun J-r, Cheng Z-h, Rao G-h, Zhang X-x. Influence of negative lattice expansion and metamagnetic transition on magnetic entropy change in the compound LaFe11.4Si1.6. Applied Physics Letters. 2001;78:3675-7.
[171] Álvarez-Alonso P, Aguilar-Ortiz CO, Camarillo JP, Salazar D, Flores-Zúñiga H, Chernenko VA. Adiabatic magnetocaloric effect in Ni50Mn35In15 ribbons. Applied Physics Letters. 2016;109:212402.
[172] Reesink BH, Brueck E, Nguyen HD, Zhang L. Magnetocaloric materials. Google Patents; 2016.
[173] Cugini F, Porcari G, Viappiani C, Caron L, Santos AOd, Cardoso LP, et al. Millisecond direct measurement of the magnetocaloric effect of a Fe2P-based compound by the mirage effect. Applied Physics Letters. 2016;108:012407.

[174] Kim K-H, Son W-J, Kwon S-J, Kim I-G, Yang D-S, Ham Y-N. Structural study of the magnetocaloric material MnFePxAs1−x. Electronic Materials Letters. 2016;12:255-9.
[175] Morrison K, Lyubina J, Moore JD, Sandeman KG, Gutfleisch O, Cohen LF, et al. Magnetic refrigeration: phase transitions, itinerant magnetism and spin fluctuations. Philosophical Magazine. 2012;92:292-303.
[176] Paticopoulos SC, Caballero-Flores R, Franco V, Blázquez JS, Conde A, Knipling KE, et al. Enhancement of the magnetocaloric effect in composites: Experimental validation. Solid State Communications. 2012;152:1590-4.
[177] Xu H, Yue M, Zhao C, Zhang D, Zhang J. Structure and magnetic properties of Mn1.2Fe0.8P0.76Ge0.24 annealed alloy. Rare Metals. 2012;31:336-8.
[178] Yamada H, Terao K. First-Order Transition of Fe 2 P and Anti-Metamagnetic Transition. Phase Transitions. 2002;75:231-42.
[179] Carroll C, Rogge O, Reesink B. Magneto-caloric heat pump with the use of a cascade of magneto-caloric materials. Google Patents; 2011.
[180] Ou ZQ, Dung NH, Zhang L, Caron L, Torun E, van Dijk NH, et al. Transition metal substitution in Fe2P-based MnFe0.95P0.50Si0.50 magnetocaloric compounds. Journal of Alloys and Compounds. 2018;730:392-8.
[181] Zheng ZG, Zhu ZR, Yu HY, Zeng DC, Li YH, He A, et al. Large magnetic entropy change and magnetic phase transitions in rapidly quenched bulk Mn-Fe-P-Si alloys. Journal of Alloys and Compounds. 2017;725:1069-76.
[182] Hudl M. Magnetic materials with tunable thermal, electrical, and dynamic properties. : Uppsala University.; 2012.
[183] Nascimento FC, Santos AOd, Campos Ad, Gama S, Cardoso LP. Structural and magnetic study of the MnAs magnetocaloric compound. Materials Research. 2006;9:111-4.
[184] Mitsiuk VI, Govor GA, Budzyński M. Phase transitions and magnetocaloric effect in MnAs, MnAs0.99P0.01, and MnAs0.98P0.02 single crystals. Inorganic Materials. 2013;49:14-7.
[185] Wada H, Funaba C, Asano T. Effects of Heat Treatment on the Magnetic Phase Transition and Magnetocaloric Properties of Mn_{1+δ}As_{1−<I>x</I>}Sb<I>_x</I>. MATERIALS TRANSACTIONS. 2006;47:486-91.
[186] Wada H, Tanabe Y. Giant magnetocaloric effect of MnAs1−xSbx. Applied Physics Letters. 2001;79:3302-4.
[187] Yue M, Li ZQ, Wang XL, Liu DM, Zhang JX, Liu XB. Crystal structure and magnetic transition of MnFePGe compound prepared by spark plasma sintering. Journal of Applied Physics. 2009;105:07A915.
[188] Liu LJ, Liu DM, Huang QZ, Zhang TL, Zhang L, Yue M, et al. Neutron diffraction study of the magnetic refrigerant Mn1.1Fe0.9P0.76Ge0.24. Powder Diffraction. 2010;25:S25-S7.
[189] Trung NT, Klaasse JCP, Tegus O, Thanh DTC, Buschow KHJ, Brück E. Determination of adiabatic temperature change in MnFe(P,Ge) compounds with pulse-field method. Journal of Physics D: Applied Physics. 2010;43:015002.
[190] Liu DM, Zhang ZL, Zhou SL, Huang QZ, Deng XJ, Yue M, et al. A pathway to optimize the properties of magnetocaloric Mn2-xFexP1-yGey for magnetic refrigeration. Journal of Alloys and Compounds. 2016;666:108-17.
[191] Delczeg-Czirjak EK, Gercsi Z, Bergqvist L, Eriksson O, Szunyogh L, Nordblad P, et al. Magnetic exchange interactions in B-, Si-, and As-doped Fe${}_{2}$P from first-principles theory. Physical Review B. 2012;85:224435.
[192] Yibole H, Guillou F, Zhang L, Dijk NHv, Brück E. Direct measurement of the magnetocaloric effect in MnFe(P, X)(X = As, Ge, Si) materials. Journal of Physics D: Applied Physics. 2014;47:075002.

[193] Miao XF, Caron L, Gubbens PCM, Yaouanc A, Dalmas de Réotier P, Luetkens H, et al. Spin correlations in (Mn,Fe)2(P,Si) magnetocaloric compounds above Curie temperature. Journal of Science: Advanced Materials and Devices. 2016;1:147-51.
[194] Thang NV, Miao XF, van Dijk NH, Brück E. Structural and magnetocaloric properties of (Mn,Fe)2(P,Si) materials with added nitrogen. Journal of Alloys and Compounds. 2016;670:123-7.
[195] Miao XF, Thang NV, Caron L, Yibole H, Smith RI, van Dijk NH, et al. Tuning the magnetoelastic transition in (Mn,Fe)2(P,Si) by B, C, and N doping. Scripta Materialia. 2016;124:129-32.
[196] Miao XF, Mitsui Y, Dugulan AI, Caron L, Thang NV, Manuel P, et al. Kinetic-arrest-induced phase coexistence and metastability in ${(\mathrm{Mn},\mathrm{Fe})}_{2}(\mathrm{P},\mathrm{Si})$. Physical Review B. 2016;94:094426.
[197] Boeije MFJ, Roy P, Guillou F, Yibole H, Miao XF, Caron L, et al. Efficient Room-Temperature Cooling with Magnets. Chemistry of Materials. 2016;28:4901-5.
[198] Thang NV, Yibole H, Miao XF, Goubitz K, van Eijck L, van Dijk NH, et al. Effect of Carbon Doping on the Structure and Magnetic Phase Transition in (Mn,Fe2(P,Si)). JOM. 2017;69:1432-8.
[199] Thang N, Dijk N, Brück E. Tuneable Giant Magnetocaloric Effect in (Mn,Fe)2(P,Si) Materials by Co-B and Ni-B Co-Doping. Materials. 2017;10:14.
[200] Guillou F, Yibole H, Porcari G, Zhang L, Dijk NHv, Brück E. Magnetocaloric effect, cyclability and coefficient of refrigerant performance in the MnFe(P, Si, B) system. Journal of Applied Physics. 2014;116:063903.
[201] Skokov KP, Müller KH, Moore JD, Liu J, Karpenkov AY, Krautz M, et al. Influence of thermal hysteresis and field cycling on the magnetocaloric effect in LaFe11.6Si1.4. Journal of Alloys and Compounds. 2013;552:310-7.
[202] Guillou F, Porcari G, Yibole H, van Dijk N, Brück E. Taming the First-Order Transition in Giant Magnetocaloric Materials. Advanced Materials. 2014;26:2671-5.
[203] Chen X, Ramanujan RV. Large magnetocaloric effect near room temperature in Mn–Fe–P–Ge nanostructured powders. Journal of Alloys and Compounds. 2015;652:393-9.
[204] Trung NT, Ou ZQ, Gortenmulder TJ, Tegus O, Buschow KHJ, Brück E. Tunable thermal hysteresis in MnFe(P,Ge) compounds. Applied Physics Letters. 2009;94:102513.
[205] Yue M, Li ZQ, Liu XB, Xu H, Liu DM, Zhang JX. Magnetocaloric effect and magnetic transition in bulk Mn1.1Fe0.9P0.8Ge0.2 compound. Journal of Alloys and Compounds. 2010;493:22-5.
[206] Yan A, Müller K-H, Schultz L, Gutfleisch O. Magnetic entropy change in melt-spun MnFePGe (invited). Journal of Applied Physics. 2006;99:08K903.
[207] Yao-Xiang G, O T, Li-Ge B. Magnetocaloric effects in Mn 1.35 Fe 0.65 P 1− x Si x compounds. Chinese Physics B. 2012;21:037504.
[208] Brück E, Tegus O, Cam Thanh DT, Trung NT, Buschow KHJ. A review on Mn based materials for magnetic refrigeration: Structure and properties. International Journal of Refrigeration. 2008;31:763-70.
[209] Liu XB, Ping Liu J, Zhang Q, Altounian Z. Fe magnetic moment formation and exchange interaction in Fe2P: A first-principles study. Physics Letters A. 2013;377:731-5.
[210] Gallagher KA, Willard MA, Zabenkin VN, Laughlin DE, McHenry ME. Distributed exchange interactions and temperature dependent magnetization in amorphous Fe88−xCoxZr7B4Cu1 alloys. Journal of Applied Physics. 1999;85:5130-2.
[211] Bratko M, Morrison K, de Campos A, Gama S, Cohen LF, Sandeman KG. History dependence of directly observed magnetocaloric effects in (Mn, Fe)As. Applied Physics Letters. 2012;100:252409.
[212] Chen X. The Magnetocaloric Effect in Fe2P based alloys: Nanyang Technological University Singapore 2016.

[213] Thang NV, Yibole H, van Dijk NH, Brück E. Effect of heat treatment conditions on MnFe(P,Si,B) compounds for room-temperature magnetic refrigeration. Journal of Alloys and Compounds. 2017;699:633-7.
[214] Engelbrecht K, Nielsen KK, Bahl CRH, Carroll CP, Asten Dv. Material properties and modeling characteristics for MnFeP1−xAsx materials for application in magnetic refrigeration. Journal of Applied Physics. 2013;113:173510.
[215] Gutfleisch O, Gottschall T, Fries M, Benke D, Radulov I, Skokov KP, et al. Mastering hysteresis in magnetocaloric materials. Philosophical Transactions of the Royal Society A: Mathematical, Physical and Engineering Sciences. 2016;374.
[216] Ajaya KN, Suresh KG, Nigam AK. Giant inverse magnetocaloric effect near room temperature in Co substituted NiMnSb Heusler alloys. Journal of Physics D: Applied Physics. 2009;42:035009.
[217] Fähler S, Rößler UK, Kastner O, Eckert J, Eggeler G, Emmerich H, et al. Caloric Effects in Ferroic Materials: New Concepts for Cooling. Advanced Engineering Materials. 2012;14:10-9.
[218] Srivastava V, Chen X, James RD. Hysteresis and unusual magnetic properties in the singular Heusler alloy Ni45Co5Mn40Sn10. Applied Physics Letters. 2010;97:014101.
[219] Liu J, Gottschall T, Skokov KP, Moore JD, Gutfleisch O. Giant magnetocaloric effect driven by structural transitions. Nat Mater. 2012;11:620-6.
[220] Li Z, Li Z, Yang B, Yang Y, Zhang Y, Esling C, et al. Large low-field magnetocaloric effect in directionally solidified Ni55Mn18+xGa27−x (x=0, 1, 2) alloys. Journal of Magnetism and Magnetic Materials. 2018;445:71-6.
[221] Qu YH, Cong DY, Sun XM, Nie ZH, Gui WY, Li RG, et al. Giant and reversible room-temperature magnetocaloric effect in Ti-doped Ni-Co-Mn-Sn magnetic shape memory alloys. Acta Materialia. 2017;134:236-48.
[222] Wei Z-Y, Liu E-K, Li Y, Xu G-Z, Zhang X-M, Liu G-D, et al. Unprecedentedly Wide Curie-Temperature Windows as Phase-Transition Design Platform for Tunable Magneto-Multifunctional Materials. Advanced Electronic Materials. 2015;1:1500076-n/a.
[223] Fjellvåg H, Andresen AF. On the crystal structure and magnetic properties of MnNiGe. Journal of Magnetism and Magnetic Materials. 1985;50:291-7.
[224] Liu E, Wang W, Feng L, Zhu W, Li G, Chen J, et al. Stable magnetostructural coupling with tunable magnetoresponsive effects in hexagonal ferromagnets. 2012;3:873.
[225] Liu EK, Zhang HG, Xu GZ, Zhang XM, Ma RS, Wang WH, et al. Giant magnetocaloric effect in isostructural MnNiGe-CoNiGe system by establishing a Curie-temperature window. Applied Physics Letters. 2013;102:122405.
[226] Zhang D, Nie Z, Wang Z, Huang L, Zhang Q, Wang Y-d. Giant magnetocaloric effect in MnCoGe with minimal Ga substitution. Journal of Magnetism and Magnetic Materials. 2015;387:107-10.
[227] Franco V, Caballero-Flores R, Conde A, Knipling KE, Willard MA. Magnetocaloric effect and critical exponents of Fe77Co5.5Ni5.5Zr7B4Cu1: A detailed study. Journal of Applied Physics. 2011;109:07A905-8.
[228] Franco V, Blazquez JS, Conde A. Field dependence of the magnetocaloric effect in materials with a second order phase transition: A master curve for the magnetic entropy change. Applied Physics Letters. 2006;89:2512-5.
[229] Hiroyoshi H, Hoshi A, Nakagawa Y. Arrott-Noakes plots near the Curie temperature of Fe3Pt: Ordered and disordered alloys in high magnetic fields. Journal of Applied Physics. 1982;53:2453-5.
[230] Banerjee BK. On a generalised approach to first and second order magnetic transitions. Physics Letters. 1964;12:16-7.
[231] Kouvel JS, Fisher ME. Detailed Magnetic Behavior of Nickel Near its Curie Point. Physical Review. 1964;136:A1626-A32.
[232] Kadanoff LP. Scaling laws for Ising models near Tc. Physics. 1966;2:263.

[233] Kaul SN. Static critical phenomena in ferromagnets with quenched disorder. Journal of Magnetism and Magnetic Materials. 1985;53:5-53.
[234] Huang K. Statistical Mechanics, 2nd ed. . New York, : Wiley; 1987.
[235] Thanh TD, Huy Dan N, Phan T-L, Kumarakuru H, Olivier EJ, Neethling JH, et al. Critical behavior of the ferromagnetic-paramagnetic phase transition in Fe90−xNixZr10 alloy ribbons. Journal of Applied Physics. 2014;115: 023903-10.
[236] Winschuh K, Rosenberg M. Critical behavior of amorphous (Fe1−xMx)90Zr10 alloys with M=Co, Ni, and 0<x<0.04. Journal of Applied Physics. 1987;61:4401-3.
[237] Álvarez P, Marcos JS, Gorria P, Barquín LF, Blanco JA. Magneto-caloric effect in FeZrB amorphous alloys near room temperature. Journal of Alloys and Compounds. 2010;504, Supplement 1:S150-S4.
[238] Perumal A, Srinivas V, Kim KS, Yu SC, Rao VV, Dunlap RA. Magnetic properties of amorphous ${\mathrm{Fe}}_{90-x}{\mathrm{Mn}}_{x}{\mathrm{Zr}}_{10}(0<~x<~12)$ alloys. Physical Review B. 2002;65:064428.
[239] Yamada K, Ishikawa Y, Endoh Y, Masumoto T. The magnetic phase transition of an amorphous Fe□P□C and its alloys containing Ni and Cr. Solid State Communications. 1975;16:1335-8.
[240] Kyprianidis IM, Achilleos CA, Tsoukalas IA, Bremers H, Hesse J. Magnetic phase transitions in FeCrBSi alloys. J Magn Magn Mater. 1996;161:203-8.
[241] Kaul SN. Critical phenomena and giant superparamagnetic moments above Curie point of the amorphous ${\mathrm{Fe}}_{20}$${\mathrm{Ni}}_{60}$${\mathrm{P}}_{14}$${\mathrm{B}}_{6}$ alloy. Phys Rev B,. 1981;23:1205-15.
[242] Kaul SN. Detailed magnetization study of an amorphous ferromagnet. Phys Rev B,. 1981;24:6550-65.
[243] Böhnke G, Kaul SN, Kettler W, Rosenberg M. Critical behaviour of the electrical resistivity in amorphous ferromagnetic alloys. Solid State Communications. 1983;48:743-6.
[244] Liu XB, Altounian Z, Ryan DH. Magnetocaloric effect in La(Fe 0.88 Al 0.12) 13 C x interstitial compounds. Journal of Physics D: Applied Physics. 2004;37:2469.
[245] Guillou F, Yibole H, van Dijk NH, Zhang L, Hardy V, Brück E. About the mechanical stability of MnFe(P,Si,B) giant-magnetocaloric materials. Journal of Alloys and Compounds. 2014;617:569-74.
[246] Amaral JS, Silva NJO, Amaral VS. A mean-field scaling method for first- and second-order phase transition ferromagnets and its application in magnetocaloric studies. Applied Physics Letters. 2007;91:172503.
[247] Tishin AM, Spichkin YI, Zverev VI, Egolf PW. A review and new perspectives for the magnetocaloric effect: New materials and local heating and cooling inside the human body. International Journal of Refrigeration. 2016;68:177-86.
[248] Sharifi I, Shokrollahi H, Amiri S. Ferrite-based magnetic nanofluids used in hyperthermia applications. Journal of Magnetism and Magnetic Materials. 2012;324:903-15.
[249] Nikiforov VN, Filinova EY. Biomedical Applications of Magnetic Nanoparticles. Magnetic Nanoparticles: Wiley-VCH Verlag GmbH & Co. KGaA; 2009. p. 393-455.
[250] McNerny KL, Kim Y, Laughlin DE, McHenry ME. Chemical synthesis of monodisperse γ-Fe–Ni magnetic nanoparticles with tunable Curie temperatures for self-regulated hyperthermia. Journal of Applied Physics. 2010;107:09A312.
[251] Kobayashi T. Cancer hyperthermia using magnetic nanoparticles. Biotechnology Journal. 2011;6:1342-7.
[252] Deatsch AE, Evans BA. Heating efficiency in magnetic nanoparticle hyperthermia. Journal of Magnetism and Magnetic Materials. 2014;354:163-72.
[253] Purushotham S, Ramanujan RV. Modeling the performance of magnetic nanoparticles in multimodal cancer therapy. Journal of Applied Physics. 2010;107:114701.

[254] Jordan A, Scholz R, Maier-Hauff K, van Landeghem FKH, Waldoefner N, Teichgraeber U, et al. The effect of thermotherapy using magnetic nanoparticles on rat malignant glioma. Journal of Neuro-Oncology. 2006;78:7-14.
[255] Johannsen M, Gneveckow U, Eckelt L, Feussner A, WaldÖFner N, Scholz R, et al. Clinical hyperthermia of prostate cancer using magnetic nanoparticles: Presentation of a new interstitial technique. International Journal of Hyperthermia. 2005;21:637-47.
[256] Alphandéry E, Faure S, Seksek O, Guyot F, Chebbi I. Chains of Magnetosomes Extracted from AMB-1 Magnetotactic Bacteria for Application in Alternative Magnetic Field Cancer Therapy. ACS Nano. 2011;5:6279-96.

Figure Captions

Fig. 1 Magnetocaloric cycle (a) a magnetocaloric material having random magnetic moments, (b) when the material is adiabatically magnetized, the magnetic entropy decreases and the temperature increases, (c) the material is brought back to its initial temperature after removal of heat by a suitable heat transfer fluid, (d) when the material is adiabatically demagnetized, the temperature decreases and this lower temperature can be used to cool the heat load.

Fig. 2 A schematic of the entropy of MCM as function of temperature, showing the ΔS_M (vertical arrow) and the ΔT_{ad} (horizontal arrow).

Fig. 3 Schematic representation of magnetization (M) and specific heat (C_H) with respect to temperature and magnetic field for second-order (a, c) and first-order (b, d) phase transition materials.

Fig. 4 Fe–Ni phase diagram. The dashed red line is the extrapolation of the T_C of the γ-phase to the iron rich region.

Fig. 5 The $M(T)$ (left) and the dM/dT (right) versus T for γ-$(Fe_{70}Ni_{30})$ nanoparticles.

Fig. 6 (a) -ΔS_M versus T for (a) $(Fe_{70}Ni_{30})_{89}B_{11}$ nanoparticles (b) multiphase bulk $(Fe_{70}Ni_{30})_{89}B_{11}$ alloy at applied magnetic field up to 5 T.

Fig. 7 ΔS_M versus T at applied magnetic field of 5 T for $(Fe_{70}Ni_{30})_{95}Mn_5$ (quenched), $(Fe_{70}Ni_{30})_{92}Mn_8$ (as milled), $(Fe_{70}Ni_{30})_{92}Mn_8$ (vacuum annealed), $(Fe_{70}Ni_{30})_{92}Mn_8$ (quenched) and $(Fe_{70}Ni_{30})_{89}Mn_{11}$ (quenched) nanoparticles.

Fig 8 $-\Delta S_M$ versus T under magnetic field strength ranging from 0.5 T to 5 T for **(a)** $(Fe_{70}Ni_{30})_{99}Cr_1$, **(b)** $(Fe_{70}Ni_{30})_{97}Cr_3$, **(c)** $(Fe_{70}Ni_{30})_{95}Cr_5$, **(d)** $(Fe_{70}Ni_{30})_{94}Cr_6$, and **(e)** $(Fe_{70}Ni_{30})_{93}Cr_7$. (**f**) Dependence of $-\Delta S_M$ (left axis) and RCP (right axis) on Cr content in $(Fe_{70}Ni_{30})_{100-x}Cr_x$ nanoparticles.

Fig. 9 T_C as a function of composition (a) $(Fe_{70}Ni_{30})_{100-x}Cr_x$ with x= 0 to 8. (b) $(Fe_{70}Ni_{30})_{100-x}Mn_x$ with x= 0 to 11. Solid line represents the theoretical values predicted from FeNi phase diagram and empirical equation $T_C = T^1_C + (T_C/dc)c$, while points (red square) are experimental results.

Fig. 10 Relative cooling power versus Curie temperature for Fe-Ni based nanoparticles. The materials for near room temperature applications are shown within the circle.

Fig. 11 Temperature dependence of ΔS_M and ΔT_{ad} under a magnetic field of up to 8 T for $Fe_{17}Er_2$ determined from (a) magnetization measurements and (b) heat-capacity measurements The insets of (a) show the theoretical values of ΔS_M and ΔT_{ad}.

Fig. 12 ΔS_M versus T for a magnetic field of 1.1 T; (a) $Fe_{80-x}B_{12}Cr_8La_x$ (b) $Fe_{80-x}B_{12}Cr_8Ce_x$ (c) $Fe_{80-x}B_{12}Cr_8Gd_x$ melt spun ribbons.

Fig. 13 Magnetic entropy change as a function of temperature under magnetic field of 0.4 T for (a) $Fe_{90-x}Zr_{10}B_x$ (x = 3 to 9) and (b) $Fe_{93-x}Zr_7B_x$ (x = 0 to 13).

Fig. 14 Relative cooling power versus Curie temperature for Fe based magnetocaloric materials. Materials suitable for near room temperature applications are shown within the circle.

Fig. 15 Schematic representation of self pumping magnetic cooling employing ferrofluid as heat transfer from heat load to heat sink.

Fig. 16 The effect of application and removal of magnetic field of 0.3 T on the temperature profile for initial temperature of heat load of (a) 87 °C, (b) 74 °C and (c) 64 °C, respectively. The temperature drop (cooling) in (a), (b) and (c) was ~ 28 °C, ~ 24 °C and 20 °C, respectively.

Fig. 17 Crystal structure of Fe_2P alloy at room temperature.

Fig. 18 $-\Delta S_M$ versus T of $Mn_{1.2}Fe_{0.8}P_{0.75}Ge_{0.25}$ for different field changes values.

Fig. 19 The $-\Delta S_M$ values under a field change of 1T (open curves) and 2T (solid curves) for $Mn_xFe_{1.95-x}P_{1-y}Si_y$ (x= 1.34, 1.32, 1.30, 1.28, 1.24, 0.66, 0.66 and y= 0.46, 0.48, 0.50, 0.52, 0.54, 0.34, 0.37) compounds, respectively (from left to right). The data of Gd metal under a field change of 1T (open diamond) and 2T (solid diamond) are included.

Fig. 20 (a) magnetocaloric properties (ΔT_{cyclic}) of $MnFe_{0.95}P_{0.67-x}Si_{0.33}B_x$ and $MnFe_{0.95}P_{0.55}Si_{0.45}$ measured for a magnetic field 1.1 T. Closed and open symbols are for warming and cooling, for $MnFe_{0.95}P_{0.55}Si_{0.45}$ warming and cooling curves are overlaps. (b) ΔT_{cyclic} measured by a direct method at constant starting temperatures before the magnetic field changes($|B|$ = 1 T).

Fig. 21 Temperature dependence of the magnetization at a magnetic field of 2 T for the $Mn_{1.1}Fe_{0.9}P_{0.75}Ge_{0.25}$ powders (a) annealed at different temperature (b) corresponding ΔS_M as a function of temperature (c) annealed at different time (d) corresponding ΔS_M as a function of temperature.

Fig. 22 Temperature dependence of magnetization during heating and cooling at a magnetic field of 1 T for $Mn_{1.00}Fe_{0.95}P_{0.595}Si_{0.33}B_{0.075}$ alloys (a) annealed for different times (b) annealed at different temperatures. The entropy change as a function of temperature for $Mn_{1.00}Fe_{0.95}P_{0.595}Si_{0.33}B_{0.075}$ (c) annealed for different times (d) annealed at different temperatures.

Fig. 23 (a) Curie temperature and (b) thermal hysteresis as function of the transition metal (Co, Mn, Cu) content in $(Mn,Fe,T)_{1.95}P_{0.50}Si_{0.50}$.

Fig. 24 (a) *M* vs *T* curves in 1T field for the first, second and third cycles (b) Field dependence of thermal hysteresis of samples annealed at 1123K, 1223K and 1323K for 9h. (c) Field dependence of thermal hysteresis of samples annealed at 1223K for 3h, 9h and 15h.

Fig. 25 Temperature dependence of Landau coefficients a_1, a_3 and a_5 for (a) $Mn_{1.1}Fe_{0.9}P_{0.87}Ge_{0.13}$ powder, (b) $Mn_{1.1}Fe_{0.9}P_{0.81}Ge_{0.19}$ powder, (c) $Mn_{1.1}Fe_{0.9}P_{0.79}Ge_{0.21}$ powder, (d) $Mn_{1.1}Fe_{0.9}P_{0.79}Ge_{0.21}$ ribbon, (e) $Mn_{1.1}Fe_{0.9}P_{0.74}Ge_{0.26}$ powder and (f) $Mn_{1.1}Fe_{0.9}P_{0.68}Ge_{0.32}$ powder alloys.

Fig. 26 Theoretical and experimental ΔS_M versus *T* for magnetic field change of 5T in Ge0.26, Ge0.3 and Ge0.32 ribbons.